附件一

行政院國家科學委員會補助專題研究計畫 □ 成 果 報 告 ☑期中進度報告

介觀系統的自旋抽運與電荷抽運(1/3)

計畫類別：☑ 個別型計畫　　□ 整合型計畫
計畫編號：NSC 93 － 2112 － M － 009 － 017 －
執行期間： 2005 年 08 月 01 日至 2006 年 07 月 31 日

計畫主持人：朱仲夏 教授
共同主持人：
計畫參與人員：M. Büttiker, P. Samuelsson, Mal'shukov, K. A. Chao, 唐志雄, 鄔其君, 鍾淑維, 王律堯, 張榮興, 陳冠伊

成果報告類型(依經費核定清單規定繳交)：☑精簡報告　□完整報告

本成果報告包括以下應繳交之附件：
□赴國外出差或研習心得報告一份
□赴大陸地區出差或研習心得報告一份
□出席國際學術會議心得報告及發表之論文各一份
□國際合作研究計畫國外研究報告書一份

處理方式：除產學合作研究計畫、提升產業技術及人才培育研究計畫、列管計畫及下列情形者外，得立即公開查詢
□涉及專利或其他智慧財產權，□一年□二年後可公開查詢

執行單位：國立交通大學電子物理系

中　華　民　國　95　年　5　月　30　日

行政院國家科學委員會專題研究計劃成果報告

介觀結構的量子傳輸: (一) 應力感應與自旋流耦合產生之奈米機械震盪；(二) 對電子式 Mach-Zehnder 干涉儀和電子式 Hanbury Brown Twiss 干涉儀作電流及雜訊干涉度的分析；(三)在 Rashba-type 量子窄通道產生自旋流；(四) 在 Rashba-type 窄通道中雜質效應對於產生直流自旋流之影響；(五) 自旋霍爾效應對二維條狀半導體的邊緣磁化強度以及電導的影響；(六) 兩個接腳的介觀環在傳輸下的 Fano 效應；(七)一維系統的三腳接點之波函數連結； (八) 在本質自旋霍爾效應下在彈性散射體附近感應出自旋雲。

The quantum transport in mesoscopic structure: [I] Strain induced coupling of spin current to nanomechanical oscillations; [II] Visibility of current and shot noise in electrical Mach-Zehnder and Hanbury Brown Twiss interferometers; [III] dc spin current generation in a Rashba-type quantum channel; [IV] Effects of elastic scatterer on the dc spin current generation in a Rashba-type channel; [V] Spin Hall Effect on Edge Magnetization and Electric conductance of a 2D Semiconductor Strip; [VI] Fano resonance in transport through a mesoscopic two-lead ring; [VII] Connecting wave functions at a three-legs junction of one-dimensional channels; [VIII] Spin cloud induced around an elastic scatterer by the intrinsic spin-Hall effect.

一、中文摘要:

在本計劃中，我們研究了介觀系統的自旋抽運與電荷抽運(2/3)，其中包括(一) 應力感應與自旋流耦合產生之奈米機械震盪；(二) 對電子式 Mach-Zehnder 干涉儀和電子式 Hanbury Brown Twiss 干涉儀作電流及雜訊干涉度的分析；(三)在 Rashba-type 量子窄通道產生自旋流；(四) 在 Rashba-type 窄通道中雜質效應對於產生直流自旋流之影響； (五) 自旋霍爾效應對二維條狀半導體的邊緣磁化強度以及電導的影響；(六)兩個接腳的介觀環在傳輸下的 Fano 效應；(七)一維系統的三腳接點之波函數連結；(八)在本質自旋霍爾效應下在彈性散射體附近感應出自旋雲。

(一) 我們提出不用靠鐵磁材料而達到電子自旋與奈米機械系統之機械運動耦合之效應。 這種方法會在 narrow gap 半導體材料中，因應力而感應出自旋軌道交互作用而這種方式可透過奈米機械元件所形成的懸空棒狀結構以去偵測和操控自旋流。 (二)利用 ac 閘極來產生和量測自旋流：我們研究在 III-V 族窄能隙的量子阱或量子線中，可以利用一個時變的閘極去影響 Rashba 自旋軌道耦合係數來產生自旋流。我們也提出對此交流自旋流的整流方法，以及利用電性量測去測量在二維電子氣中帶有交流自旋流的閘極附近的電壓以達到偵測自旋流之目的；我們提出一種不需要使用光學或磁性材料來達到"產生"和"偵測"自旋流的方法。

(二) 本研究針對電子式 Mach-Zehnder 干涉儀和電子式 Hanbury Brown Twiss 干涉儀作電流及雜訊干涉度的分析。此電子式干涉儀是利用高磁場下電子沿著導体的邊通道(edge

states)運動特性所做成。傳輸的特性可藉由 Aharonov-Bohm flux 來調整。我們研究環境溫度及外加偏壓對電流及雜訊干涉度的影響。Dephasing 效應是由虛探針模型來模擬。比較兩電子式干涉儀是有趣的，因為 Mach-Zehnder 干涉儀是電子振幅(單粒子)干涉儀，然而 Hanbury Brown Twiss 干涉儀是電子強度（雙粒子）干涉儀。若要做直接的比較，只能經由量測雜訊。我們發現 Hanbury Brown Twiss 干涉儀中的雜訊干涉度對環境溫度、外加電壓及 dephasing 的反應是大約相似於 Mach-Zehnder 干涉儀的第一諧波雜訊干涉度。相對的，Mach-Zehnder 干涉儀的第二諧波雜訊干涉度被環境溫度、外加偏壓及 dephasing rate 的影響高於第一諧波雜訊干涉度。

(三)共振非彈性散射對於直流自旋流的產生扮演重要的角色，共振非彈性散射使得單一交流偏壓指狀閘極橫跨在具有Rashba自旋軌道的量子窄通道中產生自旋流,此交流偏壓的指狀閘極使Rashba耦合係數隨時間震盪變化，造成自旋相關的共振非彈性散射機制，自旋流產生必須同時存在靜態的與動態的Rashba偶合係數，而自旋流正比$\alpha_0\alpha_1^2$，由於結構對稱所以並不會產生直流電流，我們也可以利用兩個指狀閘極來增強自旋流強度。

(四) 我們探討在 Rashba-type 窄通道中雜質對直流自旋流的影響，此直流自旋流可由單一交流指狀閘極所產生而且不會伴隨直流電流，此彈性散射源對直流自旋流有重要影響，我們考慮橫向均勻的位壘產生的反彈散射機制；而對於橫向不均勻位壘會產生反彈散射和能帶混成的效果，我們也比較的吸引和排斥性的非均勻位能對自旋流的影響，對於吸引性的位壘而言，在不同能帶交錯點附近會產生額外的結構，這是由於 inter-subband 間的躍遷到能帶底部形成準束縛態造成的結果。

(五)我們研究二維擴散系統下，變化二維條狀系統的寬度，探討本質自旋霍爾效應對於自旋累積和電導的影響；結果顯示當縱向穩態電流流動時，條狀樣品邊緣對於自旋極化出現阻尼震盪的行為，此一結果與樣品寬度和 Dresselhaus 自旋軌道偶合強度有關聯，對於自旋累積，三次方的交互作用項是非常重要的，如預期一般，對於 Rashba 自旋軌道交互作用並無此一自旋累積的情形發生。

（六）兩接頭的介觀環的 Fano 共振傳輸的研究：我們研究在無外加磁場情況下有兩個接頭的一維介觀環的傳輸現象；我們研究集中在環中的位能並沒有規範出一個封閉性共振腔或是封閉性量子點的例子，即使在沒有良好定義的準束縛態下，我們依然發現穿透係數出現 Fano 結構；這些 Fano 結構出現是由於符合環的駐波條件，他們對於系統參數的對稱性相當敏感。當系統完全對稱時，Fano 結構變成無限窄，此一結果告訴我們對於一般 Fano 結構是因為連續能量的粒子穿透一分立的共振能階所產生的干涉現象結果，值得商榷。

（七）一維系統的三腳接點之波函數連結：我們提出一種方法去處理一維分支的三接腳(Y 型接腳)結構中,波函數如何去連接;我們的結果不同於 Griffiths 的結論[Trans. Faraday Soc. **49**, 345 (1953)]，我們的模型可以處理不同寬度的準一維接腳結構，我們用我們的方法去比較在一維和準一維系統下都得到不錯的擬合，因此此一模型對於描述準一維結構是相當有用的。

(八)在本質自旋霍爾效應下在彈性散射體附近感應出自旋雲: 類比於電流流過雜質實產生 Landauer 電偶極矩，由於本質自旋霍爾效應，在自旋無關的散射體附近也會感應出墊子自旋雲，在彈道傳輸的範疇內，在 Rashba 自旋軌道交互作用下，不會產生自旋霍爾電流，但也會感應出自旋雲。

Abstract:

We study the spin and charge pumping in mesoscopic structures: [I] Strain induced coupling of spin current to nanomechanical oscillations; [II] Visibility of current and shot noise in electrical Mach-Zehnder and Hanbury Brown Twiss interferometers; [III] dc spin current generation in a Rashba-type quantum channel; [IV] Effects of elastic scatterer on the dc spin current generation in a Rashba-type channel; [V] Spin Hall Effect on Edge Magnetization and Electric conductance of a 2D Semiconductor Strip; [VI] Fano resonance in transport through a mesoscopic two-lead ring; [VII] Connecting wave functions at a three-legs junction of one-dimensional channels； [VIII] Spin cloud induced around an elastic scatterer by the intrinsic spin-Hall effect.

.

[I] Strain induced coupling of spin current to nanomechanical oscillations：
We propose a setup which allows to couple the electron spin degree of freedom to the mechanical motions of a nanomechanical system not involving any of the ferromagnetic components. The proposed method employs the strain induced spin-orbit interaction of electron in narrow gap semiconductors. We have shown how this method can be used fro detection and manipulation of the spin flow through a suspended rod in a nanomechanical device.

[II] Visibility of current and shot noise in electrical Mach-Zehnder and Hanbury Brown Twiss interferometers :
We investigate the visibility of the current and shot-noise correlations of electrical analogs of the optical Mach-Zehnder interferometer and the Hanbury Brown Twiss interferometer. The electrical analogs are discussed in conductors subject to high magnetic fields where electron motion is along edge states. The transport quantities are modulated with the help of an Aharonov-Bohm flux. We discuss the conductance (current) visibility and shot noise visibility as a function of temperature and applied voltage. Dephasing is introduced with the help of fictitious voltage probes. Comparison of these two interferometers is of interest since the Mach-Zehnder interferometer is an amplitude (single-particle) interferometer whereas the Hanbury Brown Twiss interferometer is an intensity (two-particle) interferometer. A direct comparison is only possible for the shot noise of the two interferometers. We find that the visibility of shot noise correlations of the Hanbury Brown Twiss interferometer as function of temperature, voltage or dephasing, is qualitatively similar to the visibility of the first harmonic of the shot noise correlation of the Mach-Zehnder interferometer. In contrast, the second harmonic of the shot noise visibility of the Mach-Zehnder interferometer decreases much more rapidly with increasing temperature, voltage or dephasing rate.

[III] dc spin current generation in a Rashba-type quantum channel:
We propose and demonstrate theoretically that resonant inelastic scattering _RIS_ can play an important role in dc spin current generation. The RIS makes it possible to generate dc spin current via a simple gate configuration: a single finger gate that locates atop and orients transversely to a quantum channel in the presence of Rashba spin-orbit interaction. The ac-biased finger gate gives rise to a time variation in the Rashba coupling parameter, which causes spin-resolved RIS and, subsequently, contributes to the dc spin current. The spin current depends on both the static and the dynamic parts in the Rashba coupling parameter, α_0 and α_1, respectively, and is proportional to $\alpha_0\alpha_1^2$ The proposed gate configuration has the added advantage that no dc charge current is generated. Our study also shows that the spin current generation can be enhanced significantly in a double finger-gate configuration.

[IV] Effects of impurity on the dc spin current generation in a Rashba-type channel:
We have investigated the effects of a single impurity on the dc spin current (SC) generation in a Rashba-type channel. The dc SC could be generated via a single ac finger-gate (FG). Effects of impurity have strong dependence of transverse-location and strength for the transport of dc SC in the channel. The spin-resolved dip structures are broadened while the impurity is away from the edge inside of the ac-FG. The effect of impurity is decreased for the impurity in the edge of the channel. The impurity has small effect for the transport while the impurity is outside of the ac-FG. The spin-resolved inter-subband transition is observed while the incident energy near each subband threshold because the symmetry of transverse direction is broken by the impurity.

[V] Spin Hall Effect on Edge Magnetization and Electric Conductance of a 2D semiconductor Strip:
The intrinsic spin Hall effect on spin accumulation and electric conductance in a diffusive regime of a 2D electron gas has been studied for a 2D strip of a finite width. It is shown that the spin polarization near the flanks of the strip, as well as the electric current in the longitudinal direction, exhibit damped oscillations as a function of the width and strength of the Dresselhaus spin-orbit interaction. Cubic terms of this interaction are crucial for spin accumulation near the edges. As expected, no effect on the spin accumulation and electric conductance have been found in case of Rashba spin-orbit interaction.

[VI] Fano resonance transport through a mesoscopic two-lead ring：
The ballistic transport through a one-dimensional two-lead ring at zero magnetic field is studied. We have focused on the case in which the potential in the ring does not define closed cavities or dots. Even in the absence of well-defined quasibound states, we find Fano profiles in the transmission probability. Those Fano profiles appear at energies corresponding to the standing-wave states in the ring, but their occurrence depends sensitively on the commensurability of the system parameters. When the system parameters are commensurate, the widths of the profiles at some energies are infinitesimally small. These findings suggest that the conventional understanding of the Fano profiles as a result of the interference effect of the

transition through resonant states and nonresonant continuum of states, might not account for all the Fano profiles seen in the transport measurements. Moreover, the sensitivity and tunability of the resonance with respect to the system parameters may be usable in the fabrication of electrical nanodevices.

[VII] Connecting wave functions at a three-leg junction of one-dimensional channels:
We propose a scheme to connect the wave functions on different one-dimensional branches of a three-leg junction _*Y* junction_. Our scheme differs from that due to Griffith [Trans. Faraday Soc. **49**, 345 (1953)] in the respect that ours can model the difference in the widths of the quasi-one-dimensional channels in different systems. We test our scheme by comparing results from a doubly connected one-dimensional system and a related quasi-one-dimensional system, and we find a good agreement. Therefore our scheme may be useful in the construction of one-dimensional effective models out of _multiply connected_ quasi-one-dimensional systems.

[VIII] Spin cloud induced around an elastic scatterer by the intrinsic spin-Hall effect:
Similar to the Landauer electric dipole created around an impurity by the electric current, a spin polarized cloud of electrons can be induced by the intrinsic spin-Hall effect near a spin independent elastic scatterer. It is shown that in the ballistic range around the impurity, such a cloud appears in the case of Rashba spin-orbit interaction, even though the bulk spin-Hall current is absent.

Keywords:
Quantum transport, quasi-bound state, inelastic scattering, quantum channel, spin current, Spin Hall Effect, Spin accumulation, spin cloud, Rashba spin-orbit interaction, Dresselhau spin-orbit interaction, mesoscopic ring, Fano structures, persistent current, current visibility, noise visibility, Mach-Zehnder interferometer, the Hanbury Brown Twiss interferometer, edge states, Aharonov-Bohm flux, dephasing, Fano effect.

二、Motivations and goals

[I] Strain induced coupling of spin current to nanomechanical oscillations：

An ability to control the spin transport in semiconductors is a key problem to be solved towards implementation of semiconductor spintronics into quantum information processing [1-3]. Many methods have been proposed to achieve control of the electron spin degree of freedom using magnetic materials, external magnetic fields and optical excitation [3]. Other promising ideas involve the intrinsic spin-orbit interaction (SOI) in narrow gap semiconductors to manipulate the spin by means of electron fields [4] and electric gates [5-7]. Recently, some of these ideas have been experimentally confirmed [8,9].

In semiconductors the spin-orbit effect appears as an interaction of the electron spin with an effective magnetic field whose direction and magnitude depend on the electron momentum. A specific form of this dependence is determined by the crystal symmetry, as well as by the symmetry of the potential energy profile in heterostructures. In strained semiconductors new components of the effective magnetic field appear due to violation of the local crystal symmetry [10]. The effective of the strain induced SOI on spin transport was spectacularly demonstrated by Kato *et. al.* in their Faraday rotation experiment [9]. An interesting property of the strain induced SOI is that the strain can be associated with mechanical motion of the solid, in particular, with oscillations in nanomechanical systems (NMS), in such a way making possible the spin-orbit coupling of the electron spin to nanomechanical oscillations. At the same time a big progress in fabricating various NMS [11] allows one to reach the required parameter range to observe subtle effects produced by such a coupling.

We will consider NMS in the form of a suspended beam with a doped semiconductor film epitaxially grown on its surface (see Fig. 1). An analysis of the SOI in this system shows that the flexural and torsion vibrational modes couple most effectively to the electron spin. As a simple example, we will focus the torsion modes. The strain associated with torsion produces the spin-orbit field which is linear with respect to the electron momentum and is directed perpendicular to it. This field varies in time and space according to respective variations of the torsion strain. Due to the linear dependence on the momentum, the SOI looks precisely as interaction with spin dependent electromagnetic vector potential. An immediate result of this analogy is that the time dependent torsion gives rise to a motive force on electrons. Such a force, however, acts in different directions on particles with oppositely oriented spins, including thus the spin current in the electron gas. The physics of this phenomenon is very similar to the spin current generation under time dependent Rashba SOI, where the time dependence of the SOI coupling parameter is provided by the gate voltage variation [6]. In the present work we will focus, however, on the inverse effect. Due to the SOI coupling, the spin current flowing through the beam is expected to create a mechanical torsion. The torque effect on NMS due to spin flow has been previously predicted [12] for a different physical realization, where the torque has been created by spin flips at nonmagnetic-ferromagnetic interface. They also suggested an experimental set up to measure such a small torque. The torque due to SOI effect can be by 2 orders of magnitude stronger than the torque produced by the current flowing through the FM-NM interface. Hence, the SOI effect can be measured by the same method as was proposed [12]. Besides this method, other sensitive techniques for displacement measurements can be

employed [13].

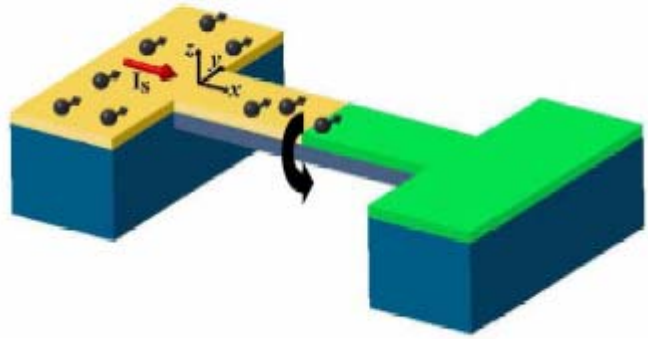

Fig. 1 : Schematic illustration of electromechanical spin current detector, containing a suspended semiconductor-mental (S-M) rectangular rod atop an insulating substrate (blue). A spin current is injected from the left semiconductor reservoir (yellow) and then diffuses toward the metallic film (green). While passing through the semiconductor film, the spin current induces torque shown by the black arrow.

[Reference]:

[1] *Semiconductor Spintronics and Quantum Computation*, edited by D. D. Awschalom, N. Samarth, and D. Loss (Springer-Verlag, Berlin, 2002).

[2] S. A.Wolf, *et. al.*, Science. **294**, 1488 (2001).

[3] I. Žutić, J. Fabian, and S. Das Sarma, Rev. Mod. Phys. **76**, 323 (2004).

[4] J. Sinova, *et. al.*, Phys. Rev. Lett. **92**, 126603 (2004); S. Murakami, N. Nagaosa and S. Zhang, Science **301**, 1348 (2003); V. M. Edelstein, Solid State Commun., **73**, 233 (1990); A. Voskoboynikov, *et. al.,* Phys. Rev. B. **59,** 12514 (1999); L. S. Levitov and E. I. Rashba, Phys. Rev. B, **67,** 115324 (2003).

[5] S. Datta and B. Das, Appl. Phys. Lett. **56**, 665 (1990); P. Sharma and P. W. Brouwer, Phys. Rev. Lett. **91**, 16 6801 (2003); M. Governale, F. Taddei, and R. Fazio, Phys. Rev. B, **68**, 155324 (2003).

[6] A. G. Malshukov, *et. al.*, Phys. Rev. B, 68, 23 3307 (2003); C. S. Tang, A. G. Malshukov, and K.A. Chao, cond-mat/0412181.

[7] C. S. Tang, A. G. Mal'shukov, and K. A. Chao, Phys.Rev. B **71**, 195314 (2005).

[8] J. Wunderlich, B. Kästner, J. Sinova, and T. Jungwirth, cond-mat/0410295.

[9] Y. K. Kato, *et. al.*, cond-mat/0502627.

[10] G. E. Pikus and A. N. Titkov, in *Optical Orientation*, edited by F. Meier and B. P. Zakharchenya (North-Holland, Amsterdam, 1984).

[11] M. L. Roukes, Phys. World **14**, 25 (2001); H. G. Craighead, Science **290**, 1532 (2000); A. N. Cleland, *Foundations of Nanomechanics* (Springer, New York, 2003).

[12] P. Mohanty, G. Zolfagharkhani, S. Kettemann, and P. Fulde, Phys. Rev. B **70**, 195301 (2004).

[13] R. G. Knobel and A. N. Cleland, Nature (London) **424**, 291 (2003).

[II] Visibility of current and shot noise in electrical Mach-Zehnder and Hanbury Brown Twiss interferometers:

With the advent of mesoscopic physics, it has become possible to experimentally investigate quantum phase coherent properties of electrons in solid state conductors in a controlled way. In particular, in ballistic mesoscopic samples at low temperatures, electrons can propagate up to several microns without loosing phase information. This opens up the possibility to investigate electrical analogs of various optical phenomena and experiments. An investigation of such analogs is of fundamental interest. On the one hand, it allows one to establish similarities between the properties of photons and conduction electrons, a consequence of the wave nature of the quantum particles. On the other hand, it also allows one to investigate the differences between the two types of particles arising from the different quantum statistical properties of fermions and bosons. For many-particle properties, such as light intensity correlations or correspondingly electrical current correlations, noise, the quantum statistical properties are important. [1,2] Both the wave-nature of the particles as well as their quantum statistics are displayed in a clearcut fashion in interferometer structures. In this work we are concerned with the electrical analogs of two well known optical interferometers, the single-particle Mach-Zehnder (MZ) interferometer and the two-particle Hanbury Brown Twiss (HBT) interferometer.

The MZ-interferometer is a subject of most textbooks in optics.[3] In the framework of quantum optics, considering individual photons rather than classical beams of light, the interference arises due to the superposition of the amplitudes for two different possible paths of a single photon. This leads to an interference term in the light intensity. The MZ-interferometer is thus a prime example of a single particle interferometer.[4] Various electronic interferometers with ballistic transport of the electrons have been investigated experimentally over the last decades, as e.g. Aharonov-Bohm (AB) rings[5] and double-slit interferometers.[6] Detailed investigations of dephasing in ballistic interferometers was carried out in Refs. [7,8]. Only very recently was the first electronic MZ-interferometer realized by Ji et al.[9] in a mesoscopic conductor in the quantum Hall regime. A high visibility of the conductance oscillations was observed, however the visibility was not perfect. This led the authors to investigate in detail various sources for dephasing. As a part of this investigation, also shot noise was measured. Still, some aspects of the experiment are not yet fully understood. Theoretically, Seelig and one of the authors [10] investigated the effect of dephasing due to Nyquist noise on the conductance in a MZ-interferometer. The effect of dephasing on the closely related four-terminal resistance in ballistic interferometers [11] was investigated as well. Dephasing in ballistic strongly interacting systems is discussed by Le Hur. [12,13] Following the experimental work of Ji et al.,[9] Marquardt and Bruder investigated the effect of dephasing on the shot-noise in MZ-interferometers, considering dephasing models based on both classical [14,15] as well as quantum fluctuating fields.[16] Very recently, Forster, Pilgram and one of the authors [17] extended the dephasing model of Refs. [10,14] to the full statistical distribution of the transmitted charge.

The HBT-interferometer [18-20] was originally invented for stellar astronomy, to measure the angular diameter of stars. It is an intensity, or two-particle,[4] interferometer. The interference arises from the superposition of the amplitudes for two different two-particle processes. Importantly, there is no single particle interference in the HBT-interferometer. Consequently, in

contrast to the MZ-interferometer there is no interference in the light intensity, the interference instead appears in the intensity-intensity correlations. Moreover, the intensity-intensity correlation also display the effect of quantum statistics. Photons originating from thermal sources tend to bunch, giving rise to positive intensity cross correlations. For the electronic analog of the HBT-interferometer, it was the corresponding anti-bunching of electrons that originally attracted interest. It was predicted [1] that the electrical current cross correlations in mesoscopic conductors would be manifestly negative, i.e. display anti-bunching, as a consequence of the fermionic statistics of the electrons. Negative current cross correlations were subsequently observed in two independent experiments.[21,22] Recently, anti-bunching for field emitted electrons in vacuum was also demonstrated.[23] The two-particle interference in the HBT-experiment has received much less attention. We emphasize that while the bunching of the photons was necessary for obtaining a finite, positive cross correlation signal, it was the two-particle effect that was of main importance to HBT since the angular diameter of the star was determined from the two-particle interference pattern. In electrical conductors, two-particle effects in AB-interferometers were investigated theoretically in Refs. [24-26]. Only very recently two of the authors and Sukhorukov [27] proposed a direct electronic analog of the optical HBT-interferometer which permits to demonstrate two-particle interference in an unambiguous way.

In this work we investigate and compare in detail the current and and zero-frequency noise in electronic MZ and HBT interferometers. We consider interferometers implemented in mesoscopic conductors in the integer Quantum Hall regime, where the transport takes place along single edge states and Quantum Point Contacts (QPC's) serve as controllable beam splitters. The effect of finite temperature, applied bias and asymmetry, i.e. unequal length of the interferometer arms, is investigated. The strength of the interference contribution is quantified via the visibility of the phase oscillations. The dependence of the visibility on the beam splitter transparencies as well as on the temperature, voltage and asymmetry is discussed in detail. Of interest is the comparison of visibility of the shot-noise correlation of the MZ-interferometer and the HBT-intensity interferometer. Shot noise correlations in the MZ-interferometer exhibit two contributions, one with the fundamental period of h/e and a second harmonic with period h/2e. The shot noise correlations in the HBT-interferometer, even though they are due to two particle processes, are periodic with period h/e. Thus the Aharonov-Bohm period can not be used to identify the two particle processes which give rise to the HBT effect. It is therefore interesting to ask whether the HBT two-particle processes have any other signature, for instance in the temperature or voltage dependence of the visibility of the shot-noise correlation. We find that this is not the case. To the contrary, we find that the shot noise correlations in the HBT intensity interferometer behave qualitatively similar to the h/e shot noise correlation in the MZ-interferometer. In contrast the h/2e contribution in the shot noise of the MZ-interferometer decreases more rapidly with increasing temperature, voltage or dephasing rate than the h/e oscillation in the MZ- or HBT-interferometer.

We investigate dephasing of the electrons propagating along the edge states by connecting one of the interferometer arms to a fictitious, dephasing voltage probe. In all cases, the current and noise of the MZ-interferometer as well as the noise in the HBT-interferometer, the effect of the voltage probe is equivalent to the effect of a slowly fluctuating phase.

[Reference]:

[1] M. Buttiker, Phys. Rev. B **46**, 12485 (1992).

[2] Ya. Blanter and M. Buttiker, Phys. Rep. **336**, 1(2000).

[3] M. Born and E. Wolf, Principles of Optics, 7:th ed. (Cambridge University press, UK, 1999).

[4] L. Mandel, Rev. Mod. Phys. **71**, S274 (1999).

[5] See e.g. S. Pedersen, A.E. Hansen, A. Kristensen, C.B. Sorensen and P.E. Lindelof, Phys. Rev. B **61**, 5457 (2000) and references therein.

[6] E. Buks, R. Schuster, M. Heilblum, D. Mahalu and V. Umansky, Nature **391**, 871 (1999).

[7] A.E. Hansen, A. Kristensen, S. Pedersen, C.B. Sorensen, and P.E. Lindelof, Phys. Rev. B **64**, 045327 (2001).

[8] K. Kobayashi, H. Aikawa, S. Katsumoto and Y. Iye, J. Phys. Soc. Jpn. **71**, 2094 (2002).

[9] Y. Ji, Y. Chung, D. Sprinzak, M. Heilblum, D. Mahalu and H. Shtrikman, Nature **422**, 415 (2003).

[10] G. Seelig, M. Buttiker, Phys. Rev. B **64**, 245313 (2001).

[11] G. Seelig, S. Pilgram, A.N. Jordan and M. Buttiker, Phys. Rev. B **68**, R161310 (2003).

[12] K. Le Hur, Phys. Rev. B **65,** 233314 (2002).

[13] K. Le Hur, cond-mat/0503652.

[14] F. Marquardt and C. Bruder, Phys. Rev. Lett. **92**, 56805 (2004).

[15] F. Marquardt and C. Bruder, Phys. Rev. B **70**, 125305 (2004).

[16] F. Marquardt, cond-mat/0410333.

[17] H. Forster, S. Pilgram and M. Buttiker, cond-mat/0502400.

[18] R. Hanbury Brown and R.Q. Twiss, Philos. Mag. Ser. **745**, 663 (1954).

[19] R. Hanbury Brown and R.Q. Twiss, Nature (London) **177**, 27 (1956).

[20] R. Hanbury Brown and R.Q. Twiss, Nature (London) **178**, 1046 (1956).

[21] M. Henny, S. Oberholzer, C. Strunk, T. Heinzel, K. Ensslin, M. Holland and C. Schonenberger, Science **284**, 296 (1999).

[22] M. Henny, S. Oberholzer, C. Strunk, T. Heinzel, K. Ensslin, M. Holland and C. Schonenberger, Science **284**, 296 (1999).

[23] H. Kiesel, A. Renz, and F. Hasselbach, Nature (London) **418**, 392 (2002).

[24] M. Buttiker, Physica B **175**, 199 (1991).

[25] M. Buttiker, Phys. Rev. Lett. **68**, 843 (1992).

[26] D. Loss and E.V. Sukhorukov, Phys. Rev. Lett. **84**, 1035 (1992).

[27] P. Samuelsson, E.V. Sukhorukov, and M. Buttiker, Phys. Rev. Lett. 92, 26805 (2004).

[III] dc spin current generation in a Rashba-type quantum channel:

Spintronics is important in both application and fundamental arenas.[1,2]. A recent key issue of great interest is the generation of dc spin current (SC) without charge current. Various dc SC generation schemes have been proposed, involving static magnetic field, [3–5] ferromagnetic material, [6] or ac magnetic field. [7] More recently, Rashba-type spin-orbit interaction (SOI) in two dimension electron gas (2DEG) [8–10] has inspired attractive proposals for nonmagnetic dc SC generation. [11–13] Of these recent proposals, including a time-modulated quantum dot with a static spin-orbit coupling, [11] and time modulations of a barrier and the spin-orbit coupling parameter in two spatially separated regions, [12] the working principle is basically adiabatic quantum pumping. Hence, simultaneous generation of both dc spin and charge current is the norm. The condition of zero dc charge current, however, is met only for some judicious choices for the values of the system parameters.

[Reference]:

[1] *Semiconductor Spintronics and Quantum Computation*, edited by D. D. Awschalom, N. Samarth, and D. Loss (Springer-Verlag, Berlin, 2002).

[2] S. A. Wolf, D. D. Awschalom, R. A. Buhrman, J. M. Daughton, S. von Mohnár, M. L. Roukes, A. Y. Chtchelkanova, and D. M. Treger, Science **294**, 1488 _2001_; Y. Kato, R. C. Myers, D. C. Driscoll, A. C. Gossard, J. Levy, and D. D. Awschalom, *ibid.* **299**, 1201 _2003_; S. Murakami, N. Nagaosa, and S. C. Zhang, *ibid.* **301**, 1348 (2003).

[3] E. R. Mucciolo, C. Chamon, and C. M. Marcus, Phys. Rev. Lett. **89**, 146802 _2002_.

[4] Experimental realization was reported by S. K. Watson, R. M. Potok, C. M. Marcus, and V. Umansky, Phys. Rev. Lett. **91**, 258301 (2003).

[5] Q. F. Sun, H. Guo, and J. Wang, Phys. Rev. Lett. **90**, 258301 (2003).

[6] A. Brataas, Y. Tserkovnyak, G. E. W. Bauer, and B. I. Halperin, Phys. Rev. B **66**, 060404(R) (2002).

[7] P. Zhang, Q. K. Xue, and X. C. Xie, Phys. Rev. Lett. **91**, 196602 (2003).

[8] Y. A. Bychkov and E. I. Rashba, J. Phys. C **17**, 6039 (1984).

[9] J. Nitta, T. Akazaki, H. Takayanagi, and T. Enoki, Phys. Rev. Lett. **78**, 1335 (1997).

[10] D. Grundler, Phys. Rev. Lett. **84**, 6074 (2000).

[11] P. Sharma and P. W. Brouwer, Phys. Rev. Lett. **91**, 166801 (2003).

[12] M. Governale, F. Taddei, and R. Fazio, Phys. Rev. B **68**, 155324 (2003).

[13] A. G. Mal'shukov, C. S. Tang, C. S. Chu, and K. A. Chao, Phys. Rev. B **68**, 23 3307 (2003).

[IV] Effects of elastic scatterer on the dc spin current generation in a Rashba-type channel：

Recent interest in spintronics has been prompted by its great potential in physical realization of quantum computation [1-3]. One of the important issue in spintronics is the generation of DC spin current (SC).Various schemes for the DC SC generation have recently been proposed, which involve a non-uniform magnetic field [4] or an oscillating magnetic field [5]. An alternate way to control the electron spin dynamics is via Rashba-type spin-orbit interaction (SOI) [6]. Several proposals have been suggested to generate DC SC with a time-varying Rashba-type SOI

[1,7,8]. The Rashba term can be described by $H_{SO} = \alpha\left(\vec{p}\times\hat{z}\right)\bullet\vec{\sigma}$ where α denotes the spin-orbit

(SO) coupling parameter and $\vec{\sigma}$ stands for the Pauli spin matrices. That α can be tuned by an external gate voltage in the InAs-based heterostructure has been demonstrated experimentally [9,10]. In the presence of such an oscillating a induced by an AC-biased gate, it was found that AC SC is generated in a ballistic quantum channel [7] or in a diffusive 2DEG [8]. Rectification, such as introducing an additional oscillating barrier is needed for the DC SC generation [7,8]. Beyond linear response to a, we find that a DC SC can be generated via a single AC-biased FG atop a ballistic Rashba-type quantum channel [1]. No charge current, however, is generated. Resonance inelastic scattering (RIS) is found to contribute to the robustness in the DC SC [1].

[Reference]:

[1] L.Y. Wang, C.S. Tang, C.S. Chu, Phys. Rev. B **73**, (2003) 085304.

[2] D.D. Awschalom, N. Samarth, D. Loss (Eds.), Semiconductor Spintronics and Quantum Computation, Springer, Berlin, 2002.

[3] S.A. Wolf, et al., Science **294**, (2001) 1488.

[4] Qing-feng Sun, Hong Guo, JianWang, Phys. Rev. Lett. **90** (25) (2003) 8301.

[5] Ping Zhang, Qi-KunXue, X.F. Xie, Phys. Rev. Lett. **90** (19) (2003) 6602.

[6] E.I. Rashba, Fiz. Tverd. Tela (Leningard) **2** (1960) 1224; E.I. Rashba, Sov. Phys. Solid State **2** (1960) 1109; Y.A. Bychkov, E.I. Rashba, J. Phys. **C 17** (1984) 6039.

[7] M. Governale, F. Taddei, R. Fazio, Phys. Rev. B **68** (15) (2003) 5324.

[V] Spin Hall Effect on Edge Magnetization and Electric Conductance of a 2D semiconductor Strip:

Spintronics is a fast developing area to use electron spin degrees of freedom in electronic devices [1]. One of its most challenging goals is to find a method for manipulating electron spins by electric fields. The spin-orbit interaction (SOI), which couples the electron momentum and spin, can be a mediator between the charge and spin degrees of freedom. Such a coupling gives rise to the so-called spin Hall effect (SHE) which attracted much interest recently. Because of SOI the spin flow can be induced perpendicular to the dc electric field, as has been predicted for systems containing spin-orbit impurity scatterers [2]. Later, similar phenomenon was predicted for noncentrosymmetric semiconductors with spin split electron and hole energy bands [3]. It was called the *intrinsic* spin Hall effect, in contrast to the *extrinsic* impurity induced effect, because in the former case it originates from the electronic band structure of a semiconductor sample. Since the spin current carries the spin polarization, one would expect a buildup of the spin density near the sample boundaries. In fact, this accumulated polarization is a first signature of SHE which has been detected experimentally, confirming thus the extrinsic SHE [4] in semiconductor films and intrinsic SHE in a 2D hole gas [5]. On the other hand, there was still no experimental evidence of intrinsic SHE in 2D electron gases. The possibility of such an effect in macroscopic samples with a finite elastic mean free path of electrons caused recently much debates. It has been shown analytically [6–11] and numerically [12] that in such systems SHE vanishes at arbitrary weak disorder in dc limit for isotropic as well as anisotropic [10] impurity scattering when SOI is represented by the so-called Rashba interaction [13]. As one can expect in this case, there is no spin accumulation at the sample boundaries, except for the pockets near the electric contacts [7]. At the same time, the Dresselhaus SOI [14], which dominates in symmetric quantum wells, gives a finite spin Hall conductivity [11]. The latter can be of the order of its universal value $e/8\pi\hbar$. The same has been shown for the cubic Rashba interaction in hole systems [12,15]. In this connection an important question is what sort of the spin accumulation could Dresselhaus SOI induce near sample boundaries. Another problem which, as far as we know, was not discussed in literature, is how the *electric* current along the applied electric field will change under SHE. In the present work we will use the diffusion approximation for the electron transport to derive the driftdiffusion equations with corresponding boundary conditions for the spin and charge densities coupled to each other via SOI of general form. Then the spin density near the flanks of an infinite 2D strip and the correction to its longitudinal electric resistance will be calculated for Dresselhaus and Rashba SOI.

[Reference]:

[1] G. A. Prinz, Science **282**, 1660 (1998); S. A. Wolf *et al.*, Science **294**, 1488 (2001); *Semiconductor Spintronics and Quantum Computation*, edited by D. D. Awschalom, D. Loss, and N. Samarth (Springer-Verlag, Berlin, 2002); I. Zutic´, J. Fabian, and S. Das Sarma, Rev. Mod. Phys. **76**, 323 (2004).

[2] M. I. Dyakonov and V. I. Perel, Phys. Lett. **35A**, 459 (1971); J. E. Hirsch, Phys. Rev. Lett. **83**, 1834 (1999).

[3] S. Murakami, N. Nagaosa, and S.-C. Zhang, Science **301**, 1348 (2003); J. Sinova *et al.*, Phys. Rev. Lett. **92**, 126603 (2004); D. Culcer *et al.*, Phys. Rev. Lett. **93**, 046602 (2004).
[4] Y. K. Kato *et al.*, Science **306**, 1910 (2004).
[5] J. Wunderlich *et al.*, Phys. Rev. Lett. **94**, 047204 (2005).
[6] J. I. Inoue, G. E.W. Bauer, and L.W. Molenkamp, Phys. Rev. B **70**, 041303 (2004); E. I. Rashba, Phys. Rev. B **70**, 201309 (2004); O. Chalaev and D. Loss, Phys. Rev. B **71**, 245318 (2005).
[7] E. G. Mishchenko, A.V. Shytov, and B. I. Halperin, Phys. Rev. Lett. **93**, 226602 (2004).
[8] A. A. Burkov, A. S. Nunez, and A. H. MacDonald, Phys. Rev. B **70**, 155308 (2004).
[9] O.V. Dimitrova, Phys. Rev. B **71**, 245327 (2005).
[10] R. Raimondi and P. Schwab, Phys. Rev. B **71**, 033311 (2005).
[11] A. G. Mal'shukov and K. A. Chao, Phys. Rev. B **71**, 121308(R) (2005).
[12] B. A. Bernevig and S. C. Zhang, Phys. Rev. Lett. **95**, 016801 (2005); K. Nomura *et al.*, cond-mat/0506189 [Phys. Rev. B (to be published)].
[13] Yu.A. Bychkov and E. I. Rashba, J. Phys. C **17**, 6039 (1984).
[14] G. Dresselhaus, Phys. Rev. **100**, 580 (1955).
[15] The cubic Rashba interaction should not be confused with the conventional linear Rashba SOI with the wave-vectordependent coupling constant α(k). In the latter case $\mathrm{SHE} \propto \alpha(k)k/E_F << 1$ [9,12].

[VI] Fano resonance transport through a mesoscopic two-lead ring：

The Fano resonance or profile is conventionally understood as a result of the interference between resonant and nonresonant processes. It was first observed and studied in nuclear physics1 and atomic physics, [1] and later the effect was also observed in a wide variety of spectroscopy such as atomic photoionization, [2] optical absorption, [3] Raman scattering, [4] and also the scanning tunneling through a surface impurity atom.[5,6] As recent progress in the fabrication technology of electrical nanodevices has achieved devices of the size of the order of the various coherence lengths of the conduction electron, quantum mechanical effect and hence the Fano resonance has also been seen in mesoscopic systems. For instance, it is seen in the transport through systems which contain quantum dots [7-12] and carbon nanotubes.[13] Moreover, it is proposed that the resonance can be used in the probe of the phase coherency of the electrons in transport [14,15] and the design of mesoscopic spin filters.[16]

[Reference]:

[1] U. Fano, Phys. Rev. **124**, 1866 (1961).

[2] U. Fano and A. R. P. Rau, *Atomic Collision and Spectra* (Academic Press, Orlando, 1986).

[3] J. Faist, F. Capasso, C. Sirtori, K. W. West, and L. N. Pfeiffer, Nature (London) **390**, 589 (1997).

[4] F. Cerdeira, T. A. Fjeldly, and M. Cardona, Phys. Rev. B **8**, 4734 (1973).

[5] V. Madhavan, W. Chen, T. Jamneala, M. F. Crommie, and N. S. Wingreen, Science **280**, 567 (1998).

[6] J. Li, W.-D. Schneider, R. Berndt, and B. Delley, Phys. Rev. Lett. **80**, 2893 (1998).

[7] J. Gores, D. Goldhaber-Gordon, S. Heemeyer, M. A. Kastner, H. Shtrikman, D. Mahalu, and Y. Meirav, Phys. Rev. B **62**, 2188 (2000).

[8] I. G. Zacharia, D. Goldhaber-Gordon, G. Granger, M. A. Kastner, Y. B. Khavin, H. Shtrikman, D. Mahalu, and U. Meirav, Phys. Rev. B **64**, 155311 (2001).

[9] K. Kobayashi, H. Aikawa, S. Katsumoto, and Y. Iye, Phys. Rev. Lett. **88**, 256806 (2002).

[10] C. Fuhner, U. F. Keyser, R. J. Haug, D. Reuter, and A. D. Wieck, cond-mat/0307590 (unpublished).

[11] K. Kobayashi, H. Aikawa, A. Sano, S. Katsumoto, and Y. Iye, Phys. Rev. B **70**, 035319 (2004).

[12] M. Sato, H. Aikawa, K. Kobayashi, S. Katsumoto, and Y. Iye, cond-mat/0410062 (unpublished).

[13] J. Kim, J.-R. Kim, Jeong-O. Lee, J. W. Park, H. M. So, N. Kim, K. Kang, K.-H. Yoo, and J.-J. Kim, Phys. Rev. Lett. **90**, 166403 (2003).

[14] A. A. Clerk, X. Waintal, and P. W. Brouwer, Phys. Rev. Lett. **86**, 4636 (2001).

[15] Y.-J. Xiong and S.-J. Xiong, Int. J. Mod. Phys. B **16**, 1479 (2002).

[17] J. F. Song, Y. Ochiai, and J. P. Bird, Appl. Phys. Lett. **82**, 4561 (2003).

[VII] Connecting wave functions at a three-legs junction of one-dimensional channels:

For a system which comprises quasi-one-dimensional (Q1D) channels, when only the low-energy regime at near the first subband bottom is considered, it can usually be modeled by a one-dimensional (1D) system. When the system is multiply connected and consists of multileg junctions, the wave functions on the branches are usually connected at the junctions by the Griffith scheme, [1-4] the Shapiro scheme, [5–7] or similar schemes. Since such formulations greatly reduce the calculational effort of complicated multiply connected mesoscopic systems, they have been used widely in the literature. For example, see Refs. [8–19] and the references therein. However, arguments which lead to these connecting schemes are kinematical, [1–7] and it is not clear what kind of junction in practice they describe. Moreover, a comparison between the results of these schemes and that of the exact calculation of Q1D systems has never been done. It is the purpose of this paper to make a comparison between the Griffith result, the Q1D result, and the result due to a scheme we propose in this paper. We find that for clean junctions of Q1D channels, the Griffith result is not even qualitatively in accord with the exact result. The scheme we derive gives a result that compares much better with the exact result.

[Reference]:

[1] H. Kuhn, Helv. Chim. Acta **32**, 2247 _1949_.

[2] J. Stanley Griffith, Trans. Faraday Soc. **49**, 345 _1953_; **49**, 650 (1953).

[3] K. Ruedenberg and C. W. Scherr, J. Chem. Phys. **21**, 1565 (1953).

[4] T. Kottos and U. Smilansky, Ann. Phys. (N.Y.) **274**, 76 (1999).

[5] B. Shapiro, Phys. Rev. Lett. **50**, 747 (1983).

[6] M. Buttiker, Y. Imry, and M. Ya. Azbel, Phys. Rev. A **30**, 1982 (1984).

[7] P. Exner and P. Seba, Rep. Math. Phys. **28**, 7 (1989).

[8] Y. Gefen, Y. Imry, and M. Ya. Azbel, Phys. Rev. Lett. **52**, 129 (1984).

[9] J.-B. Xia, Phys. Rev. B **45**, 3593 (1992).

[10] J. M. Mao, Y. Huang, and J. M. Zhou, J. Appl. Phys. **73**, 1853 (1993).

[11] P. S. Deo and A. M. Jayannavar, Phys. Rev. B **50**, 11629 (1994).

[12] M. V. Moskalets, Low Temp. Phys. **23**, 824 (1997).

[13] C.-M. Ryu and S. Y. Cho, Phys. Rev. B **58**, 3572 (1998).

[14] C. Benjamin and A. M. Jayannavar, Phys. Rev. B **68**, 085325 (2003).

[15] S. K. Joshi, D. Sahoo, and A. M. Jayannavar, Phys. Rev. B **64**,075320 (2001).

[16] B. Molnar, F. M. Peeters, and P. Vasilopoulos, Phys. Rev. B **69**, 155335 (2004).

[17] D. Bercioux, M. Governale, V. Cataudella, and V. M. Ramaglia, Phys. Rev. Lett. **93**, 056802 (2004).

[18] P. Foldi, B. Molnar, M. G. Benedict, and F. M. Peeters, Phys. Rev. B **71**, 033309 (2005).

[19] U. Aeberhard, K. Wakabayashi, and M. Sigrist, Phys. Rev. B **72**, 075328 (2005).

[VIII] Spin cloud induced around an elastic scatterer by the intrinsic spin-Hall effect:

The spin-Hall effect attracts much interest because it provides a method for manipulating electron spins by electric gates, incorporating thus spin transport into con- ventional semiconductor electronics. As it has been initially predicted, the electric field E induces the spin flux of electrons or holes flowing in the direction perpendicular to E. This spin flux can be due either to the intrinsic spin-orbit interaction (SOI) inherent to a crystalline solid [1], or to spin dependent scattering from impurities [2]. Intrinsic spin-Hall effect corresponding to the former situation has been observed in p-doped 2D semiconductor quantum wells [4], while the extrinsic effect related to the latter scenario has been detected in n-doped 3D semiconductor films [3]. Most of the theoretical studies on the spin-Hall effect (SHE) has been focused on calculation of the spin current (for a review see [5]). On the other hand, since the spin current carries the spin polarization, one would expect a buildup of the spin density near the sample boundaries. Such a spin accumulation near interfaces of various nature was calculated in a number of works [6, 7, 8]. This accumulated polarization is a first evidence of SHE that has been observed experimentally in Ref. [3, 4]. In fact, measuring spin polarization is thus far the only practical way to detect SHE.

[Reference]:

[1] S. Murakami, N. Nagaosa, and S.-C. Zhang, Science 301, 1348 (2003); J. Sinova et. al., Phys. Rev. Lett. **92**, 126603 (2004); D. Culcer et. al., Phys. Rev. Lett. **93**, 046602 (2004).

[2] M. I. Dyakonov, V. I. Perel, Phys. Lett. A 35, 459 (1971); J. E. Hirsch, Phys. Rev. Lett **83**, 1834 (1999).

[3] Y. K. Kato, et. al., Science **306**, 1910 (2004).

[4] J. Wunderlich et. al., Phys. Rev. Lett. **94**, 047204 (2005).

[5] H. -A. Engel, E. I. Rashba, and B. I. Halperin, cond-mat/0603306.

[6] V. M. Galitski et. al., cond-mat/0601677; G. Usaj and C. Balsiero, cond-mat/0405065; ˙I. Adagideli and G.E.W. Bauer, Phys. Rev. Lett. **95**, 256602 (2005).

[7] A. G. Mal'shukov et. al., Phys. Rev. Lett. **95**, 146601 (2005); R. Raimondi et. al., cond-mat/0601525.

[8] B. K. Nikoli´c et. al., Phys. Rev. Lett. **95**, 046601 (2005); Q. Wang et. al., cond-mat/0505576.

三、Results and discussion:

[I] Strain induced coupling of spin current to nanomechanical oscillations [70] (Appendix A).

[II] Visibility of current and shot noise in electrical Mach-Zehnder and Hanbury Brown Twiss interferometers (Appendix B).

[III] dc spin current generation in a Rashba-type quantum channel (Appendix C).

[IV] Effects of elastic scatterer on the dc spin current generation in a Rashba-type channel (Appendix D).

[V] Spin Hall Effect on Edge Magnetization and Electric conductance of a 2D Semiconductor Strip (Appendix E).

[VI] Fano resonance in transport through a mesoscopic two-lead ring (Appendix F).

[VII] Connecting wave functions at a three-legs junction of one-dimensional channels (Appendix G).

[VIII] Spin cloud induced around an elastic scatterer by the intrinsic spin-Hall effect (Appendix H).

Appendix A:

Strain-Induced Coupling of Spin Current to Nanomechanical Oscillations

A. G. Mal'shukov,[1] C. S. Tang,[2] C. S. Chu,[3] and K. A. Chao[4]

[1]*Institute of Spectroscopy, Russian Academy of Science, 142190, Troitsk, Moscow oblast, Russia*
[2]*Physics Division, National Center for Theoretical Sciences, P.O. Box 2-131, Hsinchu 30013, Taiwan, Republic of China*
[3]*Department of Electrophysics, National Chiao Tung University, Hsinchu 30010, Taiwan, Republic of China*
[4]*Solid State Theory Division, Department of Physics, Lund University, S-22362 Lund, Sweden*

(Received 6 May 2005; published 1 September 2005)

We propose a setup which allows us to couple the electron spin degree of freedom to the mechanical motions of a nanomechanical system not involving any of the ferromagnetic components. The proposed method employs the strain-induced spin-orbit interaction of electrons in narrow gap semiconductors. We have shown how this method can be used for detection and manipulation of the spin flow through a suspended rod in a nanomechanical device.

DOI: 10.1103/PhysRevLett.95.107203 PACS numbers: 75.40.Gb, 71.70.Ej, 71.70.Fk, 72.25.−b

An ability to control the spin transport in semiconductors is a key problem to be solved towards implementation of semiconductor spintronics into quantum information processing [1–3]. Many methods have been proposed to achieve control of the electron spin degree of freedom using magnetic materials, external magnetic fields, and optical excitation [for a review see Ref. [3]]. Other promising ideas involve the intrinsic spin-orbit interaction (SOI) in narrow gap semiconductors to manipulate the spin by means of electric fields [4] and electric gates [5–7]. Recently, some of these ideas have been experimentally confirmed [8,9].

In semiconductors the spin-orbit effect appears as an interaction of the electron spin with an effective magnetic field whose direction and magnitude depend on the electron momentum. A specific form of this dependence is determined by the crystal symmetry, as well as by the symmetry of the potential energy profile in heterostructures. In strained semiconductors new components of the effective magnetic field appear due to violation of the local crystal symmetry [10]. The effect of the strain-induced SOI on spin transport was spectacularly demonstrated by Kato *et al.* in their Faraday rotation experiment [9]. An interesting property of the strain-induced SOI is that the strain can be associated with mechanical motion of the solid, in particular, with oscillations in nanomechanical systems (NMS), in such a way making possible the spin-orbit coupling of the electron spin to nanomechanical oscillations. At the same time a big progress in fabricating various NMS [11] allows one to reach the required parameter range to observe subtle effects produced by such a coupling.

In this Letter we will consider NMS in the form of a suspended beam with a doped semiconductor film epitaxially grown on its surface (see Fig. 1). An analysis of the SOI in this system shows that the flexural and torsion vibrational modes couple most efficiently to the electron spin. As a simple example, we will focus on the torsion mode. The strain associated with torsion produces the spin-orbit field which is linear with respect to the electron momentum and is directed perpendicular to it. This field varies in time and space according to respective variations of the torsion strain. Because of the linear dependence on the momentum, the SOI looks precisely as interaction with the spin dependent electromagnetic vector potential. An immediate result of this analogy is that the time-dependent torsion gives rise to a motive force on electrons. Such a force, however, acts in different directions on particles with oppositely oriented spins, inducing thus the spin current in the electron gas. The physics of this phenomenon is very similar to the spin-current generation under time-dependent Rashba SOI, where the time dependence of the SOI coupling parameter is provided by the gate voltage variations [6]. In the present work we will focus, however, on the inverse effect. Because of the SOI coupling, the spin current flowing through the beam is expected to create a mechanical torsion. The torque effect on NMS due to spin flow has been previously predicted by Mohanty *et al.* [12] for a different physical realization, where the torque has

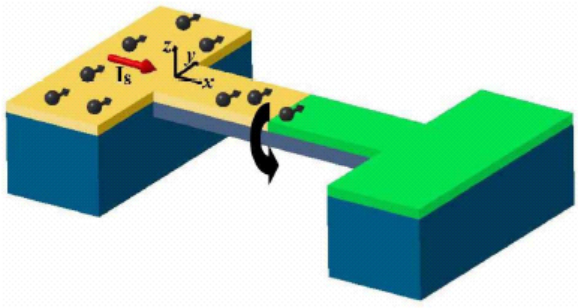

FIG. 1 (color online). Schematic illustration of electromechanical spin-current detector, containing a suspended semiconductor-metal (S-M) rectangular rod atop an insulating substrate (blue). A spin current is injected from the left semiconductor reservoir (yellow) and then diffuses toward the metallic film (green). While passing through the semiconductor film, the spin current induces torque shown by the black arrow.

been created by spin flips at the nonmagnetic-ferromagnetic interface. They also suggested an experimental setup to measure such a small torque. As it will be shown below, the torque due to the strain-induced SOI can be large enough to be measured using the experimental setup proposed in Ref. [12]. Besides this method, other sensitive techniques for displacement measurements can be employed [13].

The system under consideration is a rectangular beam of the total length L_t, width b, and thickness c. The coordinate axes are chosen as shown in Fig. 1. The semiconductor film with the thickness $c/2$ occupies the length L of the beam. The rest part contains a metal film. It can also include some additional elements for detection of the torque, for example, in Ref. [12]. Here we will consider an example when the spin current is created by diffusion of the spin polarization from the left contact in Fig. 1. Therefore, there is no electric current flow through NMS. The spin polarization diffuses towards the metal film which, due to its relatively high conduction, can play an important role as a reservoir for the spin polarization relaxation.

We start from the strain-induced SOI [10] described by the Hamiltonian

$$H_{\mathrm{SO1}} = \alpha[\sigma_x(u_{zx}k_z - u_{xy}k_y) + \sigma_y(u_{xy}k_x - u_{yz}k_z) + \sigma_z(u_{yz}k_y - u_{zx}k_x)] + \beta[\sigma_x k_x(u_{yy} - u_{zz}) + \sigma_y k_y(u_{zz} - u_{xx}) + \sigma_z k_z(u_{xx} - u_{yy})], \quad (1)$$

where u_{ij} are elements of the strain tensor, σ_i stand for Pauli matrices, and k_i denote components of the electron wave vector. In the narrow gap semiconductors the parameter β is usually much smaller than α [10]. Therefore, the term proportional to β will be omitted below. Besides the strain-induced H_{SO1}, the total SOI Hamiltonian also includes the strain independent interaction H_{SO2}. Because of submicron cross-section dimensions of the doped semiconductor film, H_{SO2} will be determined by the bulk Dresselhaus term [14].

$$H_{\mathrm{SO2}} = \delta \sum_{ijn} |\epsilon^{ijn}| k_i (k_j^2 - k_n^2). \quad (2)$$

This interaction, in the range of doping concentrations 10^{17} cm^{-3} and higher, provides the main mechanism for spin relaxation in bulk materials [10].

Since the S-M rod with total length $L_t \gg b$ and c, the major contribution to the strain comes from flexural and torsion motions of the rod [15]. Within the isotropic elastic model, the flexural motions are represented by the diagonal elements u_{xx} and u_{yy} [15] which do not enter into the first square brackets of Eq. (1). On the other hand, due to the crystal anisotropy effects, the u_{xy} components are not zero for such sort of motion and could contribute to Eq. (1). We will consider, however, the simplest example of torsion motions of the rod within an isotropic elastic model. In this case the strain can be represented as [15]

$$u_{yx} = \tau(x)\frac{\partial \chi}{\partial z}; \qquad u_{zx} = -\tau(x)\frac{\partial \chi}{\partial y}; \qquad u_{yz} = 0, \quad (3)$$

where $\tau(x) = \partial\theta/\partial x$ stands for the rate of torsion determined by the torsion angle θ. The function χ depends only on z and y and is uniquely determined by the rod cross-section geometry.

The next step is to derive from the one-particle interaction Eq. (1) a Hamiltonian which describes a coupling of the spin current to the strain. The electron system carrying the spin current can be described by a density matrix $\hat{\rho}$. In the framework of the perturbation theory the leading correction to the electron energy due to the SOI induced strain can be obtained by averaging H_{SO1} with $\hat{\rho}$. In the semiclassical approximation such a procedure can be represented as averaging over the classical phase space with the Boltzmann distribution function $\hat{F}_{\mathbf{k}}(\mathbf{r})$. This function is a 2×2 matrix in the spinor space. One can also define the spin distribution function $P^i_{\mathbf{k}}(\mathbf{r}) = (1/2)\,\mathrm{Tr}\,[\hat{F}_{\mathbf{k}}(\mathbf{r})\sigma^i]$. It is normalized in such a way that the local spin polarization $P^i(\mathbf{r}) = \sum_{\mathbf{k}} \mathbf{P}_{\mathbf{k}}(\mathbf{r})$. We notice that, due to electron confinement in y and z directions, the averages of H_{SO1} containing k_y and k_z turn to zero. Assuming that electron distribution is uniform within the cross section of the semiconductor film one thus obtains, from Eqs. (1) and (3), the SOI energy

$$E_{\mathrm{SO}} = 2\alpha \int_0^L dx \frac{\partial \theta}{\partial x} \sum_{\mathbf{k}} k_x \int dy dz \left(P^y_{\mathbf{k}}(x)\frac{\partial \chi}{\partial z} + P^z_{\mathbf{k}}(x)\frac{\partial \chi}{\partial y} \right). \quad (4)$$

This expression can be further simplified taking into account that χ turns to zero on a free surface [15]. Hence, in the example under consideration $\chi = 0$ on the top and side surfaces of the doped semiconductor film. Consequently, the second term in Eq. (4) vanishes after integration over y. Now Eq. (4) can be expressed in terms of the spin current $J^y(x)$ which is the flux in x direction of y-polarized spins.

$$J^y(x) = S \sum_{\mathbf{k}} v_x P^y_{\mathbf{k}}(x), \quad (5)$$

where $S = bc/2$ is the semiconductor film cross section and v_x is the electron velocity in x direction [16]. Finally, Eq. (4) can be transformed to

$$E_{\mathrm{SO}} = \gamma \int_0^L dx J^y(x) \frac{\partial \theta}{\partial x}. \quad (6)$$

Here the coupling constant γ is given by

$$\gamma = \gamma_0 \int_{-b/2}^{b/2} \chi(y, z = 0) dy, \quad (7)$$

where $\gamma_0 = 2m^*\alpha/\hbar S$.

From the last equation, it is seen that the spin-polarized flow imposes a distributed torque on the rod. In order to study this effect in detail we will neglect, for simplicity, the difference between elastic constants of semiconductor and

metal parts of NMS. As such, the equation of motion for the torsion angle can be then written as

$$I\frac{\partial^2\theta}{\partial t^2} - K\frac{\partial^2\theta}{\partial x^2} - \gamma\frac{\partial}{\partial x}[J^y\eta(L-x)] = 0, \tag{8}$$

where $\eta(x)$ denotes the Heaviside function, K stands for the torsion rigidity, and I is the moment of inertia. It is easy to figure out that the torque imposed by the SOI on NMS can be expressed as

$$\mathcal{T} = \frac{\gamma}{L}\int_0^L dx J^y(x) \equiv \gamma\bar{J}^y, \tag{9}$$

and, for the S-M rod clamped on both ends, the torsion angle at $x = L$

$$\theta_L = \frac{L(L_t - L)}{L_t}\frac{\mathcal{T}}{K}, \tag{10}$$

where L_t is the total length of the rod. From Eq. (8) one can easily see that if the semiconductor film covers the entire length of the beam ($L = L_t$) and the spin current is homogeneous along it, the last term in Eq. (8) turns to 0. Consequently, for a doubly clamped beam the solution of Eq. (8) is $\theta(x) \equiv 0$. In this case, in order to obtain the finite torsion angle, the NMS must include films with different spin-orbit coupling parameters γ, as in Fig. 1 where $\gamma = 0$ in the metal film. On the other hand, if J^y depends on x, as in the example considered below, the metal film is not so necessary. In this example it is shown, however, that such a film can be useful as a reservoir for fast spin relaxation, enhancing thus the diffusive spin-current flow through the beam.

In order to evaluate the torque, let us adopt the following simple model, which is also convenient for an experimental realization. Namely, we assume that the spin current is due to spin diffusion from the left contact. The spin polarization $P^y(0)$ can be created there by various methods ranging from absorption of circularly polarized light to injection from a ferromagnet [3]. One more possibility is the electric spin orientation [9]. For the steady state the diffusion equation reads

$$D_i\frac{d^2P^y}{dx^2} - \frac{P^y}{\tau_i} = 0, \tag{11}$$

where D_i and τ_i are diffusion coefficients and spin relaxation times, with the subscript i indicating the physical quantities in semiconductor ($0 < x < L$) ($i = S$) or metal ($x > L$) ($i = M$) regions. At the semiconductor-metal interface the diffusion current and magnetization $P^y/N_i(0)$ must be continuous, where $N_i(0)$ is the semiconductor or metal density of states at the Fermi energy [17]. We will assume that the length of the metal part of the rod is larger than the spin diffusion length $l_M = \sqrt{D_M\tau_M}$. Therefore, the spin current passes through the semiconductor film and further decays within the metal film. Obviously, in the considered example there is no charge current through the system. Solving the diffusion equation for $l_S \gg L$ and $(\sigma_M L)/(\sigma_S l_M) \gg 1$, where σ_M and σ_S are the 3D conductivities of metal and semiconductor, respectively, we obtain

$$\bar{J}^y = \frac{D_S P^y(0) S}{L}. \tag{12}$$

Since the ratio σ_M/σ_S is very big, Eq. (12) is valid in a broad range of not very small L.

For a numerical evaluation of the spin-orbit torsion effect we take $b = 400$ nm and $c = 200$ nm. The SOI coupling constant $\alpha/\hbar = 4 \times 10^5$ m/sec in GaAs [18]. From Eq. (7) and Ref. [15], it is easy to obtain the spin-current-torsion coupling parameter $\gamma = \gamma_0 k_2 b^3$, where k_2 is a numerical factor depending on the ratio c/b. At $b/c = 2$ the factor $k_2 = 0.03$. For such numerical parameters we find $\gamma = 2.4 \times 10^{-32}$ J sec. It is interesting to compare the torsion effect from the strain-induced SOI with that produced by spin flips at the FM-NM interface [12]. In the latter case $\mathcal{T} = \hbar I_s$, where I_s is of the order of the spin current injected at the FM-NM contact when the electric current passes through it. Comparing this expression with Eq. (9), it is seen that at the *same* spin currents the SOI effect is much stronger, by the factor $\gamma/\hbar \simeq 2.2 \times 10^2$. On the other hand, in [12] the FM-NM contact can be fabricated from all metallic components, while our device must contain the narrow gap semiconductor film. In the former case NMS is able to carry much larger spin current, due to the weaker, by the factor $\sim\sigma_S/\sigma_M$, Joule heating effect. However, the measurement setup suggested by Mohanty *et al.* [12] allows us to measure torsion effects produced by quite weak currents. For example, at $e\bar{J}^y = 10^{-8}$ Amp the torque $\mathcal{T} = 1.5 \times 10^{-21}$ Nm, which is within the sensitivity claimed in [12]. Moreover, the measurement sensitivity can be enhanced [19]. Within our model we can evaluate the spin polarization $P^y(0)$ which can produce a measurable effect on NMS. From Eq. (12), taking $L = 2\ \mu$m, the typical low temperature diffusion constant 300 cm^2/sec, and $n = 10^{17}$ cm^{-3}, one obtains $e\bar{J}^y = 10^4[P^y(0)/n]$ nA. Hence, a measurable 10 nA spin current in NMS can be created by diffusion of spin polarization from an adjacent reservoir containing only 0.1% of spin-polarized carriers. Various methods [3,8,9] are able to provide such and even much larger spin polarization. Higher spin currents are, however, restricted by the heating effects, which depend on the practical design of NMS.

It should be noted that the torsion measurement method of Ref. [12] applies to a time-dependent torque in resonance with a NMS oscillation. For such a measurement the spin current could be modulated in time by a narrow gate between the left contact and the rod, or by varying the spin polarization in the left reservoir, for example, if it is created by absorption of circularly polarized light with modulated intensity.

The static torsion angle at $x = L$ can be found from Eq. (10). On the other hand, the maximum torsion effect is obtained for the time-dependent spin current in resonance with the NMS fundamental oscillation. In this case, the torsion angle θ_L in Eq. (10) must be multiplied by $Q/2$, where Q is the resonance quality factor, which can be quite large in NMS. To observe this torsion angle it must be much larger than the mean amplitude of its thermal fluctuations $\sqrt{\overline{\delta\theta_L^2}}$. For a doubly clamped rod

$$\overline{\delta\theta_L^2} = \frac{k_B T L_t}{\pi^2 K} \sum_{n\geq 1} \frac{1}{n^2} \sin^2\left(\frac{\pi n L}{L_t}\right). \tag{13}$$

For a rectangular cross section with $b/c = 2$, the torsion rigidity $K = 0.057\mu b^3 c$ [15], where $\mu \simeq 3.3 \times 10^{10}$ N/m^2 in GaAs material. Taking $L_t = 5$ μm and all other parameters the same as in the previous paragraph, $Q = 10^4$ and $T = 100$ mK, we obtain the ratio $\delta\theta_L/\theta_L \simeq 4 \times 10^{-2}$ at $e\bar{J}^y = 10$ nA.

We have considered a simple example of the spin-orbit torque effect produced by spin flux in a diffusive 3D semiconductor film. It would be interesting to study other systems, for example, a superlattice of remotely doped high mobility quantum wells in the ballistic regime (L is less than the elastic mean free path). In such a system energy dissipation within the semiconductor film is reduced and, apparently, larger spin currents are allowable.

In summary, we propose a nanomechanical system where due to the strain-induced spin-orbit interaction the electron spin degree of freedom can couple to NMS mechanical motions. We have shown that this coupling is strong enough to induce the measurable torsion in NMS when the spin polarization flows through the suspended nanobeam. Besides a potential for other possible applications, such NMS can be employed as a sensitive detector of spin currents and spin polarizations. The basic structure can be further modified to create devices for eventual use in spintronics as well as spin information processing.

This work was partly funded by the Taiwan National Science Council and RFBR Grant No. 03-02-17452.

[1] *Semiconductor Spintronics and Quantum Computation*, edited by D. D. Awschalom, N. Samarth, and D. Loss (Springer-Verlag, Berlin, 2002).
[2] S. A. Wolf *et al.*, Science **294**, 1488 (2001).
[3] I. Žutić, J. Fabian, and S. Das Sarma, Rev. Mod. Phys. **76**, 323 (2004).
[4] J. Sinova *et al.*, Phys. Rev. Lett. **92**, 126603 (2004); S. Murakami, N. Nagaosa, and S. Zhang, Science **301**, 1348 (2003); V. M. Edelstein, Solid State Commun. **73**, 233 (1990); A. Voskoboynikov, S. S. Liu, and C. P. Lee, Phys. Rev. B **59**, 12514 (1999); L. S. Levitov and E. I. Rashba, Phys. Rev. B **67**, 115324 (2003).
[5] S. Datta and B. Das, Appl. Phys. Lett. **56**, 665 (1990); P. Sharma and P. W. Brouwer, Phys. Rev. Lett. **91**, 166801 (2003); M. Governale, F. Taddei, and R. Fazio, Phys. Rev. B **68**, 155324 (2003).
[6] A. G. Mal'shukov, C. S. Tang, C. S. Chu, and K. A. Chao, Phys. Rev. B **68**, 233307 (2003).
[7] C. S. Tang, A. G. Mal'shukov, and K. A. Chao, Phys. Rev. B **71**, 195314 (2005).
[8] J. Wunderlich, B. Käestner, J. Sinova, and T. Jungwirth, Phys. Rev. Lett. **94**, 047204 (2005).
[9] Y. K. Kato *et al.*, cond-mat/0502627.
[10] G. E. Pikus and A. N. Titkov, in *Optical Orientation*, edited by F. Meier and B. P. Zakharchenya (North-Holland, Amsterdam, 1984).
[11] M. L. Roukes, Phys. World **14**, 25 (2001); H. G. Craighead, Science **290**, 1532 (2000); A. N. Cleland, *Foundations of Nanomechanics* (Springer, New York, 2003).
[12] P. Mohanty, G. Zolfagharkhani, S. Kettemann, and P. Fulde, Phys. Rev. B **70**, 195301 (2004).
[13] R. G. Knobel and A. N. Cleland, Nature (London) **424**, 291 (2003).
[14] G. Dresselhaus, Phys. Rev. **100**, 580 (1955).
[15] L. Landau and E. Lifshitz, *Course of Theoretical Physics* (Pergamon, New York, 1986), 3rd ed., Vol. 7.
[16] We neglected the small correction to the spin current associated with Dresselhaus's term $\frac{\partial H_{SO2}}{\partial \mathbf{k}}$ in the velocity operator, as well as the corresponding correction due to H_{SO1}, within the linear perturbation theory on the strain-induced SOI.
[17] M. Johnson and R. H. Silsbee, Phys. Rev. B **35**, 4959 (1987); **37**, 5312 (1988).
[18] M. I. D'yakonov, V. A. Marushchak, V. I. Perel', and A. N. Titkov, Sov. Phys. JETP **63**, 655 (1986) [Zh. Eksp. Teor. Fiz. **90**, 1123 (1986)].
[19] P. Mohanty (private communication).

Appendix B:

PHYSICAL REVIEW B **72**, 125320 (2005)

Visibility of current and shot noise in electrical Mach-Zehnder and Hanbury Brown Twiss interferometers

V. S.-W. Chung,[1,2] P. Samuelsson,[3] and M. Büttiker[1]
[1]*Département de Physique Théorique, Université de Genève, Genève 4, CH-1211, Switzerland*
[2]*Department of Electronics, National Chiao-Tung University, Hsinchu 30010, Taiwan*
[3]*Division of Solid State Theory, Lund University, Sölvegatan 14 A, S-223 62 Lund, Sweden*
(Received 20 May 2005; published 14 September 2005)

We investigate the visibility of the current and shot-noise correlations of electrical analogs of the optical Mach-Zehnder interferometer and the Hanbury Brown Twiss interferometer. The electrical analogs are discussed in conductors subject to high magnetic fields where electron motion is along edge states. The transport quantities are modulated with the help of an Aharonov-Bohm flux. We discuss the conductance (current) visibility and shot noise visibility as a function of temperature and applied voltage. Dephasing is introduced with the help of fictitious voltage probes. Comparison of these two interferometers is of interest since the Mach-Zehnder interferometer is an amplitude (single-particle) interferometer, whereas the Hanbury Brown Twiss interferometer is an intensity (two-particle) interferometer. A direct comparison is only possible for the shot noise of the two interferometers. We find that the visibility of shot noise correlations of the Hanbury Brown Twiss interferometer as a function of temperature, voltage or dephasing, is qualitatively similar to the visibility of the first harmonic of the shot noise correlation of the Mach-Zehnder interferometer. In contrast, the second harmonic of the shot noise visibility of the Mach-Zehnder interferometer decreases much more rapidly with increasing temperature, voltage or dephasing rate.

DOI: 10.1103/PhysRevB.72.125320 PACS number(s): 73.23.−b, 72.10.−d, 72.70.+m, 73.43.−f

I. INTRODUCTION

With the advent of mesoscopic physics, it has become possible to experimentally investigate quantum phase coherent properties of electrons in solid state conductors in a controlled way. In particular, in ballistic mesoscopic samples at low temperatures, electrons can propagate up to several microns without loosing phase information. This opens up the possibility of investigating electrical analogs of various optical phenomena and experiments. An investigation of such analogs is of fundamental interest. On the one hand, it allows one to establish similarities between the properties of photons and conduction electrons, a consequence of the wave nature of the quantum particles. On the other hand, it also allows one to investigate the differences between the two types of particles arising from the different quantum statistical properties of fermions and bosons. For many-particle properties, such as light intensity correlations or correspondingly electrical current correlations, noise, the quantum statistical properties are important.[1,2] Both the wave-nature of the particles as well as their quantum statistics are displayed in a clearcut fashion in interferometer structures. In this work we are concerned with the electrical analogs of two well known optical interferometers, the single-particle Mach-Zehnder (MZ) interferometer and the two-particle Hanbury Brown Twiss (HBT) interferometer.

The MZ-interferometer is a subject of most textbooks in optics.[3] In the framework of quantum optics, considering individual photons rather than classical beams of light, the interference arises due to the superposition of the amplitudes for two different possible paths of a single photon. This leads to an interference term in the light intensity. The MZ-interferometer is thus a prime example of a single particle interferometer.[4] Various electronic interferometers with ballistic transport of the electrons have been investigated experimentally over the last decades, as e.g. Aharonov-Bohm (AB) rings[5] and double-slit interferometers.[6] Detailed investigations of dephasing in ballistic interferometers was carried out in Refs. 7 and 8. Only very recently was the first electronic MZ-interferometer realized by Ji *et al.*[9] in a mesoscopic conductor in the quantum Hall regime. A high visibility of the conductance oscillations was observed, however the visibility was not perfect. This led the authors to investigate in detail various sources for dephasing. As a part of this investigation, also shot noise was measured. Still, some aspects of the experiment are not yet fully understood. Theoretically, Seelig and one of the authors[10] investigated the effect of dephasing due to Nyquist noise on the conductance in a MZ-interferometer. The effect of dephasing on the closely related four-terminal resistance in ballistic interferometers[11] was investigated as well. Dephasing in ballistic strongly interacting systems is discussed by Le Hur.[12,13] Following the experimental work of Ji *et al.*,[9] Marquardt and Bruder investigated the effect of dephasing on the shot-noise in MZ-interferometers, considering dephasing models based on both classical[14,15] as well as quantum fluctuating fields.[16] Very recently, Förster, Pilgram and one of the authors[17] extended the dephasing model of Refs. 10 and 14 to the full statistical distribution of the transmitted charge.

The HBT-interferometer[18–20] was originally invented for stellar astronomy, to measure the angular diameter of stars. It is an intensity, or two-particle,[4] interferometer. The interference arises from the superposition of the amplitudes for two different two-particle processes. Importantly, there is no single particle interference in the HBT-interferometer. Consequently, in contrast to the MZ-interferometer there is no

interference in the light intensity, the interference instead appears in the intensity-intensity correlations. Moreover, the intensity-intensity correlation also displays the effect of quantum statistics. Photons originating from thermal sources tend to bunch, giving rise to positive intensity cross correlations. For the electronic analog of the HBT-interferometer, it was the corresponding antibunching of electrons that originally attracted interest. It was predicted[1] that the electrical current cross correlations in mesoscopic conductors would be manifestly negative, i.e., display antibunching, as a consequence of the fermionic statistics of the electrons. Negative current cross correlations were subsequently observed in two independent experiments.[21,22] Recently, antibunching for field emitted electrons in vacuum was also demonstrated.[23] The two-particle interference in the HBT-experiment has received much less attention. We emphasize that while the bunching of the photons was necessary for obtaining a finite, positive cross correlation signal, it was the two-particle effect that was of main importance to HBT since the angular diameter of the star was determined from the two-particle interference pattern. In electrical conductors, two-particle effects in AB-interferometers were investigated theoretically in Refs. 24–26. Only very recently two of the authors and Sukhorukov[27] proposed a direct electronic analog of the optical HBT-interferometer which permits to demonstrate two-particle interference in an unambiguous way.

In this work we investigate and compare in detail the current and and zero-frequency noise in electronic MZ and HBT interferometers. We consider interferometers implemented in mesoscopic conductors in the integer quantum Hall regime, where the transport takes place along single edge states and quantum point contacts (QPC's) serve as controllable beamsplitters. The effect of finite temperature, applied bias and asymmetry, i.e., unequal length of the interferometer arms, is investigated. The strength of the interference contribution is quantified via the visibility of the phase oscillations. The dependence of the visibility on the beamsplitter transparencies as well as on the temperature, voltage and asymmetry is discussed in detail. Of interest is the comparison of visibility of the shot-noise correlation of the MZ-interferometer and the HBT-intensity interferometer. Shot noise correlations in the MZ-interferometer exhibit two contributions, one with the fundamental period of h/e and a second harmonic with period $h/2e$. The shot noise correlations in the HBT-interferometer, even though they are due to two particle processes, are periodic with period h/e. Thus the Aharonov-Bohm period can not be used to identify the two particle processes which give rise to the HBT effect. It is therefore interesting to ask whether the HBT two-particle processes have any other signature, for instance in the temperature or voltage dependence of the visibility of the shot-noise correlation. We find that this is not the case. To the contrary, we find that the shot noise correlations in the HBT intensity interferometer behave qualitatively similar to the h/e shot noise correlation in the MZ-interferometer. In contrast the $h/2e$ contribution in the shot noise of the MZ-interferometer decreases more rapidly with increasing temperature, voltage or dephasing rate than the h/e oscillation in the MZ-or HBT-interferometer.

We investigate dephasing of the electrons propagating along the edge states by connecting one of the interferometer arms to a fictitious, dephasing voltage probe. In all cases, the current and noise of the MZ-interferometer as well as the noise in the HBT-interferometer, the effect of the voltage probe is equivalent to the effect of a slowly fluctuating phase.

II. MODEL AND THEORY

A. Optical analogs in the quantum Hall regime

In the paper we consider implementations of the MZ and HBT interferometers in mesoscopic conductors in strong magnetic fields, in the integer quantum Hall regime.[28] The typical system is a two-dimensional electron gas in a semiconductor heterostructure, with the lateral confinement of the electron gas controllable via electrostatic gating. The transport between reservoirs[29] connected to the conductor takes place along edge states.[30] The edge states, quantum analogs of classical skipping orbits, are chiral, the transport along an edge state is unidirectional. Scattering between edge states is suppressed everywhere in the conductor except at electrostatically controllable constrictions, QPC's.[31,32] For a magnetic field that does not break the spin degeneracy of the edge states, each edge state supplies two conduction modes, one per spin.

These properties make conductors in the integer quantum Hall regime ideal for realizing analogs of optical experiments. First, the edge states correspond to single mode waveguides for the light. The unidirectional motion along the edge states allows for "beams" of electrons to be realized. Second, the QPC's work as electronic beam splitters with controllable transparency. Moreover, due to chirality the beamsplitters are reflectionless, a property essential for the MZ and HBT interferometers but difficult to achieve for beam splitters in conductors in weak (or zero) magnetic fields.[22,33] These properties of conductors in the quantum Hall regime have been demonstrated experimentally in a number of works, see e.g., Refs. 9, 21, and 34.

Theoretically, several works have been concerned with the conductance and noise properties of beamsplitters and interferometers in quantum Hall systems, for a recent reviews see, e.g., Refs. 2 and 35. Recently, it was proposed to use these appealing properties of edge states in the context of orbital[36] quasiparticle entanglement in static[27,37,38] and dynamic[39,40] systems as well as for quantum state transfer.[41]

It is interesting to note that the edge state description also hold for conductors at even higher magnetic fields, in the fractional quantum Hall regime. As examples, the fractional charge has been determined in shot-noise experiments[42,43] and the quantum statistical properties of the fractionally charged quasiparticles have been investigated theoretically in beamsplitter,[44] and HBT (Ref. 45) geometries. Various interferometer structures have also been considered.[46–48] Very recently, a MZ-interferometer in the fractional Quantum Hall regime was proposed.[49] In this work we however consider only the integer quantum Hall effect, where the quasiparticles are noninteracting and the electrical analogs to optical experiments can be directly realized.

B. Scattering approach to current and noise

This discussion leads us to consider single mode, multiterminal conductors with noninteracting electrons. The prin-

ciple aim of this work is a comparison of the MZ and HBT-interferometers. In reality in both interferometers interactions (screening) play a role both for the voltage and temperature dependence. A noninteracting scattering approach is not gauge invariant but requires a treatment of screening.[50] However, these effects are expected to be simliar in the two interferometers and will not affect the main conclusions of this work. Therefore, below we treat noninteracting quasiparticle interferometers. The conductors are connected to several electronic reservoirs, biased at a voltage eV or grounded. The current[51] and the noise[1,52] are calculated within the scattering approach for multiterminal conductors. We first introduce the creation and annihilation operators for ingoing, $\hat{a}_\alpha^\dagger(E)$ and $\hat{a}_\alpha(E)$, and outgoing, $\hat{b}_\alpha^\dagger(E)$ and $\hat{b}_\alpha(E)$, particles, at energy E in terminal α. For simplicity we suppress spin notation. Considering a conductor with N terminals, the in- and outgoing annihilation operators are related via the $N\times N$ scattering matrix, as

$$\hat{b}_\alpha(E) = \sum_{\beta=1}^{N} s_{\alpha\beta}(E)\hat{a}_\beta(E), \tag{1}$$

where $s_{\alpha\beta}(E)$ is the amplitude to scatter from terminal β to terminal α. The current operator in the lead α has the form[51]

$$\hat{I}_\alpha(t) = \frac{e}{h}\sum_{\beta\gamma}\int dE dE' \exp(i[E-E']t/\hbar) \times A^\alpha_{\beta\gamma}(E,E')\hat{a}^\dagger_\beta(E)\hat{a}_\gamma(E'), \tag{2}$$

with the notation

$$A^\alpha_{\beta\gamma}(E,E') = \delta_{\alpha\beta}\delta_{\alpha\gamma} - s^*_{\alpha\beta}(E)s_{\alpha\gamma}(E'). \tag{3}$$

The average current is given by[51]

$$\langle I_\alpha\rangle = \int dE j_\alpha(E), \tag{4}$$

where the spectral current density is

$$j_\alpha(E) = \frac{1}{e}\sum_\beta G_{\alpha\beta}(E) f_\beta(E). \tag{5}$$

Here $f_\beta(E)=1/(1+\exp[(E-\mathrm{eV}_\beta)/k_BT])$ is the Fermi Dirac distribution of terminal β, with V_β the corresponding applied voltage. The spectral conductance $G_{\alpha\beta}(E)$ is given by

$$G_{\alpha\beta}(E) = \frac{e^2}{h}A^\alpha_{\beta\beta}(E,E). \tag{6}$$

The zero frequency correlator between current fluctuations in terminals α and β is defined as

$$S_{\alpha\beta} = \int dt \langle \Delta\hat{I}_\alpha(0)\Delta\hat{I}_\beta(t) + \Delta\hat{I}_\beta(t)\Delta\hat{I}_\alpha(0)\rangle, \tag{7}$$

where $\Delta\hat{I}_\alpha(t)=\hat{I}_\alpha(t)-\langle\hat{I}_\alpha(t)\rangle$. The current correlator is given by[1,52]

$$S_{\alpha\beta} = \int dE S_{\alpha\beta}(E), \tag{8}$$

where

$$S_{\alpha\beta}(E) = \frac{2e^2}{h}\sum_{\gamma\delta} A^\alpha_{\gamma\delta}(E,E)A^\beta_{\delta\gamma}(E,E)f_\gamma(E)[1-f_\delta(E)] \tag{9}$$

is the spectral current correlator.

C. Dephasing voltage probe model

There are several physical mechanisms that might lead to dephasing of the electrons propagating along the edge states (see e.g., the discussion in Ref. 9). In this work we are not interested in any particular mechanism for dephasing but consider instead a phenomenological model, a dephasing voltage probe. The idea of using a voltage probe to induce dephasing was introduced in Refs. 53 and 54. A voltage probe connected to a mesoscopic sample was considered, leading to a suppression of coherent transport due to inelastic scattering. The probe model, originally considered for the average current, was extended to treat the effect of inelastic scattering on shot noise by Büttiker and Beenakker[55] by considering a conservation of current fluctuations at the probe as well. Later De Jong and Beenakker[56] extended the voltage probe concept and introduced a (fictitious) voltage probe which breaks phase but does not dissipate energy. Scattering in the voltage probe is (quasi-)elastic. This is achieved with the help of a distribution function in the voltage probe which conserves not only total current like a real voltage probe, but conserves current in every small energy interval. Such a probe provides a model of pure dephasing. The different probe models have been used as qualitative models in a number of works, see Refs. 2 and 57 for a review. For an application to quantum Hall systems, see Ref. 58.

In this work we consider the dephasing voltage probe model, which conserves the current at each energy. The model is based on the assumption that the current is conserved on a time scale τ_C, much shorter than the time of the measurement but much longer than the time between injection of individual electrons, here of the order of $\hbar$/eV. One could however consider a more general voltage probe model that takes into account a more complicated dynamics of the probe. A detailed discussion of such a general model in the light of recent work[14,15,59,60] is however deferred to a later work. Here we only note that below we find that the voltage probe in both the MZ and HBT-interferometers only gives rise to a suppression of the phase dependent terms in conductance and noise, just as one would naively expect to be the effect of pure dephasing.

The condition of zero current into the fictitious probe γ at each energy is fulfilled by considering a time dependent distribution function of the probe

$$f_\gamma(E,t) = \bar{f}_\gamma(E) + \delta f_\gamma(E,t), \tag{10}$$

where $\delta f_\gamma(E,t)$ fluctuates to conserve current on the timescale τ_C. As a consequence, the spectral current density at each energy in lead α fluctuates in time as

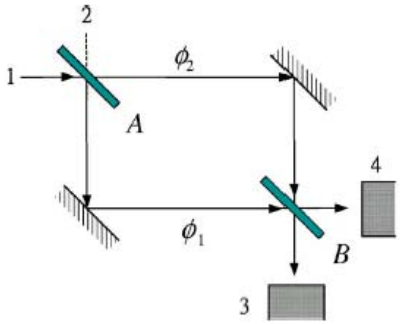

FIG. 1. (Color online) An optical Mach-Zehnder interferometer. A beam of light incident from 1 is split in two partial beams at the semitransparent beamsplitter A. The two partial beams acquire geometrical phases ϕ_1 and ϕ_2, respectively, and are rejoined at the second beamsplitter B. The light intensity is measured in detectors 3 and 4.

$$j_\alpha(E,t) = j_\alpha(E) + \Delta j_\alpha(E,t), \tag{11}$$

where the fluctuations $\Delta j_\alpha(E,t) = \delta j_\alpha(E,t) + (1/e)G_{\alpha\gamma}(E)\delta f_\gamma(E,t)$ consist of two parts, the intrinsic fluctuations $\delta j_\alpha(E,t)$ and the additional fluctuations due to $\delta f_\gamma(E,t)$. The requirement of zero average current into the probe, $j_\gamma(E)=0$, leads to the averaged distribution function at the probe reservoir γ

$$\bar{f}_\gamma(E) = -\sum_{\alpha\neq\gamma} \frac{G_{\gamma\alpha}(E)}{G_{\gamma\gamma}(E)} f_\alpha(E). \tag{12}$$

The average spectral current density $j_\alpha^{\mathrm{dp}}(E)$ is then found from Eq. (5).

The fluctuating part of the distribution function, $\delta f_\gamma(E,t)$, is obtained from the requirement of zero current fluctuations into the probe, $\Delta j_\gamma(E,t) = \delta j_\gamma(E,t) + (1/e)G_{\gamma\gamma}(E)\delta f_\gamma(E,t) = 0$. The total current density fluctuation is then given by

$$\Delta j_\alpha(E,t) = \delta j_\alpha(E,t) - \frac{G_{\alpha\gamma}(E)}{G_{\gamma\gamma}(E)} \delta j_\gamma(E,t). \tag{13}$$

As a result, in the presence of dephasing the total spectral current correlation $S_{\alpha\beta}^{\mathrm{dp}}(E)$ is

$$S_{\alpha\beta}^{\mathrm{dp}}(E) = S_{\alpha\beta}(E) - \frac{G_{\alpha\gamma}(E)}{G_{\gamma\gamma}(E)} S_{\beta\gamma}(E) - \frac{G_{\beta\gamma}(E)}{G_{\gamma\gamma}(E)} S_{\alpha\gamma}(E) + \frac{G_{\alpha\gamma}(E)G_{\beta\gamma}(E)}{G_{\gamma\gamma}^2(E)} S_{\gamma\gamma}(E), \tag{14}$$

where $S_{\alpha\beta}(E)$ is the correlation function between the intrinsic current fluctuations, δj_α and δj_β, of contact α and β, given by Eq. (9), and $G_{\alpha\beta}(E)$ is the conductance, given by Eq. (6).

III. MACH-ZEHNDER INTERFEROMETERS

A schematic of the MZ-interferometer is shown in Fig. 1. An incident beam of light from source 1 is divided in two parts at the semitransparent beamsplitter A. The two partial beams are reflected at mirrors and later joined at the second beamsplitter B. Beams of light going out from B are detected in 3 and 4. The amplitude of the light in an outgoing beam is the sum of the amplitudes for the two partial beams, $A = A_1 \exp(i\phi_1) + A_2 \exp(i\phi_2)$. This gives an intensity $|A|^2 = |A_1|^2 + |A_2|^2 + 2\,\mathrm{Re}\{A_1 A_2^* \exp(i[\phi_1 - \phi_2])\}$. The interference term $2\,\mathrm{Re}\{A_1 A_2^* \exp(i[\phi_1 - \phi_2])\}$ thus contains the difference between the geometrical phases, $\phi_1 - \phi_2$. Importantly, the four terminal geometry together with the reflectionless beamsplitters lead to an incident beam that traverses the interferometer only once. This is a defining property of the MZ-interferometer.

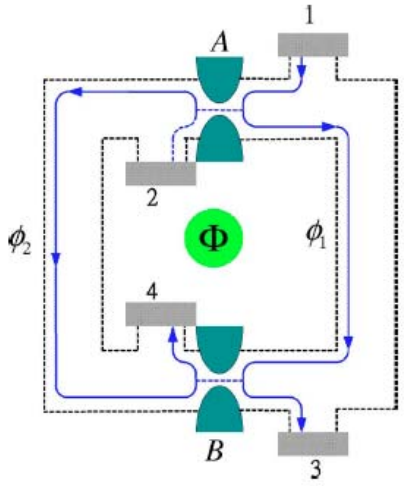

FIG. 2. (Color online) The electronic analog of the MZ-interferometer, implemented by Ji *et al.* (Ref. 9) in a conductor in the quantum Hall regime. The electronic reservoir 1 is biased at eV and reservoirs 2–4 are kept at ground. The edge states (solid lines) have a direction of transport indicated by arrows. The QPC's A and B play the role of the beam splitters in Fig. 1. Geometrical phases ϕ_1 and ϕ_2 and the AB-flux Φ are shown.

We then turn to the electric analog of the MZ-interferometer, shown in Fig. 2. As pointed out above, several results for the current and noise are available in the literature.[10,11,14–17] Here we analyze the most general situation possible, with finite voltage, temperature, and interferometer arm asymmetry as well as different beamsplitters A and B with arbitrary transparency. When we consider limiting cases, e.g., small temperature, bias or asymmetry, known results are recovered. This detailed analysis of the MZ-interferometer is of importance when comparing to the HBT-interferometer below.

We first discuss a fully coherent interferometer, the effect of dephasing is investigated below. An electric potential eV is applied at terminal 1, all other terminals are kept at zero potential. The injected electrons propagate along single edge states. Scattering between the edge states can take place only at the two QPC's, acting as beamsplitters with controllable transparency. The beamsplitters $j=A,B$ are characterized by the scattering matrices

$$\begin{pmatrix} i\sqrt{R_j} & \sqrt{\mathcal{T}_j} \\ \sqrt{\mathcal{T}_j} & i\sqrt{R_j} \end{pmatrix}, \tag{15}$$

where $\mathcal{T}_j$ and $R_j=1-\mathcal{T}_j$ are the transmission and reflection probabilities, respectively. We note that any additional phases of the beamsplitters just give rise to a constant phase shift of the oscillations in the interference terms and are therefore not considered.

Propagating along the edge states, the electrons pick up geometrical phases ϕ_1 and ϕ_2 as well as phases ψ_1 and ψ_2 due to the AB-flux Φ through the center of the interferometer. For example, the amplitude for scattering from terminal 1 to 4 is given by

$$s_{41} = i\sqrt{\mathcal{T}_B R_A} e^{i(\phi_1+\psi_1)} + i\sqrt{\mathcal{T}_A R_B} e^{i(\phi_2-\psi_2)}. \tag{16}$$

For the geometrical phases, to be specific we consider the case when the potential landscape $eU(x,y)$ of the conductor in Fig. 2 is varying smoothly on the scale of the magnetic length $l_B=(\hbar/e|B|)^{1/2}$, with $B\hat{z}$ the applied magnetic field perpendicular to the plane in Fig. 2 (the effect of selfconsistency of the potential[61] is neglected). This allows for a semiclassical treatment.[62] In a high magnetic field the edge states at Fermi energy E_F follow equipotential lines determined by $eU(x,y)=E_F-\hbar\omega_c(n+1/2)$ where $\omega_c=eB/m$ is the cyclotron frequency and m the effective electron mass. We are concerned here with the case where there is only one edge state and thus $n=0$. Suppose the x-axis is a line intersecting quantum point contacts A and B in Fig. 2. Excluding self-intersections we can express the edge state in terms of functions $y_1(x)$ and $y_2(x)$ for the left and right path of the interferometer. Working in the symmetric gauge, the geometric phases can be written[62] $\phi_i=-l_B^{-2}\int_{x_A}^{x_B} dx y_i(x)$, where x_A and x_B are the locations of the QPC's. Importantly, $\phi_1-\phi_2$ corresponds to the total area A enclosed by these two paths divided by the magnetic length squared, or $\phi_1-\phi_2=2\pi BA/\Phi_0$, where BA is the total flux through the enclosed area and $\Phi_0=h/e$ the elementary flux quantum. Note that the Aharonov-Bohm flux Φ adds an additional phase ψ_1 and ψ_2, with $\psi_1+\psi_2=2\pi\Phi/\Phi_0$, to each of the paths.

For the discussion of the temperature and voltage dependence of the current and the noise, we also need to know the energy dependence of the phases. First, instead of parameterizing the edge state through x we introduce the parameter s which measures directly the path length, i.e., $x(s), y(s)$. In addition at s we introduce local coordinates $s_\parallel$ along and $s_\perp$ perpendicular to the equipotential line. In these coordinates, an edge state that follows the equipotential line at a small energy E away from E_F acquires the additional phase $\Delta\phi=-l_B^{-2}\int ds\Delta s_\perp$ with $e(dU/ds_\perp)\Delta s_\perp=E$. The potential gradient $dU/ds_\perp$ determines the local electric field $F(s)=-dU/ds_\perp$ at s. But $eF(s)l_B^2=\hbar v_D(s)$, where $v_D(s)=F(s)/B$ is the drift velocity of the guiding center of the cyclotron orbit at point s of the edge state. Thus a small increase in energy leads to a phase increment given by $\Delta\phi_i=\int ds[1/\hbar v_D(s_i)]E$. A rough estimate using a drift velocity which is constant along the edge gives $\Delta\phi_i\approx(L_i/\hbar v_D)E$ with L_i the length of the edge state i. For the phase-difference of the two interfering paths we have

$$\phi_1(E)-\phi_2(E)=\Delta\phi(E_F)+E/E_c \tag{17}$$

with $\Delta\phi(E_F)=\phi_1(E_F)-\phi_2(E_F)$ the equilibrium phase difference. Formally, higher order terms in energy can be neglected for characteristic energies k_BT and eV much smaller than $(dU/ds_\perp)^2/[d^2U/ds_\perp^2]$. The asymmetry of the two edges thus gives rise to an energy scale $E_c=\{\int ds[1/\hbar v_D(s_1)]-\int ds[1/\hbar v_D(s_2)]\}^{-1}$ which is due to the mismatch of the edge state path lengths, i.e., $E_c\approx\hbar v_D/(\Delta L)$ with $\Delta L=L_1-L_2$. In principle, for a completely symmetric interferometer one has $E_c\to\infty$.

Given the scattering amplitudes $s_{\alpha\beta}$, the spectral current density is found from Eqs. (3), (5), and (6). For example, terminal 4, one gets

$$j_4(E)=(e/h)[f(E)-f_0(E)][\mathcal{T}_A R_B+\mathcal{T}_B R_A + 2\sqrt{\mathcal{T}_A\mathcal{T}_B R_A R_B}\cos(E/E_c+\Theta)], \tag{18}$$

where we introduce the total, energy independent phase $\Theta=\Delta\phi(E_F)+2\pi\Phi/\Phi_0$. Here $f_0(E)$ is the distribution functions of the grounded terminals 2, 3, and 4 and $f(E)=f_0(E-\mathrm{eV})$ the distribution function of terminal 1. The current is then given from Eq. (4), as

$$I_4=\frac{e}{h}\left[(\mathcal{T}_A R_B+\mathcal{T}_B R_A)\mathrm{eV}+\sqrt{\mathcal{T}_A\mathcal{T}_B R_A R_B}\times 4\pi k_BT\,\mathrm{csch}\left(\frac{k_BT\pi}{E_c}\right)\sin\left(\frac{\mathrm{eV}}{2E_c}\right)\cos\left(\frac{\mathrm{eV}}{2E_c}+\Theta\right)\right]. \tag{19}$$

Current conservation gives $I_3=(e^2/h)V-I_4$. The current consists of two physically distinct parts. The first term in Eq. (19) is the phase independent, incoherent part, the current in the absence of interference, while the second, phase dependent term is the interference contribution. We note that a bias eV of the order of the asymmetry energy E_c leads to the phase shifts of the oscillation. The strength of the interference can conveniently be quantified via the visibility as

$$\nu_I=\frac{I_{\max}-I_{\min}}{I_{\max}+I_{\min}}=\frac{\mathrm{amp}[I]}{\langle I\rangle}, \tag{20}$$

which gives for the current in the MZ-interferometer

$$\nu_{I,\mathrm{MZ}}=\frac{\sqrt{\mathcal{T}_A\mathcal{T}_B R_A R_B}}{\mathcal{T}_A R_B+\mathcal{T}_B R_A}\frac{4\pi k_BT}{\mathrm{eV}}\,\mathrm{csch}\left(\frac{k_BT\pi}{E_c}\right)\left|\sin\left(\frac{\mathrm{eV}}{2E_c}\right)\right|. \tag{21}$$

The visibility is a product of a term containing the QPC scattering probabilities and a function depending on the energy scales k_BT, eV, and E_c. The scattering probability term is maximum for identical QPC's, $\mathcal{T}_A=\mathcal{T}_B$. The energy scale dependence is shown in Fig. 3 where the visibility for identical point contacts is plotted as a function of the normalized temperature, k_BT/E_c. We note several interesting features from Fig. 3 and Eq. (21). (i) the visibility shows decaying oscillations as a function of voltage $\nu_{I,\mathrm{MZ}}\propto|\sin(\mathrm{eV}/2E_c)|/\mathrm{eV}$ for arbitrary temperature. (ii) A symmetric MZ-interferometer, $E_c\gg k_BT$, eV, has unity visibility (for

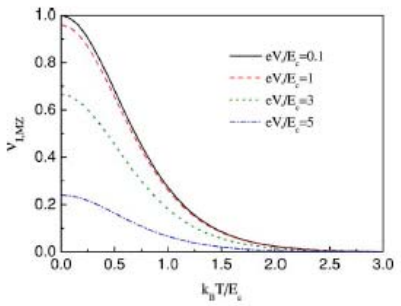

FIG. 3. (Color online) Current visibility of the Mach-Zehnder interferometer $\nu_{I,MZ}$ versus normalized temperature k_BT/E_c for $\mathcal{T}_A = \mathcal{T}_B$.

$\mathcal{T}_A = \mathcal{T}_B$), i.e., shows perfect interference. (iii) The visibility decays monotonically with increasing temperature. For large temperatures, $k_BT \gg E_c$, the visibility decays exponentially with the temperature as $\nu_{I,MZ} \propto k_BT \exp(-\pi k_BT/E_c)$.

It is interesting to compare the calculated visibility to the experimentally measured one in Ref. 9. As already shown in Ref. 9, the measured scattering probability dependence of $\nu_{I,MZ}$ is well reproduced by Eq. (21). For the energy scale dependence, no information about the drift velocity v_D or the asymmetry ΔL needed to determine E_c is provided in Ref. 9. However, to obtain the order of magnitude of E_c, considering as a rough estimate a typical drift velocity[63] $v_D \sim 10^4$ m/s at a magnetic field $B \sim 1$ T and an asymmetry $\Delta L \sim 0.1$ μm gives an E_c corresponding to an applied bias ~ 10 μV or a temperature ~ 100 mK. These values are typically of the same order of magnitude as the ones considered in the experiment. As a first approximation, one would thus expect asymmetry effects to be of importance. The observed temperature dependence, a strong decrease of the visibility for increased temperature, is also qualitatively described by Eq. (21) with an $E_c/k_B \sim 50$ mK. This is however not the case with the voltage dependence. Ji *et al.* find a differential visibility, i.e., the visibility of $dI(V)/dV$, which decays strongly with applied voltage, while Eq. (19) predicts a constant, voltage independent differential visibility. There are several possible explanations to why the voltage dependence in contrast to the temperature dependence is not reproduced by the theory. Ji *et al.* themselves point out two voltage dependent dephasing mechanism: low frequency noise of $1/f$ type due to moving impurities, induced by a higher current and fast fluctuations of the potential landscape (and hence of the phase via the enclosed area) caused by screening of the additional charges injected at higher current. Screening might also, for the nonlinear current-voltage characteristics predicted by Eq. (19), lead to a voltage dependent renormalization of the transmission probabilities, introducing a voltage dependence in the differential visibility.[50,64] We also note that in the model of Ref. 16, inducing dephasing by coupling the MZ-interferometer to a quantum bath, gives a dephasing rate that increases with increasing voltage. Clearly, further investigations are needed to clarify the origin of the dephasing in the experiment in Ref. 9.

Turning to the noise, we focus on the cross correlator between currents flowing in terminals 3 and 4 (the autocorrelator can be obtained analogously). This allows for a straightforward comparison to the result of the HBT-interferometer, for which the cross correlator was investigated in Ref. 27. From Eqs. (8) and (9) and the expressions for the scattering amplitudes, we arrive at the noise spectral density

$$S_{34}(E) = \frac{-2e^2}{h}[f(E) - f_0(E)]^2 \left\{ c_0 + c_\Theta \cos\left(\frac{E}{E_c} + \Theta\right) + c_{2\Theta} \cos\left(2\left[\frac{E}{E_c} + \Theta\right]\right)\right\}, \tag{22}$$

with coefficients

$$c_0 = \mathcal{T}_A R_A + \mathcal{T}_B R_B - 6\mathcal{T}_A R_A \mathcal{T}_B R_B,$$

$$c_\Theta = 2(\mathcal{T}_A - R_A)(\mathcal{T}_B - R_B)\sqrt{\mathcal{T}_A \mathcal{T}_B R_A R_B},$$

$$c_{2\Theta} = 2\mathcal{T}_A \mathcal{T}_B R_A R_B. \tag{23}$$

Performing the energy integrals in Eq. (8) we find for the cross correlator

$$S_{34} = -\frac{2e^2}{h}\left\{ c_0 \bar{S}_0 + c_\Theta \bar{S}_\Theta \cos\left(\frac{\mathrm{eV}}{2E_c} + \Theta\right) + c_{2\Theta} \bar{S}_{2\Theta} \cos\left[2\left(\frac{\mathrm{eV}}{2E_c} + \Theta\right)\right]\right\}, \tag{24}$$

where we introduce the functions

$$\bar{S}_0 = \mathrm{eV} \coth \frac{\mathrm{eV}}{2k_BT} - 2k_BT, \tag{25}$$

and

$$\bar{S}_{m\Theta} = 2\pi k_BT \,\mathrm{csch}\left(\frac{m\pi k_BT}{E_c}\right)\left[\coth\left(\frac{\mathrm{eV}}{2k_BT}\right)\sin\left(\frac{m\mathrm{eV}}{2E_c}\right) - \frac{mk_BT}{E_c}\cos\left(\frac{m\mathrm{eV}}{2E_c}\right)\right] \tag{26}$$

with $m = 1, 2$, containing the dependence on the energy scales eV, k_BT, and E_c.

Just as the current in Eq. (19), the noise consists of a phase independent, incoherent part and a phase dependent, interference part. However, in contrast to the current, the phase dependent part of the noise contains two terms with different periods in Θ, corresponding to oscillations periodic in h/e and $h/2e$. These terms result from two-particle scattering processes which enclose the AB-flux one and two times respectively. Similarly to the current, the phase of the oscillations are shifted for a bias eV of the order of the asymmetry energy E_c.

It is important to note that in the MZ (in contrast to the HBT) interferometer, two particle and higher order scattering processes are just products of single particle scattering processes. The full distribution of current fluctuations[17] is thus a function of single particle scattering probabilities only. In particular, the noise spectral density $S_{34}(E)$ in Eq. (22) is proportional to $-|s_{41}|^2|s_{31}|^2$, i.e., partition noise[1] with phase dependent scattering probabilities. As a consequence, the

phase independent, incoherent part of the noise cannot be understood as partition noise from incoherent single particle processes, i.e., $\langle|s_{41}|^2\rangle_{\rm inc}\langle|s_{31}|^2\rangle_{\rm inc} \neq \langle|s_{41}|^2|s_{31}|^2\rangle_{\rm inc}$. This is formally clear since the term proportional to $\cos^2\Theta=[1+\cos(2\Theta)]/2$, from two coherent scattering processes, obviously contribute to the phase independent part of the noise. As a consequence, as shown by Marquardt and Bruder,[14,15] a model[2] with a filled stream of classical particles injected from reservoir 1 correctly reproduces the incoherent part of the current but fails to reproduce the incoherent part of the noise. In contrast, as found in Ref. 15 and further discussed below, the completely dephasing voltage probe model correctly reproduces the incoherent part of both the current and the noise.

To quantify the strength of the oscillations we introduce two separate quantities, $\nu^{\Theta}_{N,\rm MZ}$ and $\nu^{2\Theta}_{N,\rm MZ}$, here simply called visibilities, which in close analogy to the current visibility in Eq. (21) are defined as the ratio of the amplitudes of the noise oscillations and the average noise. They become

$$\nu^{\Theta}_{N,\rm MZ}=\frac{|c_{\Theta}\bar{S}_{\Theta}|}{c_0\bar{S}_0} \tag{27}$$

and

$$\nu^{2\Theta}_{N,\rm MZ}=\frac{|c_{2\Theta}\bar{S}_{2\Theta}|}{c_0\bar{S}_0}. \tag{28}$$

Similarly to the current, both visibilities are products of a term containing the scattering probabilities and a function of the energy scales eV, k_BT, and E_c. We first focus on the scattering probability dependent term by considering the visibility in the limit of a symmetric interferometer, $E_c \gg$ eV, k_BT, where the energy-scale dependent terms are unity. This gives

$$\nu^{\Theta}_{N,\rm MZ}=\frac{2|(\mathcal{T}_A-R_A)(\mathcal{T}_B-R_B)|\sqrt{\mathcal{T}_A\mathcal{T}_BR_AR_B}}{\mathcal{T}_AR_A+\mathcal{T}_BR_B-6\mathcal{T}_AR_A\mathcal{T}_BR_B} \tag{29}$$

and

$$\nu^{2\Theta}_{N,\rm MZ}=\frac{2\mathcal{T}_A\mathcal{T}_BR_AR_B}{\mathcal{T}_AR_A+\mathcal{T}_BR_B-6\mathcal{T}_AR_A\mathcal{T}_BR_B}. \tag{30}$$

The two visibilities are plotted in Fig. 4. Both visibilities are symmetric under the substitutions $\mathcal{T}_A \leftrightarrow R_A$ and $\mathcal{T}_B \leftrightarrow R_B$. The visibility $\nu^{\Theta}_{N,\rm MZ}$ is zero for $\mathcal{T}_A=R_A=1/2$, i.e., for a symmetric setting of any of the QPC's. The visibility increases for increasing QPC asymmetry, reaching a maximum for $0<\mathcal{T}_A<0.5$ and $0<\mathcal{T}_B<0.5$ (unity only in the limit $\mathcal{T}_A, \mathcal{T}_B \ll 1$) and then decreases again toward zero at $\mathcal{T}_A=0$ or $\mathcal{T}_B=0$. Interestingly, the visibility $\nu^{2\Theta}_{N,\rm MZ}$ shows an opposite behavior. It is maximum, equal to unity, at $\mathcal{T}_A=\mathcal{T}_B=1/2$ and then decreases monotonically for increasing QPC asymmetry, reaching zero at $\mathcal{T}_A=0$ or $\mathcal{T}_B=0$. This different dependence on the scattering probabilities makes it possible to investigate the two oscillations independently by modulating the QPC transparencies.

Turning to the energy scale behavior, we consider for simplicity $\nu^{\Theta}_{N,\rm MZ}$ in the limit $\mathcal{T}_A, \mathcal{T}_B \ll 1$ and $\nu^{2\Theta}_{N,\rm MZ}$ in the limit

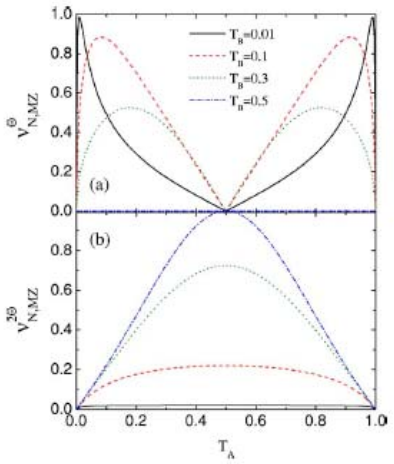

FIG. 4. (Color online) Noise visibility $\nu^{\Theta}_{N,\rm MZ}$ (a) of the h/e and $\nu^{2\Theta}_{N,\rm MZ}$ (b) of the $h/2e$ oscillations in the shot noise of the Mach-Zehnder interferometer versus transmission $\mathcal{T}_A$ of beamsplitter A for $E_c \gg k_BT$, eV for various transmission probabilities $\mathcal{T}_B$ of beamsplitter B.

$\mathcal{T}_A=\mathcal{T}_B=1/2$ where respective scattering probability terms are unity. For a symmetric interferometer, i.e., $E_c \gg$ eV, k_BT, both visibilities are unity. Considering the situation when the temperature is comparable to the asymmetry energy scale E_c but the voltage is small eV $\ll k_BT$, E_c, we get the visibilities $(m=1,2)$

$$\nu^{m\Theta}_{N,\rm MZ}=\frac{m\pi k_BT}{E_c}\,\mathrm{csch}\left(\frac{m\pi k_BT}{E_c}\right)\left[1+\left(\frac{mk_BT}{E_c}\right)^2\right]. \tag{31}$$

The temperature dependence of the visibilities are shown in Fig. 5. Both visibilities decrease monotonically with increasing temperature. For large temperature

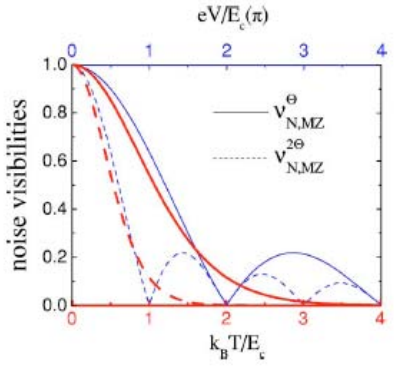

FIG. 5. (Color online) Noise visibilities $\nu^{\Theta}_{N,\rm MZ}$ (for $\mathcal{T}_A, \mathcal{T}_B \ll 1$) of the h/e oscillations (solid curve) and $\nu^{2\Theta}_{N,\rm MZ}$ (for $\mathcal{T}_A=\mathcal{T}_B=1/2$) of the $h/2e$ oscillations (dashed curve) in the shot noise correlation of a Mach-Zehnder interferometer versus k_BT/E_c for eV $\ll k_BT$, E_c (thick, red curve) and versus eV$/E_c$ for $k_BT \ll E_c$, eV (thin, blue curve).

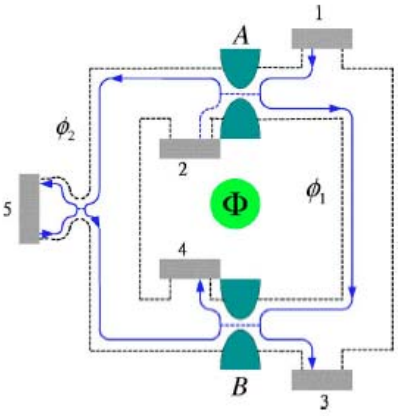

FIG. 6. (Color online) The electrical MZ-interferometer, Fig. 2, with a dephasing voltage probe, 5, attached along one edge.

$k_BT \gg E_c$, the visibilities decay exponentially as $\nu^{\Theta}_{N,\mathrm{MZ}} \propto (k_BT)^3 \exp(-\pi k_BT/E_c)$ and $\nu^{2\Theta}_{N,\mathrm{MZ}} \propto (k_BT)^3 \exp(-2\pi k_BT/E_c)$. The visibility $\nu^{2\Theta}_{N,\mathrm{MZ}}$ is thus considerably more sensitivity to thermal smearing than $\nu^{\Theta}_{N,\mathrm{MZ}}$. In the opposite limit, for a small temperature but a voltage comparable to E_c, i.e., $k_BT \ll E_c$, eV, we instead get the visibilities

$$\nu^{m\Theta}_{N,\mathrm{MZ}} = \frac{2E_c}{m\mathrm{eV}} \left| \sin\left(\frac{m\mathrm{eV}}{2E_c}\right) \right|. \tag{32}$$

The visibilities as a function of voltage are plotted in Fig. 5. Both visibilities show an oscillating behavior, decaying as a power law $\propto 1/\mathrm{eV}$ with increasing voltage. The period of oscillations, in eV, is $2\pi E_c$ for $\nu^{\Theta}_{N,\mathrm{MZ}}$ but πE_c for $\nu^{2\Theta}_{N,\mathrm{MZ}}$, half the value for $\nu^{\Theta}_{N,\mathrm{MZ}}$. The different voltage dependence gives an additional possibility to investigate the two visibilities independently.

In the experiment of Ji *et al.*[9] the noise was measured in the high voltage regime, with the interference terms in both the current and noise completely suppressed. The dependence of the incoherent noise on the transparencies $\mathcal{T}_A$ and $\mathcal{T}_B$ was investigated ($\mathcal{T}_A$ was kept at 1/2 and $\mathcal{T}_B$ was varied). A good agreement was found with the first, incoherent term in Eq. (24). Taken the open questions on the effect of decoherence on the average current, a detailed experimental investigation on the phase dependent, interference part of the noise would be of great interest.

Effect of dephasing

Next we consider the effect of dephasing on the current and noise. As discussed above, dephasing is introduced by connecting one of the two arms of the interferometer to a fictitious, dephasing voltage probe. The interferometer with the probe, denoted terminal 5, is shown in Fig. 6. The dephasing probe is connected to the edge via a contact described by a scattering matrix

$$\begin{pmatrix} \sqrt{1-\varepsilon} & i\sqrt{\varepsilon} \\ i\sqrt{\varepsilon} & \sqrt{1-\varepsilon} \end{pmatrix}, \tag{33}$$

where the dephasing parameter ε varies between 0 (no dephasing, fully coherent transport) and 1 (complete dephasing, fully incoherent transport). The presence of the dephasing probe modifies the amplitudes for scattering between the terminal 1, 2, 3, and 4. As an example, the scattering amplitude s_{41}, given in Eq. (16) in the absence of dephasing, now becomes

$$s_{41}(\varepsilon) = i\sqrt{\mathcal{T}_B R_A} e^{i(\phi_1+\psi_1)} + i\sqrt{1-\varepsilon}\sqrt{\mathcal{T}_A R_B} e^{i(\phi_2-\psi_2)}. \tag{34}$$

In addition, amplitudes for scattering into and out from the probe terminal 5 have to be considered. The current is obtained from Eqs. (4), (5), and (12). For the current in terminal 4, we find

$$I_4^{\mathrm{dp}} = \frac{e}{h}\Bigg[(\mathcal{T}_A R_B + \mathcal{T}_B R_A)\mathrm{eV} \times \sqrt{1-\varepsilon}\sqrt{\mathcal{T}_A \mathcal{T}_B R_A R_B} 4\pi k_BT \,\mathrm{csch}\left(\frac{k_BT\pi}{E_c}\right) \times \sin\left(\frac{\mathrm{eV}}{2E_c}\right)\cos\left(\frac{\mathrm{eV}}{2E_c}+\Theta\right)\Bigg]. \tag{35}$$

Comparison with the result in the absence of dephasing in Eq. (19) shows that the effect of the dephasing is to suppress the phase-dependent oscillations by multiplying the phase-dependent interference term with a factor $\sqrt{1-\varepsilon}$. For complete dephasing $\varepsilon=1$, the phase dependent term is completely suppressed. The effect of dephasing can thus be simply incorporated in the visibility as

$$\nu^{\mathrm{dp}}_{I,\mathrm{MZ}} = \sqrt{1-\varepsilon}\,\nu_{I,\mathrm{MZ}}, \tag{36}$$

where $\nu_{I,\mathrm{MZ}}$ is the visibility of the current oscillations in the absence of dephasing, given by Eq. (21). As is clear from the discussion above, to account for the experimental observations in Ref. 9, one would have to consider a voltage dependent dephasing parameter ε.

Turning to the noise, we obtain the cross correlator between currents in lead 3 and 4 in the presence of dephasing from Eqs. (8) and (14), giving

$$S_{34}^{\mathrm{dp}} = -\frac{2e^2}{h}\Bigg\{ c_0\bar{S}_0 + c_\Theta \bar{S}_\Theta \sqrt{1-\varepsilon}\cos\left(\frac{\mathrm{eV}}{2E_c}+\Theta\right) + c_{2\Theta}\bar{S}_{2\Theta}(1-\varepsilon)\cos\left[2\left(\frac{\mathrm{eV}}{2E_c}+\Theta\right)\right]\Bigg\}. \tag{37}$$

Here the terms c_0, c_Θ $c_{2\Theta}$, $\bar{S}_0$, $\bar{S}_\Theta$, and $\bar{S}_{2\Theta}$ are defined above in Eqs. (23) and (25). Similarly to the current, the effect of the dephasing is only to suppress the amplitude of the phase-dependent oscillations. That is what one would naively expect to be the consequence of pure dephasing. The two phase-dependent terms are however affected differently, the $\cos\Theta$ term is suppressed by a factor $\sqrt{1-\varepsilon}$ while the $\cos 2\Theta$ term is suppressed by $(1-\varepsilon)$. The $\cos 2\Theta$ oscillations are thus more strongly suppressed. The visibilities of the two

oscillations in the presence of dephasing can simply be written

$$\nu_{N,\mathrm{MZ}}^{\Theta,\mathrm{dp}} = \sqrt{1-\varepsilon}\,\nu_{N,\mathrm{MZ}}^{\Theta} \tag{38}$$

and

$$\nu_{N,\mathrm{MZ}}^{2\Theta,\mathrm{dp}} = (1-\varepsilon)\nu_{N,\mathrm{MZ}}^{2\Theta}, \tag{39}$$

where $\nu_{N,\mathrm{MZ}}^{\Theta}$ and $\nu_{N,\mathrm{MZ}}^{2\Theta}$ are the visibilities for the noise oscillations in the absence of dephasing, given by Eqs. (27) and (28), respectively.

Importantly, both oscillating terms are fully suppressed for complete dephasing, $\varepsilon=1$. Complete dephasing within the voltage probe model thus gives a noise expression that only consists of the phase independent, incoherent term in Eq. (22). We note already here that the same result is found below for the HBT-interferometer. Since quantum interference by definition is excluded from the model, i.e., all scattering phases are neglected, the completely dephasing voltage probe thus constitutes a classical model that correctly reproduces the incoherent part of the noise. As pointed out above, a more detailed discussion of the physics of the voltage probe and a comparison with Refs. 14, 15, and 59 is deferred to a later work.

It is interesting to note that the effect of dephasing introduced with the voltage probe, both for the current and noise, is for arbitrary coupling to the voltage probe identical to a phase averaging. The result in Eqs. (38) and (39) can be obtained by averaging the fully coherent expressions in Eqs. (27) and (28) with respect to a Lorentzian distribution $\rho(\Theta)$ of slow fluctuations of the phase Θ around the average value Θ_0, as

$$\int d\Theta\rho(\Theta)\cos(n\Theta) = (1-\varepsilon)^{n/2}\cos(n\Theta_0) \tag{40}$$

with the Lorentzian distribution

$$\rho(\Theta) = \frac{a/\pi}{(\Theta-\Theta_0)^2+a^2}, \quad a = -(1/2)\ln(1-\varepsilon). \tag{41}$$

We note that, as pointed out in Ref. 15, a Gaussian distribution of the phase fluctuations gives a different result, not consistent with the dephasing voltage probe approach for arbitrary coupling to the voltage probe.

We emphasize that the results above are independent on to which edge the probe is connected. Moreover, we also point out that the effect of the voltage probes, for arbitrary ε, is multiplicative, i.e., attaching n voltage probes at arbitrary places along the arms can be described by renormalizing $1-\varepsilon\rightarrow(1-\varepsilon)^n$. Writing $(1-\varepsilon)^n=\exp(n\ln[1-\varepsilon])=\exp(-L/L_\phi)$, with $L_\phi=-d/\ln[1-\epsilon]$ and $L=nd$ with d the distance between two probes, we can quite naturally incorporate the effect of a uniform distribution of probes into a dephasing length L_ϕ. The suppression of the visibilities of the h/e and $h/2e$ oscillations due to dephasing in Eqs. (38) and (39) are then modified as $(1-\varepsilon)^{1/2}\rightarrow\exp(-L/2L_\phi)$ and $(1-\varepsilon)\rightarrow\exp(-L/L_\phi)$.

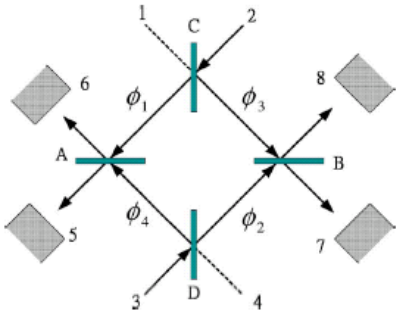

FIG. 7. (Color online) Two-source, four-detector optical Hanbury Brown Twiss geometry proposed in Ref. 27. Two beams of light incident from 2 and 3 are split in partial beams at the semitransparent beamsplitters C and D. The partial beams acquire geometrical phases $\phi_1-\phi_4$ and are rejoined in the beamsplitters A and B. The light intensity is measured in detectors 5–8.

IV. HANBURY BROWN TWISS INTERFEROMETERS

The HBT-interferometer is less well known than the MZ-interferometer and deserves some additional comments.[65] The HBT-interferometer was invented as a tool to measure the angular diameter of stars. The first measurement[18] was carried out on a radio star in 1954. Compared to existing schemes based on Michelson interferometers, the HBT-interferometer proved to be less sensitive to atmospheric scintillations, which allowed for a more accurate determination of the angular diameter. After having demonstrated a table-top version of the interferometer in the visual range,[19] the angular diameter of the visual star Sirius was determined.[20]

The experimental results, both the two-particle interference and the positive intensity cross correlations, were successfully explained within a semiclassical framework. Soon after the experiments, it was however shown by Purcell[66] that the positive cross correlations could be explained in terms of bunching of individual photons, emerging from the star, a thermal source of light. This bunching was also demonstrated explicitly in subsequent photo counting experiments.[67,68] The HBT experiment thus laid the foundations for quantum statistical methods in quantum optics.[69] The HBT approach has also been of importance in experimental particle physics.[70] It is interesting to note that positive intensity cross correlations between beams of light emerging from a thermal source, according to some contemporary[71,72] "*would call for a major revision of some fundamental concepts in quantum mechanics.*" Purcell,[66] however, providing an elegant explanation of the bunching phenomena, pointed out that "*the Hanbury Brown Twiss effect, far from requiring a revision of quantum mechanics, is an instructive illustration of its elementary principles.*"

An optical table-top version[73,74] of the HBT-interferometer is shown in Fig. 7. A beam of light is emitted from each one of the sources 2 and 3, completely uncorrelated with each other. The beams are split in two partial beams at the semitransparent beam splitters C and D respectively. The partial beams acquire phases ϕ_1 to ϕ_4 before

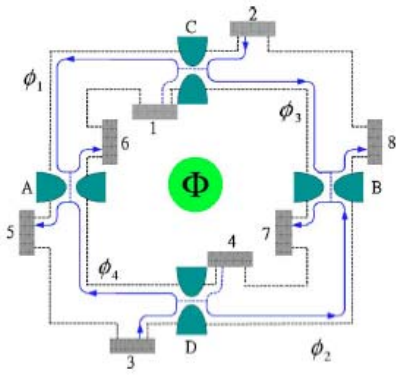

FIG. 8. (Color online) Two-source, four-detector electrical Hanbury Brown Twiss geometry implemented in a conductor in the quantum Hall regime. The electronic reservoirs 2 and 3 biased at eV and reservoirs 1 and 4 to 8 are kept at ground. The edge states (solid lines) have a direction of transport indicated by arrows. The QPC's A and B play the role of the beamsplitters in Fig. 7. Geometrical phases ϕ_1 to ϕ_4 and the AB-flux Φ are shown.

scattering at the second pair of beam splitters A and B. The resulting beams are collected in detectors at ports 5 to 8.

Importantly, there is no interference pattern in the intensities at the detectors 5 to 8, instead the interference occurs only in the cross correlations between intensities at 5, 6 and 7, 8. The intensity cross correlations are sensitive to the two-particle amplitudes: the interference is thus between two different two-particle scattering events, e.g. (i) one particle from 2 scatters to 5 and one particle from 3 scatters to 8, with an amplitude $A_1 \exp(i[\phi_1+\phi_2])$ and (ii) one particle from 2 scatters to 8 and one particle from 3 scatters to 5, with an amplitude $A_2 \exp(i[\phi_3+\phi_4])$. The amplitude to detect one particle in 5 and one in 8 is then the sum of the two two-particle amplitudes. This is the case since both scattering processes have the same initial and final states and cannot be distinguished. The (reducible) cross correlation between intensities in 5 and 8 is directly related to the corresponding two-particle probability $|A_1 \exp(i[\phi_1+\phi_2]) + A_2 \exp(i[\phi_3+\phi_4])|^2 = |A_1|^2 + |A_2|^2 + 2\,\mathrm{Re}\{A_1 A_2^* \exp(i[\phi_1+\phi_2 - \phi_3-\phi_4])\}$. The interference term $2\,\mathrm{Re}\{A_1 A_2^* \exp(i[\phi_1+\phi_2 - \phi_3-\phi_4])\}$ contains the four geometrical phases ϕ_1 to ϕ_4. The HBT-interferometer is thus, in contrast to the MZ-interferometer, a two-particle interferometer.

The electrical analog of the HBT-interferometer, presented in Ref. 27, is shown in Fig. 8. It consists of a (rectangular) conductor with a hole in the middle, a Corbino geometry. Similar to the MZ-interferometer, the electrons propagate along single edge states. Scattering between the edge states take place only at the beamsplitters A–D. The beamsplitters are described by scattering matrices given by Eq. (15). We first consider the fully coherent case. In contrast to the MZ-interferometer, the scattering amplitudes contain the phases ϕ_i and ψ_i only via multiplicative phase factors. As an example, the amplitude to scatter from terminal 2 to terminal 5 is given by

$$s_{52} = \sqrt{\mathcal{T}_A \mathcal{T}_C} e^{i(\phi_1-\psi_1)}. \tag{42}$$

As a consequence, the average currents which depend only on the modulus squared of the scattering amplitudes [see Eqs. (4) and (6)] do not contain any scattering phases. We get the currents at terminals 5–8 as

$$\begin{aligned} I_5 &= (e^2/h)V \quad (\mathcal{T}_A\mathcal{T}_C + R_A R_D), \\ I_6 &= (e^2/h)V \quad (\mathcal{T}_A R_D + R_A \mathcal{T}_C), \\ I_7 &= (e^2/h)V \quad (\mathcal{T}_B R_C + R_B \mathcal{T}_D), \\ I_8 &= (e^2/h)V \quad (\mathcal{T}_B\mathcal{T}_D + R_B R_C). \end{aligned} \tag{43}$$

Turning to the current noise, the correlation between currents in terminals 5,6 and 7,8 is given by Eq. (9). We find for the spectral density for the correlators between terminal 5 and 8

$$S_{58}(E) = \frac{-2e^2}{h}[f(E) - f_0(E)]^2 \{c_{0,58} + c_\Theta \cos(E/E_c + \Theta)\} \tag{44}$$

with the coefficients

$$\begin{aligned} c_{0,58} &= \mathcal{T}_A R_B \mathcal{T}_C R_C + \mathcal{T}_B R_A \mathcal{T}_D R_D; \\ \bar{c}_\Theta &= 2 \prod_{j=A,B,C,D} \sqrt{\mathcal{T}_j R_j}, \end{aligned} \tag{45}$$

and for the correlator between terminal 5 and 7

$$S_{57}(E) = \frac{-2e^2}{h}[f(E) - f_0(E)]^2 \{c_{0,57} + \bar{c}_\Theta \cos(E/E_c + \Theta)\} \tag{46}$$

with the coefficient

$$c_{0,57} = \mathcal{T}_A \mathcal{T}_B \mathcal{T}_C R_C + R_A R_B \mathcal{T}_D R_D. \tag{47}$$

Performing the energy integrals in Eq. (9), we obtain the corresponding current cross correlators

$$S_{58} = \frac{-2e^2}{h}\left[c_{0,58}\bar{S}_0 + \bar{c}_\Theta \bar{S}_\Theta \cos\left(\frac{\mathrm{eV}}{2E_c} + \Theta\right)\right] \tag{48}$$

and

$$S_{57} = \frac{-2e^2}{h}\left[c_{0,57}\bar{S}_0 + \bar{c}_\Theta \bar{S}_\Theta \cos\left(\frac{\mathrm{eV}}{2E_c} + \Theta\right)\right]. \tag{49}$$

Here $\bar{S}_0$ and $\bar{S}_\Theta$ are given by Eqs. (25) and (26). The other two correlators S_{67} and S_{68} are given by the substitutions $S_{67}=S_{58}$ $(\mathcal{T}_C \leftrightarrow \mathcal{T}_D)$ and $S_{68}=S_{57}$ $(\mathcal{T}_C \leftrightarrow \mathcal{T}_D)$. Here, as for the MZ-interferometer we have $\Theta = \Delta\phi(E_F) + 2\pi\Phi/\Phi_0$ with $\Delta\phi = \phi_1+\phi_2-\phi_3-\phi_4$ and $\Sigma_{i=1}^4 \psi_i = 2\pi\Phi/\Phi_0$.

Several observation can be made from the results above, put in comparison with the result for the noise correlations for the MZ-interferometer in Eq. (24). Just as for the MZ-interferometer, the noise consists of an incoherent, phase independent part, and a coherent, interference part. The phase dependent part of the noise in Eqs. (48) and (49) however

contains only one term. The amplitude of the oscillating term is a product of a scattering probability term and an energy-scale dependent function, just as for the MZ-interferometer. This phase dependent term has the same dependence on the phase Θ, the same voltage dependent phase shift as well as the same energy-scale dependence as the second term in Eq. (24). This is the case since they both arise from processes which enclose the AB-flux once. Despite the fact that in the HBT interferometer the AB-effect results from two-particle processes, the periodicity is determined by the single electron flux quantum h/e. The dependence on the scattering probabilities is however different, a consequence of the MZ and HBT interferometer geometries being different. Importantly, there is no term in the noise in Eqs. (48) and (49) that corresponds to the last term in Eq. (24), describing processes which enclose the AB-flux twice. We note that the elementary scattering processes in the HBT-interferometer, in contrast to the MZ-interferometer, are two-particle processes. An important consequence of this is that the incoherent, phase independent noise term in Eqs. (48) and (49) can directly be reproduced by a model with filled streams of classical particles incident from reservoirs 2 and 3.

Since there is only one phase-dependent term, the visibility of the phase-dependent oscillations can again be directly defined, giving for $\alpha=5,6$ and $\beta=7,8$

$$\nu_{N,\mathrm{HBT}}^{\Theta,\alpha\beta}=\frac{|\bar{c}_{\Theta}\bar{S}_{\Theta}|}{c_{0,\alpha\beta}\bar{S}_0}. \tag{50}$$

Since the energy-scale dependence of the visibilities is identical to $\nu_{N,\mathrm{MZ}}^{\Theta}$ for the MZ-interferometer in Eq. (27), shown in Fig. 5, we focus here only on the scattering probability terms. We thus consider the limit of a symmetric interferometer, $E_c \gg k_B T$, eV for which the energy-scale dependent part is unity. Several symmetries exists, e.g., all visibilities $\nu_{N,\mathrm{HBT}}^{\Theta,\alpha\beta}$ are unchanged by the substitutions $R_C \leftrightarrow T_C$ and $R_D \leftrightarrow T_D$. The visibility $\nu_{N,\mathrm{HBT}}^{\Theta,58}$ is unity for scattering probabilities obeying $T_A R_B R_C T_C = T_B R_A R_D T_D$ and similar relations hold for the other visibilities. All visibilities go to zero for any of the transmission probabilities approaching either zero or unity. Focusing on the case with $T_C=T_D$ (or equivalently $T_C=R_D$), the visibilities are given by

$$\nu_{N,\mathrm{HBT}}^{\Theta,58}=\nu_{N,\mathrm{HBT}}^{\Theta,67}=\frac{2\sqrt{\mathcal{T}_A R_A \mathcal{T}_B R_B}}{\mathcal{T}_A R_B+\mathcal{T}_B R_A} \tag{51}$$

and

$$\nu_{N,\mathrm{HBT}}^{\Theta,57}=\nu_{N,\mathrm{HBT}}^{\Theta,68}=\frac{2\sqrt{\mathcal{T}_A R_A \mathcal{T}_B R_B}}{\mathcal{T}_A \mathcal{T}_B+R_A R_B}. \tag{52}$$

The two different visibilities are plotted in Fig. 9 as a function of $\mathcal{T}_A$ for different $\mathcal{T}_B$. The visibility $\nu_{N,\mathrm{HBT}}^{\Theta,58}$ has a maximum equal to unity for $\mathcal{T}_A=\mathcal{T}_B$, while $\nu_{N,\mathrm{HBT}}^{\Theta,57}$ instead has a maximum equal to unity for $\mathcal{T}_A=R_B$.

The effect of dephasing

Just as in the MZ-interferometer, the dephasing in the HBT-interferometer is introduced by connecting a fictitious voltage probe to an edge between any of the two point contacts. The HBT-interferometer with the probe, denoted 9, is shown in Fig. 10. Here the probe is connected to the edge between contact C and A, we emphasize that the results discussed below do not depend on to which edge-state the probe is connected.

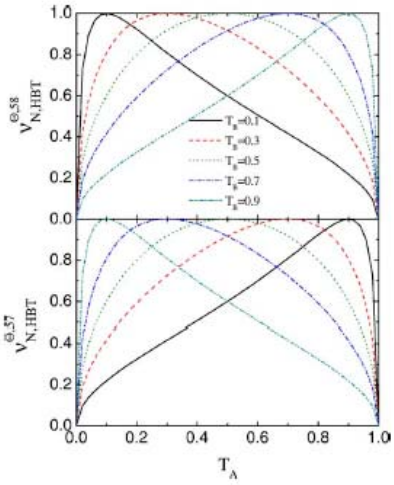

FIG. 9. (Color online) Noise visibilities $\nu_{N,\mathrm{HBT}}^{\Theta,58}$ and $\nu_{N,\mathrm{HBT}}^{\Theta,57}$ of shot noise correlations in the HBT geometry versus transmission probability $\mathcal{T}_A$ for various values of $\mathcal{T}_B$. A symmetric geometry, $E_c \gg kT$, eV, and identical QPC's C and D are considered.

The presence of the probe modifies the amplitudes for scattering from terminals 2, 3 to terminals 5 to 8. As an example, the scattering amplitude in Eq. (42) is modified

$$s_{52}=\sqrt{1-\varepsilon}\sqrt{\mathcal{T}_A \mathcal{T}_C}e^{i(\phi_1-\psi_1)}. \tag{53}$$

In addition, we also have to consider amplitudes for scattering into and out from the probe terminal 9. The average currents in the presence of dephasing, given from Eqs. (4)–(6) and (12), turn out to be given by the same equations as in the absence of dephasing, i.e., Eq. (43). This is what

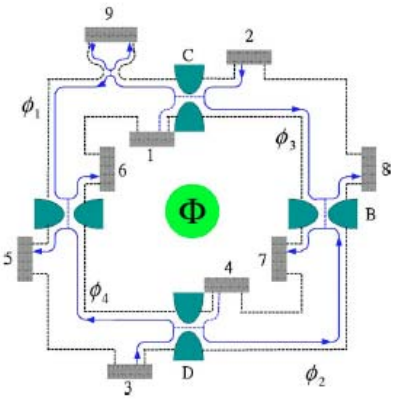

FIG. 10. (Color online) The electrical HBT-interferometer, Fig. 8, with a dephasing voltage probe, 9, attached along one edge.

one expects, i.e., that dephasing affects only the phase-dependent parts of the observables.

Turning to the current correlators, given from Eqs. (8), (9), and (14), we find for the correlators between terminal 5 and 8

$$S_{58}^{\mathrm{dp}} = \frac{-2e^2}{h}\left[c_{0,58}\bar{S}_0 + \bar{c}_{\Theta}\bar{S}_{\Theta}\sqrt{1-\varepsilon}\cos\left(\frac{\mathrm{eV}}{2E_c}+\Theta\right)\right] \tag{54}$$

and for the correlators between terminals 5 and 7

$$S_{57}^{\mathrm{dp}} = \frac{-2e^2}{h}\left[c_{0,57}\bar{S}_0 + \bar{c}_{\Theta}\bar{S}_{\Theta}\sqrt{1-\varepsilon}\cos\left(\frac{\mathrm{eV}}{2E_c}+\Theta\right)\right]. \tag{55}$$

The two remaining correlators are again given by the substitutions $S_{67}=S_{58}$ $(\mathcal{T}_C \leftrightarrow \mathcal{T}_D)$ and $S_{68}=S_{57}$ $(\mathcal{T}_C \leftrightarrow \mathcal{T}_D)$. We see from Eqs. (54) and (55) that just as for the MZ-interferometer, the only effect of dephasing is to suppress the phase-dependent term. The suppression factor is $\sqrt{1-\varepsilon}$, just the same as for the $\cos\Theta$ term in the noise for the MZ-interferometer in Eq. (24). We can thus directly write the visibilities in the presence of dephasing as

$$\nu_{N,\mathrm{HBT}}^{\Theta,\alpha\beta,\mathrm{dp}} = \sqrt{1-\varepsilon}\,\nu_{N,\mathrm{HBT}}^{\Theta,\alpha\beta}. \tag{56}$$

This leads to the conclusion that the voltage probe for the HBT-interferometer, just as for the MZ-interferometer, just has the same effect as dephasing due to slow fluctuations of the phase Θ, with the distribution of the phase fluctuations obeying the relation in Eq. (40). Moreover, the voltage probes have the same multiplicative property as for the MZ-interferometer, allowing one to describe the effect of a continuum of probes along the edges (of total length $L=L_1+L_2+L_3+L_4$) with a dephasing length L_ϕ. The suppression of the visibilities of the h/e oscillations due to dephasing are then modified as $(1-\varepsilon)^{1/2} \to \exp(-L/2L_\phi)$, just as for the h/e oscillations of the MZ-interferometer.

V. CONCLUSIONS

The MZ-interferometer is an amplitude interferometer: it exhibits a visibility in the average current with period h/e and exhibits a visibility in the shot noise with periods of both h/e and $h/2e$. In contrast, the HBT interferometer is an intensity interferometer, it exhibits no AB-effect in the current and exhibits only an h/e-effect in the shot noise correlations. Interestingly, our investigation shows that the shot noise visibility of the HBT interferometer as a function of temperature, voltage and dephasing rate, is qualitatively similar to that of the h/e-component of the shot noise of the MZ-interferometer. This is contrary to the naive expectation that the visibility of the two particle processes which lead to the HBT effect should be similar to the visibility of the two particle processes in the MZ-interferometer, that is the $h/2e$ component of the shot noise. Instead it is the number of times the AB-flux is enclosed which determines the behavior of the visibility.

In this paper we have investigated and compared in detail the voltage, temperature and asymmetry dependence for the current and noise visibilities in the MZ and HBT-interferometers. The experimental realization of the HBT-interferometer is of large importance since it allows for an unambiguous demonstration of two-particle interference effects with electrons, to date not demonstrated. Moreover, a successful realization of the HBT-interferometer would also enable a first demonstration of orbital entanglement in electrical conductors, a fundamentally important result. The results presented in this work should prove useful for the experimental work aiming to detect the HBT effect in electrical conductors.

Note added in proof. Recently, I. Neder *et al.*[75] presented new measurements on the conductance in an electronic Mach-Zehnder interferometer, indicating the importance of screening effects in understanding the finite voltage properties of the interferometer.

ACKNOWLEDGMENTS

We thank M. Heiblum, I. Neder, H. Förster, and E. Sukhorukov for stimulating discussions. This work was supported by the Graduate Students Study Abroad Program and NSC93-2112-M-009-036 of Taiwan National Science Council, the Swedish Research Council and the Swiss National Science Foundation and the network for Materials with Novel Electronic Properties.

[1] M. Büttiker, Phys. Rev. B **46**, 12485 (1992).
[2] Ya. Blanter and M. Büttiker, Phys. Rep. **336**, 1 (2000).
[3] M. Born and E. Wolf, *Principles of Optics*, 7th ed. (Cambridge University Press, Cambridge, 1999).
[4] L. Mandel, Rev. Mod. Phys. **71**, S274 (1999).
[5] See, e.g., S. Pedersen, A. E. Hansen, A. Kristensen, C. B. Sorensen, and P. E. Lindelof, Phys. Rev. B **61**, 5457 (2000), and references therein.
[6] E. Buks, R. Schuster, M. Heilblum, D. Mahalu, and V. Umansky, Nature (London) **391**, 871 (1999).
[7] A. E. Hansen, A. Kristensen, S. Pedersen, C. B. Sorensen, and P. E. Lindelof, Phys. Rev. B **64**, 045327 (2001).
[8] K. Kobayashi, H. Aikawa, S. Katsumoto, and Y. Iye, J. Phys. Soc. Jpn. **71**, 2094 (2002).
[9] Y. Ji, Y. Chung, D. Sprinzak, M. Heilblum, D. Mahalu, and H. Shtrikman, Nature (London) **422**, 415 (2003).
[10] G. Seelig and M. Büttiker, Phys. Rev. B **64**, 245313 (2001).
[11] G. Seelig, S. Pilgram, A. N. Jordan, and M. Büttiker, Phys. Rev. B **68**, 161310(R) (2003).
[12] K. Le Hur, Phys. Rev. B **65**, 233314 (2002).
[13] K. Le Hur, Phys. Rev. Lett. **95**, 076801 (2005).
[14] F. Marquardt and C. Bruder, Phys. Rev. Lett. **92**, 056805 (2004).
[15] F. Marquardt and C. Bruder, Phys. Rev. B **70**, 125305 (2004).
[16] F. Marquardt, cond-mat/0410333 (unpublished).

[17] H. Förster, S. Pilgram, and M. Büttiker, Phys. Rev. B **72**, 075301 (2005).
[18] R. Hanbury Brown and R. Q. Twiss, Philos. Mag. **45**, 663 (1954).
[19] R. Hanbury Brown and R. Q. Twiss, Nature (London) **177**, 27 (1956).
[20] R. Hanbury Brown and R. Q. Twiss, Nature (London) **178**, 1046 (1956).
[21] M. Henny, S. Oberholzer, C. Strunk, T. Heinzel, K. Ensslin, M. Holland, and C. Schönenberger, Science **284**, 296 (1999).
[22] W. D. Oliver, J. Kim, R. C. Liu, and Y. Yamamoto, Science **284**, 299 (1999).
[23] H. Kiesel, A. Renz, and F. Hasselbach, Nature (London) **418**, 392 (2002).
[24] M. Büttiker, Physica B **175**, 199 (1991).
[25] M. Büttiker, Phys. Rev. Lett. **68**, 843 (1992).
[26] D. Loss and E. V. Sukhorukov, Phys. Rev. Lett. **84**, 1035 (1992).
[27] P. Samuelsson, E. V. Sukhorukov, and M. Büttiker, Phys. Rev. Lett. **92**, 026805 (2004).
[28] K. v. Klitzing, G. Dorda, and M. Pepper, Phys. Rev. Lett. **45**, 494 (1980).
[29] M. Büttiker, Phys. Rev. B **38**, 9375 (1988).
[30] B. I. Halperin, Phys. Rev. B **25**, 2185 (1982).
[31] B. J. van Wees, H. van Houten, C. W. J. Beenakker, J. G. Williamson, L. P. Kouwenhoven, D. van der Marel, and C. T. Foxon, Phys. Rev. Lett. **60**, 848 (1988).
[32] D. A. Wharam, T. J. Thornton, R. Newbury, M. Pepper, H. Ahmed, J. E. F. Frost, D. G. Hasko, D. C. Peacock, D. A. Ritchie, and G. A. C. Jones, J. Phys. C **21**, L861 (1988).
[33] R. C. Liu, B. Odom, Y. Yamamoto, and S. Tarucha, Nature (London) **391**, 263 (1998).
[34] S. Oberholzer, M. Henny, C. Strunk, C. Schonenberger, T. Heinzel, K. Ensslin, and M. Holland, Physica E (Amsterdam) **6**, 314 (2000).
[35] M. Büttiker, P. Samuelsson, and E. V. Sukhorukov, Physica E (Amsterdam) **20**, 33 (2003).
[36] P. Samuelsson, E. V. Sukhorukov, and M. Büttiker, Phys. Rev. Lett. **91**, 157002 (2003).
[37] C. W. J. Beenakker, C. Emary, M. Kindermann, and J. L. van Velsen, Phys. Rev. Lett. **91**, 147901 (2003).
[38] C. W. J. Beenakker and M. Kindermann, Phys. Rev. Lett. **92**, 056801 (2004).
[39] P. Samuelsson and M. Büttiker, Phys. Rev. B **71**, 245317 (2005).
[40] See also related work by C. W. J. Beenakker, M. Titov, and B. Trauzettel, Phys. Rev. Lett. **94**, 186804 (2005); A. V. Lebedev, G. B. Lesovik, and G. Blatter, cond-mat/0504583 (unpublished).
[41] T. M. Stace, C. H. W. Barnes, and G. J. Milburn, Phys. Rev. Lett. **93**, 126804 (2004).
[42] L. Saminadayar, D. C. Glattli, Y. Jin, and B. Etienne, Phys. Rev. Lett. **79**, 2526 (1997).
[43] R. de-Picciotto, M. Reznikov, M. Heiblum, V. Umansky, G. Bunin, and D. Mahalu, Nature (London) **389**, 162 (1997).
[44] I. Safi, P. Devillard, and T. Martin, Phys. Rev. Lett. **86**, 4628 (2001).
[45] S. Vishveshwara, Phys. Rev. Lett. **91**, 196803 (2003).
[46] S. A. Kivelson and V. L. Pokrovsky, Phys. Rev. B **40**, 1373 (1989).
[47] C. deC. Chamon, D. E. Freed, S. A. Kivelson, S. L. Sondhi, and X. G. Wen, Phys. Rev. B **55**, 2331 (1997).
[48] M. R. Geller and D. Loss, Phys. Rev. B **56**, 9692 (1997).
[49] T. Jonckheere, P. Devillard, A. Crepieux, and Th. Martin, cond-mat/0503617 (unpublished); K. T. Law, D. E. Feldman, and Yuval Gefen, cond-mat/0506302 (unpublished).
[50] T. Christen and M. Büttiker, Europhys. Lett. **35**, 523 (1996); M. Büttiker, J. Phys.: Condens. Matter **5**, 9361 (1993).
[51] M. Büttiker, Phys. Rev. Lett. **57**, 1761 (1986).
[52] M. Büttiker, Phys. Rev. Lett. **65**, 2901 (1990).
[53] M. Büttiker, Phys. Rev. B **33**, 3020 (1986).
[54] M. Büttiker, IBM J. Res. Dev. **32**, 63 (1988).
[55] C. W. J. Beenakker and M. Büttiker, Phys. Rev. B **46**, R1889 (1992).
[56] M. J. M. de Jong and C. W. J. Beenakker, Physica A **230**, 219 (1996).
[57] S. A. van Langen and M. Büttiker, Phys. Rev. B **56**, R1680 (1997).
[58] C. Texier and M. Büttiker, Phys. Rev. B **62**, 7454 (2000); **46**, 1889 (1992).
[59] A. A. Clerk and A. D. Stone, Phys. Rev. B **69**, 245303 (2004).
[60] C. W. J. Beenakker and B. Michaelis, cond-mat/0503347 (unpublished).
[61] D. B. Chklovskii, B. I. Shklovskii, and L. I. Glazman, Phys. Rev. B **46**, 4026 (1992); N. R. Cooper and J. T. Chalker, *ibid.* **48**, 4530 (1993).
[62] H. A. Fertig, Phys. Rev. B **38**, 996 (1988).
[63] See, e.g., the discussion in N. C. van der Vaart, M. P. de Ruyter van Steveninck, L. P. Kouwenhoven, A. T. Johnson, Y. V. Nazarov, C. J. P. M. Harmans, and C. T. Foxon, Phys. Rev. Lett. **73**, 320 (1994), and references therein.
[64] D. Sanchez and M. Büttiker, Phys. Rev. Lett. **93**, 106802 (2004); T. Christen and M. Büttiker, Phys. Rev. B **53**, 2064 (1996).
[65] For an interesting historical account, see R. Hanbury Brown, *The Intensity Interferometer* (Taylor and Francis, London, 1974).
[66] E. M. Purcell, Nature (London) **178**, 1449 (1956).
[67] R. Q. Twiss, A. G. Little, and R. Hanbury Brown, Nature (London) **180**, 324 (1957).
[68] G. A. Rebka and R. V. Pound, Nature (London) **180**, 1035 (1957).
[69] See, e.g., R. Loudon, Rep. Prog. Phys. **43**, 58 (1980).
[70] G. Baym, Acta Phys. Pol. B **29**, 1839 (1998).
[71] E. Brannen and H. I. S. Ferguson, Nature (London) **178**, 481 (1956).
[72] R. Hanbury Brown and R. Q. Twiss, Nature (London) **178**, 1447 (1956).
[73] B. Yurke and D. Stoler, Phys. Rev. Lett. **68**, 1251 (1992).
[74] B. Yurke and D. Stoler, Phys. Rev. A **46**, 2229 (1992).
[75] I. Neder, M. Heiblum, Y. Levinson, D. Mahalu, and V. Umansky, cond-mat/0508024 (unpublished).

Appendix C:

PHYSICAL REVIEW B 73, 085304 (2006)

dc spin current generation in a Rashba-type quantum channel

L. Y. Wang,[1] C. S. Tang,[2] and C. S. Chu[1]
[1]*Department of Electrophysics, National Chiao Tung University, Hsinchu 30010, Taiwan*
[2]*Physics Division, National Center for Theoretical Sciences, P.O. Box 2-131, Hsinchu 30013, Taiwan*
(Received 15 August 2005; revised manuscript received 2 November 2005; published 2 February 2006)

We propose and demonstrate theoretically that resonant inelastic scattering (RIS) can play an important role in dc spin current generation. The RIS makes it possible to generate dc spin current via a simple gate configuration: a single finger gate that locates atop and orients transversely to a quantum channel in the presence of Rashba spin-orbit interaction. The ac-biased finger gate gives rise to a time variation in the Rashba coupling parameter, which causes spin-resolved RIS and, subsequently, contributes to the dc spin current. The spin current depends on both the static and the dynamic parts in the Rashba coupling parameter, α_0 and α_1, respectively, and is proportional to $\alpha_0\alpha_1^2$. The proposed gate configuration has the added advantage that no dc charge current is generated. Our study also shows that the spin current generation can be enhanced significantly in a double finger-gate configuration.

DOI: 10.1103/PhysRevB.73.085304 PACS number(s): 73.23.−b, 72.25.−b, 72.30.+q

I. INTRODUCTION

Spintronics is important in both application and fundamental arenas.[1,2] A recent key issue of great interest is the generation of dc spin current (SC) without charge current. Various dc SC generation schemes have been proposed, involving static magnetic field,[3–5] ferromagnetic material,[6] or ac magnetic field.[7] More recently, Rashba-type spin-orbit interaction (SOI) in two dimension electron gas (2DEG)[8–10] has inspired attractive proposals for nonmagnetic dc SC generation.[11–13] Of these recent proposals, including a time-modulated quantum dot with a static spin-orbit coupling,[11] and time modulations of a barrier and the spin-orbit coupling parameter in two spatially separated regions,[12] the working principle is basically adiabatic quantum pumping. Hence, simultaneous generation of both dc spin and charge current is the norm. The condition of zero dc charge current, however, is met only for some judicious choices for the values of the system parameters.

It is known, on the other hand, that quantum transport in a narrow channel exhibits resonant inelastic scattering (RIS) features when it is acted upon by a spatially localized time-modulated potential.[14,15] This RIS is coherent inelastic scattering, but with resonance at work, when the traversing electrons can make transitions to their subband threshold by emitting $m\hbar\Omega$.[14,15] Should this RIS become spin resolved in a Rashba-type quantum channel (RQC), of which its Rashba coupling parameter is time modulated locally, we will have a simpler route to the nonmagnetic generation of dc SC. Thus, we opt to study, in this work, the RIS features in a RQC. This requires us to go beyond the adiabatic regime and into the regime when either μ or $\mu_n \sim \hbar\Omega$. We solve the time-dependent spin-orbit scattering (SOS) for all possible incident electron energies and obtain large RIS contribution. In the adiabatic regime, however, with μ, $\mu_n \gg \hbar\Omega$, we find that the dc spin-pumping effect from a sole SOI time-modulated region is small.[12]

II. SYSTEM CONFIGURATION

The system configuration considered is based on a RQC that forms out of a 2DEG in an asymmetric quantum well by the split-gate technique. As is depicted in Fig. 1(a), a finger gate (FG) is positioned above while separated from the RQC by an insulating layer. A local time variation in the Rashba coupling parameter $\alpha(\mathbf{r},t)$ can be induced by ac biasing the FG.[12,13] The Hamiltonian is given by $\mathcal{H}=p^2/2m+\mathcal{H}_{so}(\mathbf{r},t)+V_c(y)$ where the Rashba term

$$\mathcal{H}_{so}(\mathbf{r},t)=\mathbf{M}\cdot\tfrac{1}{2}[\alpha(\mathbf{r},t)p+p\alpha(\mathbf{r},t)]. \quad (1)$$

Here, $\mathbf{M}=\hat{\mathbf{z}}\times\boldsymbol{\sigma}$, $\hat{\mathbf{z}}$ is normal to the 2DEG, $\boldsymbol{\sigma}$ is the vector of Pauli spin matrices, and $V_c(y)$ is the confinement potential. The unperturbed Rashba coupling parameter $\alpha(\mathbf{r},t)$ is α_0 throughout the RQC, but becomes $\alpha_0+\alpha_1\cos\Omega t$ in the region underneath the ac-biased FG. The Dresselhaus term is neglected for the case of a narrow-gap semiconductor system.[16]

To demonstrate the pumping mechanism, we consider a narrow RQC in which its subband energy spacing is much greater than the Rashba-induced subband mixing. As such, the unperturbed Hamiltonian, in its dimensionless form, is $\mathcal{H}_0=-\nabla^2+\alpha_0\sigma_y(i\partial/\partial x)+V_c(y)$. Appropriate units have been used such that all physical quantities presented here, and henceforth, are dimensionless.[15] In particular, α is in unit of $v_F^*/2$, and spin in unit of $\hbar/2$. The right-going (R) eigenstate of $\mathcal{H}_0$, in the nth subband, is $\phi_n(y)\psi_n^\sigma(x)$, where $\psi_n^\sigma(x)=\exp[ik_{n,R}^\sigma x]\chi_\sigma$. The wave vector $k_{n,R}^\sigma=\sqrt{\mu_n+\eta_\sigma\alpha_0/2}$,

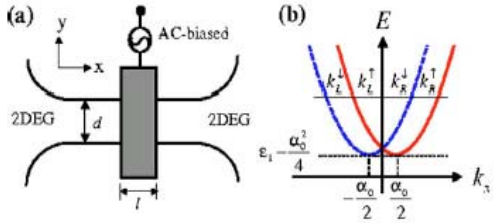

FIG. 1. (Color online) (a) Top-view schematic illustration of the RQC. The ac-biased FG, of width l, is indicated by the gray area; (b) the electron dispersion relation of an unperturbed RQC.

while $\eta_\sigma = \pm 1$ denotes the eigenvalue of χ_σ to the operator σ_y. μ_n is the energy measured from the nth subband threshold such that the energy of the eigentstate is $E = \mu_n + \varepsilon_n - \alpha_0^2/4$, for $\varepsilon_n = (n\pi/d)^2$. This dispersion relation is shown in Fig. 1(b). The subband with $\mu_n \sim \hbar\Omega$ is found to contribute most to the RIS-enhanced spin pumping. It is of import to note that right-going electrons have $|k_R^\uparrow| > |k_R^\downarrow|$ and that, at the subband threshold, $k_R^{\uparrow(\downarrow)} = k_L^{\uparrow(\downarrow)}$.

III. PHYSICAL PICTURE

In this section, we show that the physical origin of the dc SC generation can be understood from two perspectives. A weak pumping regime result is then obtained for an explicit confirmation of our physical reasoning.

The first perspective is associated with the vector potential. In the ac-biased region, $\mathcal{H} = \mathcal{H}_x + \mathcal{H}_y$, the transverse part $\mathcal{H}_y = -\partial^2/\partial y^2 + V_c(y)$, and the longitudinal part

$$\mathcal{H}_x(t) = \left(-i\frac{\partial}{\partial x} + \frac{\alpha(x,t)}{2}\mathbf{M}\cdot\hat{x} \right)^2 - \frac{1}{4}\alpha(x,t)^2. \tag{2}$$

The form of Eq. (2) suggests an effective vector potential, $\mathbf{A}(t) = \frac{1}{2}\alpha(x,t)\mathbf{M}\cdot\hat{x}$, which depends on the spin and gives rise to a spin-resolved driving electric field $\mathbf{E} = -\partial\mathbf{A}/\partial t$. However, in $\mathcal{H}_x$, the A^2 term does not depend on $\boldsymbol{\sigma}$, while for the term linear in $\mathbf{A}$, $\mathbf{A}\chi_\sigma = -\frac{1}{2}\eta_\sigma\alpha(x,t)\chi_\sigma$ gives rise only to a trivial spin dependence, which can be easily removed by a shift in the origin of time for the case of an oscillatory $\alpha(x,t)$. Yet it turns out that the full term linear in $\mathbf{A}$, given by $-i(\partial/\partial x)\hat{x}\cdot\mathbf{A}$, manages to give rise to nontrivial spin-resolved transmissions. In a perturbative sense, this term becomes $k_R^{\uparrow(\downarrow)}A_x$, for the case of a right-going electron incident upon a spatially uniform $\alpha(t)$. This renders the effective longitudinal driving field to become spin dependent, through the factor $k_R^{\uparrow(\downarrow)}$. The difference in the current transmissions, for spin-up and spin-down cases, is proportional to the difference in $k_R^{\uparrow(\downarrow)}$, or α_0, and is found to be amplified by RIS. This breaking of the longitudinal symmetry in the effective driving field by α_0 leads to the generation of dc spin current in a FG-RQC structure that has but an apparent longitudinal configuration symmetry, and with zero source-drain bias. No dc charge current will be generated, however, in such a structure.

An alternate perspective for the understanding of the origin of the spin-resolved current transmission is associated with a unitary transformation. By introducing a unitary transformation $\Psi_\sigma(x,t) = \exp[(i\eta_\sigma/2)\int_{-l/2}^{x}\alpha(x',t)dx']\psi_\sigma(x,t)$, the Schrödinger equation [Eq. (2)] becomes

$$\left[-\frac{\partial^2}{\partial x^2} + U_1(t) + U_2^\sigma(t) \right]\psi_\sigma(x,t) = i\frac{\partial}{\partial t}\psi_\sigma(x,t), \tag{3}$$

of which the two time-dependent potentials are $U_1(t) = -\alpha(x,t)^2/4$ and $U_2^\sigma(t) = (\Omega\alpha_1/2)(x+l/2)\cos(\Omega t + \eta_\sigma\pi/2)$. Even though only U_2^σ depends on spin, both the term in $U_1(t)$ that oscillates with frequency Ω and U_2^σ together constitute a pair of quantum pumping potential that pump SC. This is our major finding in this work: that spin pumping nature is built-in even in a single FG configuration.

The SC expression for a state Ψ_σ is given by the SC density operator

$$\hat{J}_x^y = i\left[\frac{\partial\Psi_\sigma^\dagger}{\partial x}\sigma_y\Psi_\sigma - \text{H.c.} \right] + \frac{\alpha}{2}\Psi_\sigma^\dagger\{\sigma_y, \mathbf{M}\}_x\Psi_\sigma. \tag{4}$$

The SC conservation is maintained by the supression of subband mixing and the associated spin-flipping in a RQC. For a scattering state Ψ_σ, the SC can be expressed in terms of the transmission coefficients. More specifically, the ratio between the time-averaged transmitted and the incident SC gives the spin-resolved current transmission $T_{\beta\alpha}^\sigma$, where α, β, are, respectively, the incident and the transmitting lead. Summing over contributions from all states in reservoirs R and L, the SC is

$$I^s = I^\uparrow - I^\downarrow,$$

where

$$I^\sigma = \int dE f(E)[T_{RL}^\sigma - T_{LR}^\sigma], \tag{5}$$

and I^σ is the number current due to electrons with spin η_σ from both reservoirs that are under zero source-drain bias condition. Here $T_{RL}^\sigma = \Sigma_n\Sigma_{m(\mu_n^m>0)}T_{n,RL}^{m,\sigma}$ and $f(E)$ is the Fermi-Dirac distribution. The transmission coefficient $T_{n,RL}^{m,\sigma} = |t_{n,RL}^{m,\sigma}|^2\sqrt{\mu_n^m/\mu_n}$ denotes the current transmission that an electron incident from terminal L in the spin channel σ, subband n, energy E, is scattered into terminal R, sideband m, with kinetic energy $\mu_n^m = \mu_n + m\Omega$. The net charge current is given by $I^q = I^\uparrow + I^\downarrow$. In a symmetric FG configuration, we have $T_{LR}^\sigma = T_{RL}^{-\sigma}$, so that the net spin current is $I^s = 2\int dE f(E)(T_{RL}^\uparrow - T_{RL}^\downarrow)$ and the net charge current is identically zero.

In the weak pumping (WP) regime, when α_1 is small, we can demonstrate analytically, and most unequivocally, that spin-dependent reflection arises merely from the aforementioned linear $\mathbf{A}$ term in $H_x(t)$. We outline the derivation here while leaving the detail in Appendix A. Tracing up to the first order in α_1, our derivation retains the reflection amplitudes to $m = \pm 1$ sideband and drops that to the $m = 0$ sideband. Contribution to the total reflection includes thus reflection at either the left or the right edges of the time-modulated region. For an electron incident from terminal L with wave vector $k_{n,R}^\sigma(E)$, the reflection at the left edge is obtained from the wave-function continuous condition and the boundary condition

$$-\frac{\partial}{\partial x}\Psi_\sigma\big|_{x=(-l/2)^+} + \frac{\partial}{\partial x}\Psi_\sigma\big|_{x=(-l/2)^-} + \frac{i}{2}\eta_\sigma\alpha_1\cos\Omega t\,\Psi_\sigma\big|_{x=-l/2} = 0. \tag{6}$$

In the time-modulated region, the wave function Ψ_σ consists of one-sideband terms, given by the form $e^{ik_{n,R}^\sigma(E\pm\Omega)x}e^{-i(E\pm\Omega)t}$, and the $m = 0$ term, given by the form $e^{ik_{n,R}^\sigma(E)x}e^{-iEt}[1 + \eta_\sigma/(2\Omega)\alpha_1 k_{n,R}^\sigma(E)(e^{i\Omega t} - e^{-i\Omega t})]$. The extra Ωt dependence in the $m = 0$ term is resulted from the time-dependent driving effect of $\mathbf{A}$, which is obviated by the

weighting factor that involves $\alpha_1 k_{n,R}^{\sigma}$. The reflection amplitude $r_L^{m,\sigma}$ at the left edge is obtained to be

$$r_L^{m,\sigma} = \mathrm{sgn}(m)\frac{\eta_\sigma}{2}\frac{\left[\frac{\alpha_1}{\Omega}k_{n,R}^{\sigma}(k_{n,R}^{\sigma}-k_{n,R}^{m,\sigma})+\frac{\alpha_1 m}{2}\right]}{k_{n,R}^{m,\sigma}-k_{n,L}^{m,\sigma}} \times e^{-i(k_{n,R}^{\sigma}-k_{n,L}^{m,\sigma})l/2} \quad (7)$$

for $m=\pm 1$. The first term in the numerator of Eq. (7) is clearly due to **A**, because of the factor $\alpha_1 k_{n,R}^{\sigma}$, and the second term is due to the scattering at the edge. Here the wave vector $k_{n,R(L)}^{m,\sigma}=\pm(\mu_n^m)^{1/2}+\eta_\sigma\alpha_0/2$, with upper (lower) sign corresponds to the right-(left-) moving electron in the nth subband, mth sideband, and with kinetic energy μ_n^m. It is clear then that wave-vector differences in both the numerator and the denominator of $r_L^{m,\sigma}$ are spin independent. Hence, the spin dependence arises solely from the $\alpha_1 k_{n,R}^{\sigma}$ factor in the first term of the numerator in Eq. (7), or from **A**. This confirms our understanding of the physical origin of the dc SC generation.

Including the reflection at the right edge, we obtain the total reflection amplitude

$$r_{n,LL}^{m,\sigma} = [1 - e^{i(k_{n,R}^{\sigma}-k_{n,L}^{m,\sigma})l}]r_L^{m,\sigma}. \quad (8)$$

We note that the spin dependence of this total reflection amplitude is associated with α_0. In fact, it turns out that the SC is proportional to α_0. The SC is related to the current transmission, which, within the aforementioned approximation, is given by $T_{RL}^{\sigma}\approx 1-\Sigma_n[R_{n,LL}^{1,\sigma}+R_{n,LL}^{-1,\sigma}]$, where $R_{n,LL}^{m,\sigma}=|r_{n,LL}^{m,\sigma}|^2\sqrt{\mu_n^m}/\sqrt{\mu_n}$. From Eq. (5), the energy derivative of the zero-temperature SC is given by $\partial I^s/\partial E=2\Delta T_{RL}=2(T_{RL}^{\uparrow}-T_{RL}^{\downarrow})$ from which its explicit expression is given by

$$\frac{\partial I^s}{\partial E}=\frac{1}{2}\alpha_0\alpha_1^2\sum_n\sum_{m=\pm 1\ (\mu_n^m>0)}\frac{\{1-\cos[(\sqrt{\mu_n}+\sqrt{\mu_n^m})l]\}\left[\left(\frac{1}{4}\right)^2-\left(\frac{1}{\Omega}(\mu_n-\sqrt{\mu_n\mu_n^m})+\frac{m}{4}\right)^2\right]}{\mu_n\sqrt{\mu_n^m}}. \quad (9)$$

That this expression diverges when $\mu_n^m=0$, for $m<0$, exhibits the RIS feature unambiguously and also demonstrates the need to go beyond the one-sideband approximation near the RIS condition.

IV. NUMERICAL RESULTS AND DISCUSSIONS

In the following, we present results obtained from solving the time-dependent SOS exactly, in the numerical sense. An outline of the method is presented in Appendix B. Physical parameters are chosen to be consistent with the InGaAs-InAlAs–based narrow-gap heterostructures such that the electron density $n_e=1\times 10^{12}$ cm^{-2}, effective mass $m^*=0.04m_0$, and $\alpha_0=0.13$ ($\hbar\alpha_0=3\times 10^{-11}$ eV m).[9] Accordingly, the length unit $l^*=4.0$ nm and the energy unit $E^*=59$ meV.

For the case of one FG ($N=1$), the energy dependence of the spin-resolved transmission T_{RL}^{σ} is plotted in Figs. 2(a)–2(c), and that of the corresponding dc SC is plotted in Fig. 2(d). The FG width $l=20$ (80 nm), driving frequency $\Omega=0.002$ ($\nu=\Omega/2\pi\approx 28$ GHz), and energy $\mu=E-\varepsilon_1$. Dip features in T_{RL}^{σ} at $\mu/\Omega=1$ are the quasi-bound state (QBS) features, where electrons undergo coherent inelastic scattering to a QBS just beneath its subband bottom.[14] Higher-order QBS features at $\mu/\Omega=2$ are barely shown by the small peaks. Of particular interest is the change in sign in the transmission difference $\Delta T_{RL}=T_{RL}^{\uparrow}-T_{RL}^{\downarrow}$ across the dip structures, namely, $\Delta T_{RL}(\mu=\Omega^-)>0$ while $\Delta T_{RL}(\mu=\Omega^+)<0$. This leads to a nonzero dc SC, peaked at $\mu/\Omega=1$, and is exhibited in Fig. 2(d).

It is also shown that the dc SC increases with the oscillating amplitude α_1 of the ac-biased gate voltage. More importantly, all the above dc SC characteristics, including even their order of magnitudes, are already captured by Eq. (9). This lends strong support to our finding that RIS has played a pivotal role in the generation of dc SC. Similar RIS-induced peak in I^s is found if we vary d instead of μ.

The nonlinear enhancement in the dc SC by two FGs ($N=2$) is presented in Figs. 3(a)–3(c). The driving frequency

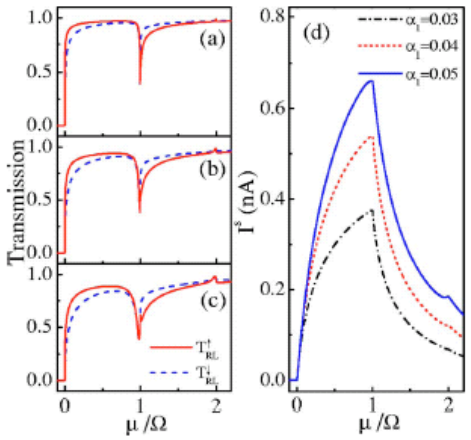

FIG. 2. (Color online) Spin-resolved current transmissions $T_{RL}^{\uparrow}$ (solid) and $T_{RL}^{\downarrow}$ (dashed) versus the incident energy μ/Ω. Parameters $N=1$, $\alpha_0=0.13$, $\Omega=0.002$, $l=20$, and $\alpha_1=$(a) 0.03, (b) 0.04, and (c) 0.05. The corresponding dc SC is plotted in (d).

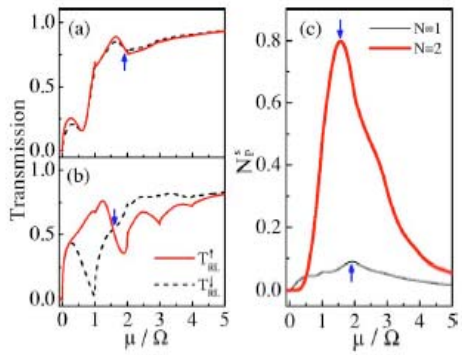

FIG. 3. (Color online) Current transmission versus μ/Ω for N=(a) 1, and (b) 2. Pumped spins per cycle are plotted in (c) for N=1 (thick curve) and N=2 (thin curve) with α_1=0.065, and driving frequency Ω=0.001. Other parameters are the same as in Fig. 2.

is chosen to be Ω=0.001 ($\nu \approx 14$ GHz), and with l=22 ($\simeq$88 nm). For comparison, the N=1 FG transmissions are plotted along with that of the N=2 FG case, in Figs. 3(a) and 3(b), respectively. The corresponding dc SC, expressed in terms of pumped spins per cycle $N^s_P=(2\pi/\Omega)|I^s|$, is shown in Fig. 3(c). The pumping is optimized by a choice of the FG separation, with the edge-to-edge separation Δl=22. The QBS dip structures are significant up to the fourth sideband in Fig. 3(b). As indicated by arrows, the pumped spin-per-cycle peaks at $\mu/\Omega \simeq 1.57$ (1.92), with peak value 0.8 (0.1) for the N=2 (N=1) FG case. The enhancement in N^s_P is far greater than doubling the N^s_P of N=1 FG. Finally, we discuss the effectiveness of tuning α. Grundler showed that a static FG bias change $\Delta V_{\mathrm{FG}} \sim 0.075$ V can tune $\Delta\alpha \sim 0.25\alpha_0$.[10] This tuning ability should remain valid in ac FG bias if the wave function in the asymmetric quantum well responses adiabatically. We estimate the quantum-well energy-level spacing $\Delta E \sim 0.08$ eV $\gg \hbar\Omega \sim 0.06$ meV, for $\Omega/(2\pi)$=14 GHz. Thus, the adiabatic response of the wave function in the quantum well is established. Furthermore, the ac FG biases, with amplitude $\Delta V_{\mathrm{FG}} \sim 0.075$ V, is estimated to be within reach of coaxiable cable technology.[17]

V. CONCLUSION

In conclusion, a nonmagnetic way of generating dc SC has been established. The proposed Rashba-type quantum channel driven by an ac-biased finger gate is a simple structure and should be within reach of recent fabrication capability. The spin pumping is studied, in detail, in both its nature and its pumping mechanism. A resonant inelastic process is the major factor that contributes to the robustness of the spin pumping. The coherent nature of the pumping supports further enhancement of the spin pumping by invoking configuration consisting of more than one finger gate.

ACKNOWLEDGMENTS

The authors acknowledge valuable discussions with A. G. Mal'shukov. This work was funded by the National Science Council of ROC under Grants No. NSC92-2112-M-009-035, No. NSC92-2120-M-009-010, No. NSC93-2112-M-009-036, and No. NSC93-2119-M-007-002 (NCTS).

APPENDIX A: WEAK-PUMPING (WP) REGIME

In the WP regime, we can obtain analytic results. The WP regime refers to the case when the Rashba coupling parameter oscillates with a small amplitude α_1. Keeping only up to the lowest nonvanishing contribution of α_1, it is simpler to calculate the reflection amplitudes than the transmission coefficients. The reflection amplitudes to $m=\pm 1$ sidebands are first order in α_1 and are the major objects of our calculation here. The reflection amplitudes to m=0 sideband, however, is second order in α_1 and is neglected. When the Rashba coupling parameter oscillates in time within a spatial region $-l/2<x<l/2$, the longitudinal Hamiltonian is given by

$$H_x = -\frac{\partial^2}{\partial x^2} + \alpha_0\sigma_y\left(i\frac{\partial}{\partial x}\right) + \frac{\alpha_1 \cos\Omega t}{2}\sigma_y \times\left[\theta(l/2-|x|)\left(i\frac{\partial}{\partial x}\right) + \left(i\frac{\partial}{\partial x}\right)\theta(l/2-|x|)\right], \quad \text{(A1)}$$

where $\theta(x)$ is the step function. For an electron incident from terminal L with wave vector $k^{\sigma}_{n,R}(E)$, the reflection coefficients consist of contributions from reflections at the left and the right edges of the time-modulated region. We first calculate the reflection amplitudes due to reflection at $x=-l/2$. The wave function is given by

$$\psi^{\sigma}_n(x<-l/2) = e^{ik^{\sigma}_{n,R}(E)x}e^{-iEt} + \sum_{\substack{m=\pm1\\(m\neq0)}} r^{m,\sigma}_L e^{ik^{m,\sigma}_{n,L}x}e^{-i(E+m\Omega)t}, \quad \text{(A2)}$$

$$\psi^{\sigma}_n(-l/2<x<l/2) = \sum_{\substack{m=\pm1\\(m\neq0)}} t^{m,\sigma}_L e^{ik^{m,\sigma}_{n,R}x}e^{-i(E+m\Omega)t} + t^{0,\sigma}_L e^{ik^{\sigma}_{n,R}(E)x}e^{-iEt}\left[1+\frac{\eta_\sigma}{2\Omega}\alpha_1 k^{\sigma}_{n,R}(E)(e^{i\Omega t}-e^{-i\Omega t})\right]. \quad \text{(A3)}$$

Here, $t^{m,\sigma}_L$ and $r^{m,\sigma}_L$ denote, respectively, the transmission and reflection coefficients at the left edge of the time-modulated region. We have not included, in Eq. (A3), corrections to the wave functions associated with the coefficients $t^{m,\sigma}_L$, for $m=\pm1$, that arise from the time-modulation of the Rashba spin-orbit intraction (SOI). It is because the coefficients $t^{m,\sigma}_L$ are already first order in α_1. These coefficients are solved from the wave-function continuous condition and the boundary condition in Eq. (6). The reflection coefficients are calculated, and the expression is presented in Eq. (7). It is worth noting that $t^{0,\sigma}_L=1$, up to first order in α_1.

Following a similar procedure, the reflection at the right edge of the time-modulated region can be obtained from the following wave function:

Appendix D:

Available online at www.sciencedirect.com
SCIENCE DIRECT®
Physica E 32 (2006) 450–453
PHYSICA E
www.elsevier.com/locate/physe

Effects of an elastic scatterer on the DC spin current generation in a Rashba-type quantum channel

L.Y. Wang[a], C.S. Tang[b], C.S. Chu[a,*]

[a]Department of Electrophysics, National Chiao-Tung University, Hsinchu 30010, Taiwan
[b]Physics Division, National Center for Theoretical Sciences, P.O. Box 2-131, Hsinchu 30013, Taiwan

Available online 7 March 2006

Abstract

In this work, we consider a Rashba-type quantum channel (RQC) consisting of one AC-biased finger-gates (FG) that orient perpendicularly and located above the RQC. Such an AC-biased FG gives rise to a local time-modulation in the Rashba coupling parameter, and is shown recently to generate a DC spin current [L.Y. Wang, C.S. Tang, C.S. Chu, Cond-mat/0409291, 2004]. No charge current, however, is generated in this configuration. We explore the robustness of such DC spin current generation against elastic scattering in the RQC. The effect of backscattering is studied by introducing a static barrier that is uniform in the transverse dimension. The effects of both backscattering and subband mixing is studied by introducing a static partial-barrier that is spatially localized and non-uniform in the transverse dimension. In addition, we compare the cases of attractive and repulsive partial-barriers. It is found that attractive partial-barrier gives rise to additional DC spin current structures due to resonant inter-subband and inter-sideband transition to quasi-bound states formed just beneath subband thresholds.

PACS: 72.20.−i; 72.20.Dp; 72.25.Mk

Keywords: Rashba coupling parameter; Spin current; Inter-subband; Backscattering; Inter-sideband; Quasi-bound states

1. Introduction

Recent interest in spintronics has been prompted by its great potential in physical realization of quantum computation [1–3]. One of the important issue in spintronics is the generation of DC spin current (SC).Various schemes for the DC SC generation have recently been proposed, which involve a non-uniform magnetic field [4] or an oscillating magnetic field [5]. An alternate way to control the electron spin dynamics is via *Rashba*-type *spin-orbit interaction* (SOI) [6]. Several proposals have been suggested to generate DC SC with a time-varying *Rashba*-type SOI [1,7,8]. The *Rashba* term can be described by $H_{SO} = \alpha(\vec{p} \times \hat{z}) \cdot \vec{\sigma}$ where α denotes the spin-orbit (SO) coupling parameter and $\vec{\sigma}$ stands for the Pauli spin matrices. That α can be tuned by an external gate voltage in the InAs-based heterostructure has been demonstrated experimentally [9,10]. In the presence of such an oscillating α induced by an AC-biased gate, it was found that AC SC is generated in a ballistic quantum channel [7] or in a diffusive 2DEG [8]. Rectification, such as introducing an additional oscillating barrier is needed for the DC SC generation [7,8]. Beyond linear response to α, we find that a DC SC can be generated via a single AC-biased FG atop a ballistic *Rashba*-type quantum channel [1]. No charge current, however, is generated. Resonance inelastic scattering (RIS) is found to contribute to the robustness in the DC SC [1].

In this work, we study the effect of elastic scattering on the DC SC generation in a single FG configuration. The method of approach is time-dependent scattering matrix method [1,11]. The backscattering effect can be studied via a static full-barrier locating either inside or outside of the AC-biased FG. Strong barrier position-dependent effect on the DC SC generation is found in our theoretical calculation.

The elastic scattering effect is further studied by considering a repulsive or attractive partial-barrier. The

*Corresponding author. Tel.: +886 3 5712121x56127; fax: +886 3 5725230.
E-mail address: cschu@cc.nctu.edu.tw (C.S. Chu).

partial-barrier introduces intersubband scattering to the system due to the fact that it covers only part of the transverse dimension of the quantum channel. We have studied the barrier position dependence of the DC SC generation. For an attractive partial-barrier, the intersubband transition into a quasi-bound state formed just beneath the subband bottom causes the SC to have an additional structure at μ below the second subband bottom.

In all the above elastic scattering effect on the DC SC, as long as the barrier breaks the longitudinal symmetry of the configuration, the charge current (CC) will become nonzero.

2. Method of approach

The schematic structure shown in Fig. 1 is based on a RQC that forms out of a 2DEG in an asymmetric quantum well by the split-gate technique, and a single barrier is located in the RQC. This effective Hamiltonian is given by $H = p^2/2m + H_{SO}(\vec{r}, t) + V_c(y) + f_0(y)\delta(x - x_0)$, where $p = (p_x, p_y)$ is the in-plane momentum, $H_{SO}(\vec{r}, t)$ is the *Rashba* term, and $V_c(y)$ is the confinement potential. In the case of a full-barrier, $f_0(y) = V_0$ in the entire width of the quantum channel $0 \leqslant y \leqslant d$. In the case of a partial-barrier, $f_0(y) = V_0$ in the region $y_1 \leqslant y \leqslant y_2$, with $0 \leqslant y_1$, $y_2 \leqslant d$, and $f_0(y) = 0$ for other regions.

The unperturbed RQC we considered is narrow so that its subband energy spacing is much greater than the subband mixing due to the *Rashba* interaction. As such the unperturbed Hamiltonian in the dimensionless form is given by $\mathscr{H}_0 = -\nabla^2 + \alpha_0\sigma_y(i\partial/\partial x) + V_c(y)$. Here we have chosen appropriate units for all physical quantities [1]. In particular, α is in unit of $v_F/2$, where v_F denotes the Fermi velocity, and spin is in unit of $\hbar/2$. The right-going (R) eigenstate of $\mathscr{H}_0$, in the nth subband, is $\phi_n(y)\psi_n^\sigma(x)$, where $\psi_n^\sigma(x) = \exp(ik_{n,R}^\sigma x)\chi_\sigma$. The wavevector $k_{n,R}^\sigma = \sqrt{\mu_n} + \eta_\sigma\alpha_0/2$ while $\eta_\sigma = \pm 1$ denotes the eigenvalue of χ_σ to the operator σ_y. μ_n is the energy measured from the nth subband threshold such that the energy of the eigenstate is $E = \mu_n + \varepsilon_n - \alpha_0^2/4$, for $\varepsilon_n = (n\pi/d)^2$. In the AC-biased FG region, the *Rashba* coupling parameter becomes $\alpha(t) = \alpha_0 + \alpha_1\cos\Omega t$. Introducing a unitary transformation $\psi_n^\sigma(x) = e^{\eta_\sigma(\alpha_1/\Omega)\sin(\Omega t)(\partial/\partial x)}\varphi_n^\sigma(x)$ in this region, leads us to the time-dependent longitudinal Schrödinger equation

$$\left(-\frac{\partial^2}{\partial x^2} + i\alpha_0\sigma_y\frac{\partial}{\partial x}\right)\varphi_n^\sigma(x) = i\frac{\partial}{\partial t}\varphi_n^\sigma(x). \tag{1}$$

Thus a general form of $\psi_n^\sigma(x)$ in the time-modulated region is given by

$$\psi_n^\sigma(x,t) = \sum_{m,m'}\{A_n^{m',\sigma}e^{ik_{n,R}^{m,\sigma}x}J_{m-m'}(\tilde{k}_{n,R}^{m,\sigma}) + B_n^{m',\sigma}e^{ik_{n,L}^{m',\sigma}x}J_{m-m'}(\tilde{k}_{n,L}^{m',\sigma})\}(-\eta_\sigma)^{m-m'}e^{-i\mu_n^m t}. \tag{2}$$

Here the sideband energy is denoted by $\mu_n^m = \mu_n + m\Omega$, the spin-dependent wavevector is denoted by $k_{n,R(L)}^{m,\sigma} = \pm(\mu_n^m)^{1/2} + \eta_\sigma\alpha_0/2$, with the upper (lower) sign corresponds to the right- (left-) going electron, and $\tilde{k}_{n,R(L)}^{m,\sigma} = (\alpha_1/\Omega)k_{n,R(L)}^{m,\sigma}$. The wavefunction in Eq. (2) is to be matched with that outside the time-modulated region at all times in order to obtain the transmission coefficients. At the boundary of the time-modulated region, we apply the wavefunction continuous condition, and the condition connecting the slopes of the wavefunction, which are obtained from the Schrödinger equation.

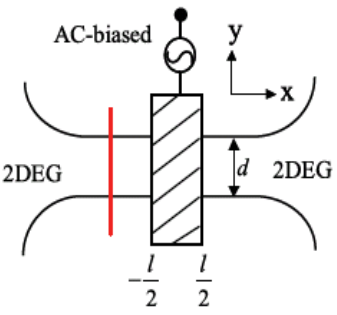

Fig. 1. Top-view schematic illustration of the RQC with a static barrier. The AC-biased FG, of width l, is indicated by the shaded area. The solid line at the left of the FG indicates the static barrier.

3. Results and discussion

We first present numerical results for the case of a full-barrier. The physical parameters are chosen to be consistent with InGaAs–InAlAs based narrow gap heterostructure such that the electron density $n_e = 1 \times 10^{12}\,\mathrm{cm}^{-2}$, effective mass $m^* = 0.04m_0$, and $\alpha_0 = 0.13$ ($\hbar\alpha_0 = 3\times 10^{-11}\,\mathrm{eV\,m}$) [10]. The length unit is $l^* = 4.0\,\mathrm{nm}$, and the energy unit is $E^* = 59\,\mathrm{meV}$. We present in Fig. 2 the dependence of the SC (empty-symbols) and the CC (filled-symbols) on channel width d for a number of barrier positions. The driving frequency is $\Omega = 0.002$ ($\approx 28\,\mathrm{GHz}$), the FG length $l = 20$ (80 nm), and the barrier strength is $V_0 = 0.1$. For a fixed Fermi energy E, the nth subband bottom matches E when $E = (n\pi/d)^2 - \alpha_0^2/4$. Thus in Fig. 2, when $E = 0.0131$, the first and the second subband bottoms match that of E when $d = 23.86$ and 47.73, respectively. The SC (I^s) and CC (I^c) are defined by $I^S = I^\uparrow - I^\downarrow$, and $I^C = I^\uparrow + I^\downarrow$, where

$$I^\sigma = \int dE f(E)\left[T_{RL}^\sigma - T_{LR}^\sigma\right]. \tag{3}$$

Here $T_{\beta\alpha}^\sigma$ depicts current transmission and α, β denotes the incident and the transmitting lead, respectively. The case of a full-barrier located either inside or outside the time-modulated region is given by Figs. 2(a) and (b), respectively. The trend shown in Fig. 2 is that both the SC and the CC are smaller when the barrier is located inside the time-modulated region. This trend is consistent with another feature in Fig. 2(a): namely that the current is largest for $x_0 = -9.9$, when the barrier is closest to the edge

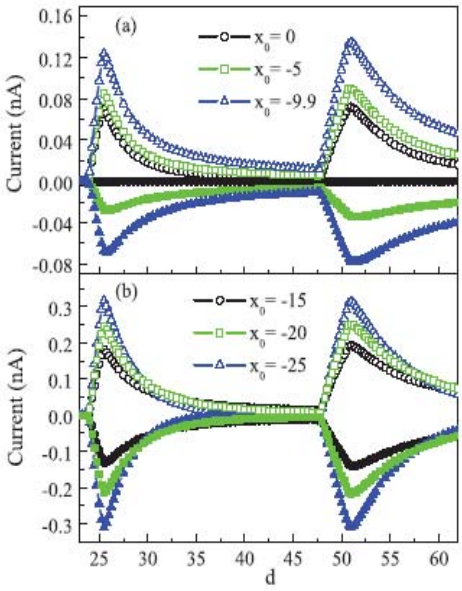

Fig. 2. The SC and CC are plotted as a function of channel width d. The static full-barrier is located (a) inside and (b) outside the FG with various longitudinal positions. The empty-symbols and filled-symbols indicate the SC and the CC, respectively. The Fermi energy is fixed at $E = 0.0131$ and other parameters are $\alpha_0 = 0.13$, $\alpha_1 = 0.03$, $l = 20$, $\Omega = 0.002$, and $V_0 = 0.1$. The center and the edges of the time-modulated regions are at $x_0 = 0, \pm 10$, respectively.

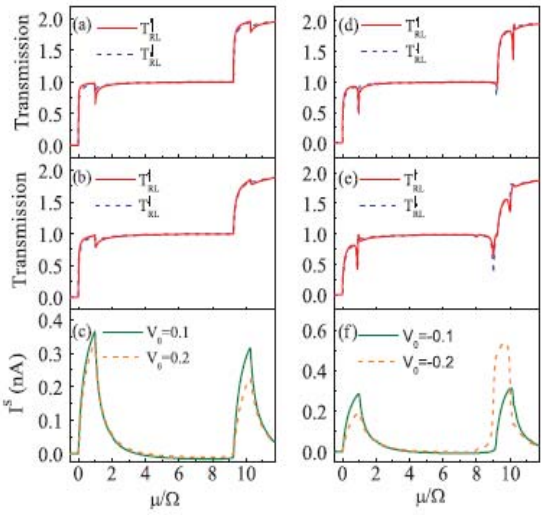

Fig. 3. The repulsive, (a)–(c) and attractive, (d)–(f), partial-barrier is located at the FG center but with various V_0. We choose $V_0 = 0.1$, 0.2, −0.1, −0.2, in (a), (b), (d), (e), respectively. The current transmission is plotted as incident energy in the unit of μ/Ω. Other parameters are $\alpha_0 = 0.13$, $\alpha_1 = 0.03$, $\Omega = 0.002$, $l = 20$, and $d = 40$.

of the time-modulated region, and it is the smallest for $x_0 = 0$, when the barrier is centered. Outside the time-modulated region, the SC and the CC continue to grow with increasing separation between the barrier and the time-modulated region, until they saturate eventually to certain values. Besides this overall trend, the channel width dependence of the SC and CC exhibits distinct signatures of the coherent inelastic processes. The sharp rise in SC occurs when the Fermi energy E aligns with a subband bottom. More importantly, the SC peaks at $d = 25.37$, and 50.75, when the effective Fermi energy μ_n of the highest subband equals $\hbar\Omega$. This is shown to be associated with the coherent inelastic scattering to a quasi-bound state (QBS) just beneath the subband bottom [1,12,13]. The sharp rises of SC in Fig. 2 thus demonstrate that coherent processes have played an important role in the large enhancement of the DC SC. These coherent processes come into effect through the reflections at the two edges of the time-modulated region and through the interference between these reflection amplitudes. A barrier located inside the time-modulated region will therefore cause greater disruption to the aforementioned coherent processes than a barrier located outside the time-modulated region, and hence results in a smaller DC SC pumping.

We present, in Fig. 3, both the transmission and the DC SC characteristics for a partial-barrier located inside the time-modulated region. The partial-barrier has a delta-profile in the longitudinal direction and covers only a fraction of the channel width, which transverse range is from $y_1 = 8$ to $y_2 = 12$. For a RQC width of $d = 40$, the center of the partial-barrier is at $d/4$. Of particular interest here is the effect of the sign of the partial-barrier potential to the SC. The partial-barrier is repulsive, attractive, in Figs. 3(a)–(c), and in Figs. 3(d)–(f), respectively. For the repulsive partial-barrier, the transmission coefficients are spin-resolved and show both step-like structures, due to the subband structures, and the dip structures, due to the coherent inelastic scattering features. The dip structures are broadened for larger V_0. Subsequently, the DC SC is suppressed. For the attractive partial-barrier, the transmission coefficients show additional dip structures at the subband bottom, when $\mu/\Omega \approx 9$. These additional dip structures are due to coherent elastic inter-subband scattering into the QBS state just beneath the subband bottom. On the other hand, the coherent inelastic scattering dip structures develop into dip-and-peak structures for larger $|V_0|$. Subsequently, the DC SC has an additional shoulder, near $\mu/\Omega \approx 8$, before the SC sharp rise at the subband bottom. Moreover, as is shown by the dotted curve in Fig. 3(f), when the partial-barrier is more attractive, the DC SC is suppressed around $\mu/\Omega \approx 1$ but is enhanced around $\mu/\Omega \approx 10$.

4. Summary

We have studied DC SC generation in the presence of either a full-barrier or a partial-barrier in a RQC. In general, a barrier inside the time-modulated region causes a stronger suppression to the SC than it is outside the region. Interestingly, we find that an attractive partial-barrier induces inter-subband processes, gives rise to additional

QBS dip structures in the transmission coefficients, and can lead to the enhancement of the SC.

Acknowledgments

The authors wish to acknowledge the National Science Council of the Republic of China for financially supporting this research under Grant nos. NSC93-2112-M-009-036, and NSC 94-2120-M-009-002.

References

[1] L.Y. Wang, C.S. Tang, C.S. Chu, cond-mat/0409291, 2004.
[2] D.D. Awschalom, N. Samarth, D. Loss (Eds.), Semiconductor Spintronics and Quantum Computation, Springer, Berlin, 2002.
[3] S.A. Wolf, et al., Science 294 (2001) 1488.
[4] Qing-feng Sun, Hong Guo, JianWang, Phys. Rev. Lett. 90 (25) (2003) 8301.
[5] Ping Zhang, Qi-KunXue, X.F. Xie, Phys. Rev. Lett. 90 (19) (2003) 6602.
[6] E.I. Rashba, Fiz. Tverd. Tela (Leningard) 2 (1960) 1224; E.I. Rashba, Sov. Phys. Solid State 2 (1960) 1109; Y.A. Bychkov, E.I. Rashba, J. Phys. C 17 (1984) 6039.
[7] M. Governale, F. Taddei, R. Fazio, Phys. Rev. B 68 (15) (2003) 5324.
[8] A.G. Mal'shukov, C.S. Tang, C.S. Chu, K.A. Chao, Phys. Rev. B 68 (23) (2003) 3307.
[9] J. Nitta, T. Akazaki, H. Takayanagi, T. Enoki, Phys. Rev. Lett. 78 (1997) 1335.
[10] D. Grundler, Phys. Rev. Lett. 84 (2000) 6074.
[11] C.S. Tang, C.S. Chu, Phys. Rev. B 60 (1999) 1830.
[12] C.S. Tang, C.S. Chu, Phys. Rev. B 53 (1996) 4838.
[13] P.F. Bagwell, R.K. Lake, Phys. Rev. B 46 (15) (1992) 329.

Appendix E:

Spin Hall Effect on Edge Magnetization and Electric Conductance of a 2D Semiconductor Strip

A. G. Mal'shukov,[1] L. Y. Wang,[2] C. S. Chu,[2] and K. A. Chao[3]

[1]*Institute of Spectroscopy, Russian Academy of Science, 142190, Troitsk, Moscow oblast, Russia*
[2]*Department of Electrophysics, National Chiao Tung University, Hsinchu 30010, Taiwan*
[3]*Solid State Theory Division, Department of Physics, Lund University, S-22362 Lund, Sweden*

(Received 7 July 2005; published 27 September 2005)

The intrinsic spin Hall effect on spin accumulation and electric conductance in a diffusive regime of a 2D electron gas has been studied for a 2D strip of a finite width. It is shown that the spin polarization near the flanks of the strip, as well as the electric current in the longitudinal direction, exhibit damped oscillations as a function of the width and strength of the Dresselhaus spin-orbit interaction. Cubic terms of this interaction are crucial for spin accumulation near the edges. As expected, no effect on the spin accumulation and electric conductance have been found in case of Rashba spin-orbit interaction.

DOI: 10.1103/PhysRevLett.95.146601 PACS numbers: 72.25.Dc, 71.70.Ej, 73.40.Lq

Spintronics is a fast developing area to use electron spin degrees of freedom in electronic devices [1]. One of its most challenging goals is to find a method for manipulating electron spins by electric fields. The spin-orbit interaction (SOI), which couples the electron momentum and spin, can be a mediator between the charge and spin degrees of freedom. Such a coupling gives rise to the so-called spin Hall effect (SHE) which attracted much interest recently. Because of SOI the spin flow can be induced perpendicular to the dc electric field, as has been predicted for systems containing spin-orbit impurity scatterers [2]. Later, similar phenomenon was predicted for noncentrosymmetric semiconductors with spin split electron and hole energy bands [3]. It was called the *intrinsic* spin Hall effect, in contrast to the *extrinsic* impurity induced effect, because in the former case it originates from the electronic band structure of a semiconductor sample. Since the spin current carries the spin polarization, one would expect a buildup of the spin density near the sample boundaries. In fact, this accumulated polarization is a first signature of SHE which has been detected experimentally, confirming thus the extrinsic SHE [4] in semiconductor films and intrinsic SHE in a 2D hole gas [5]. On the other hand, there was still no experimental evidence of intrinsic SHE in 2D electron gases. The possibility of such an effect in macroscopic samples with a finite elastic mean free path of electrons caused recently much debates. It has been shown analytically [6–11] and numerically [12] that in such systems SHE vanishes at arbitrary weak disorder in dc limit for isotropic as well as anisotropic [10] impurity scattering when SOI is represented by the so-called Rashba interaction [13]. As one can expect in this case, there is no spin accumulation at the sample boundaries, except for the pockets near the electric contacts [7]. At the same time, the Dresselhaus SOI [14], which dominates in symmetric quantum wells, gives a finite spin Hall conductivity [11]. The latter can be of the order of its universal value $e/8\pi\hbar$. The same has been shown for the cubic Rashba interaction in hole systems [12,15]. In this connection an important question is what sort of the spin accumulation could Dresselhaus SOI induce near sample boundaries. Another problem which, as far as we know, was not discussed in literature, is how the *electric* current along the applied electric field will change under SHE. In the present work we will use the diffusion approximation for the electron transport to derive the drift-diffusion equations with corresponding boundary conditions for the spin and charge densities coupled to each other via SOI of general form. Then the spin density near the flanks of an infinite 2D strip and the correction to its longitudinal electric resistance will be calculated for Dresselhaus and Rashba SOI.

Let us consider two-dimensional electron gas (2DEG) confined in an infinite 2D strip. The boundaries of the strip are at $y = \pm d/2$. The electric field E drives the dc current in the x direction and induces the spin Hall current in the y direction. This current leads to spin polarization buildup near boundaries. Since $d \gg k_F^{-1}$, where k_F is the Fermi wave vector, this problem can be treated within the semiclassical approximation. Moreover, we will assume that d is much larger than the electron elastic mean free path l, so that the drift-diffusion equation can be applied for description of the spin and charge transport. Our goal is to derive this equation for SOI of general form

$$H_{so} = \boldsymbol{h}_{\boldsymbol{k}} \cdot \boldsymbol{\sigma}, \tag{1}$$

where $\boldsymbol{\sigma} \equiv (\sigma^x, \sigma^y, \sigma^z)$ is the Pauli matrix vector, and the effective magnetic field $\boldsymbol{h}_{\boldsymbol{k}} = -\boldsymbol{h}_{-\boldsymbol{k}}$ is a function of the two-dimensional wave vector $\boldsymbol{k}$.

We start from determining linear responses to the magnetic $\boldsymbol{B}(\boldsymbol{r}, t)$ and electric $V(\boldsymbol{r}, t)$ potentials. The magnetic potentials are introduced in order to derive the diffusion equation and play an auxiliary role. The corresponding one-particle interaction with the spin density is defined as $H_{sp} = \boldsymbol{B}(\boldsymbol{r}, t) \cdot \boldsymbol{\sigma}$. These potentials induce the spin and charge densities, $\boldsymbol{S}(\boldsymbol{r}, t)$ and $n(\boldsymbol{r}, t)$, respectively. Because of SOI the charge and spin degrees of freedom are coupled, so that the electric potential can induce the spin density [16] and *vice versa*. Therefore, it is convenient to introduce

the four vector of densities $D_i(\boldsymbol{r}, t)$, such that $D_0(\boldsymbol{r}) = n(\boldsymbol{r}, t)$ and $D_{x,y,z}(\boldsymbol{r}, t) = S_{x,y,z}(\boldsymbol{r}, t)$. The corresponding four vector of potentials will be denoted as $\Phi_i(\boldsymbol{r}, t)$. Accordingly, the linear response equations can be written in the form

$$D_i(\boldsymbol{r}, t) = \int d^2r' dt' \sum_j \Pi_{ij}(\boldsymbol{r}, \boldsymbol{r}', t - t')\Phi_j(\boldsymbol{r}', t') + D_i^0(\boldsymbol{r}, t). \quad (2)$$

The response functions $\Pi_{ij}(\boldsymbol{r}, \boldsymbol{r}', t - t')$ can be expressed in a standard way [17] through the retarded and advanced Green functions $G^r(\boldsymbol{r}, \boldsymbol{r}', t)$ and $G^a(\boldsymbol{r}, \boldsymbol{r}', t)$. In the Fourier representation we get

$$\Pi_{ij}(\boldsymbol{r}, \boldsymbol{r}', \omega) = i\omega \int \frac{d\omega'}{2\pi} \frac{\partial n_F(\omega')}{\partial \omega'} \langle \mathrm{Tr}[G^a(\boldsymbol{r}', \boldsymbol{r}, \omega') \times \Sigma_i G^r(\boldsymbol{r}, \boldsymbol{r}', \omega' + \omega)\Sigma_j]\rangle, \quad (3)$$

where $\Sigma_0 = 1$, $\Sigma_i = \sigma_i$ at $i = x, y, z$, and $n_F(\omega)$ is the Fermi distribution function. The time Fourier components of densities $D_i^0(\boldsymbol{r}, t)$ at $\omega \ll E_F$ are defined as

$$D_i^0(\boldsymbol{r}, \omega) = i \int d^2r' \sum_j \Phi_j(\boldsymbol{r}', \omega) \int \frac{d\omega'}{2\pi} n_F(\omega') \times \langle \mathrm{Tr}[G^r(\boldsymbol{r}, \boldsymbol{r}', \omega')\Sigma_i G^r(\boldsymbol{r}', \boldsymbol{r}, \omega')\Sigma_j - G^a(\boldsymbol{r}, \boldsymbol{r}', \omega')\Sigma_i G^a(\boldsymbol{r}', \boldsymbol{k}, \omega')\Sigma_j]\rangle. \quad (4)$$

The trace in Eqs. (3) and (4) runs through the spin variables, and the angular brackets denote the average over the random distribution of impurities. Within the semiclassical approximation the average of the product of Green functions can be calculated perturbatively. Ignoring the weak localization effects, the perturbation expansion consists of the so-called ladder series [17,18]. At small ω and large $|\boldsymbol{r} - \boldsymbol{r}'|$ they describe the particle and spin diffusion processes. The building blocks for the perturbation expansion are the average Green functions $\mathcal{G}^r$ and $\mathcal{G}^a$, together with the pair correlator of the impurity scattering potential $U_{sc}(\boldsymbol{r})$. A simple model of the short-range isotropic potential gives $\langle U_{sc}(\boldsymbol{r})U_{sc}(\boldsymbol{r}')\rangle = \Gamma\delta(\boldsymbol{r} - \boldsymbol{r}')/\pi N_0$, where N_0 is the electron density of states at the Fermi energy and $\Gamma = 1/2\tau$. Within the semiclassical approach the explicit behavior of the electron wave functions near the boundaries of the strip is not important. Therefore, the bulk expressions can be used for the average Green functions. Hence, in the plane wave representation

$$\mathcal{G}^r(\boldsymbol{k}, \omega) = [\mathcal{G}^a(\boldsymbol{k}, \omega)]^\dagger = (\omega - E_{\boldsymbol{k}} - \boldsymbol{h}_{\boldsymbol{k}} \cdot \boldsymbol{\sigma} + i\Gamma)^{-1}, \quad (5)$$

where $E_{\boldsymbol{k}} = k^2/(2m^*) - E_F$. Since the integral in (4) rapidly converges at $|\boldsymbol{r} - \boldsymbol{r}'| \lesssim k_F^{-1}$, $D_i^0(\boldsymbol{r}, \omega)$ are given by the local values of potentials. From (4) and (5) one easily obtains the local equilibrium densities

$$D_i^0(\boldsymbol{r}, \omega) = -2N_0\Phi_i(\boldsymbol{r}, \omega). \quad (6)$$

In their turn, the nonequlibrium spin and charge densities are represented by the first term in Eq. (2). Within the diffusion approximation this term is given by the gradient expansion of (3) [18]. Such an expansion is valid as far as spatial variations of $D_i(\boldsymbol{r}, \omega)$ are relatively small within the length of the order of the mean free path l. The length scale for spin density variations near the boundaries of the strip is given by v_F/h_{k_F}. Hence, the diffusion approximation can be employed only in the dirty limit $h_{k_F} \ll 1/\tau$. The diffusion equation is obtained after the ladder summation in the first term of Eq. (3) and multiplying this equation by the operator inverse to $\Pi_{ij}(\boldsymbol{r}, \boldsymbol{r}', \omega)$, as it has been previously done in [19,20]. After some algebraic manipulations one gets

$$\sum_j \mathcal{D}^{ij}(D_j - D_j^0) = -i\omega D_i, \quad (7)$$

where the diffusion operator $\mathcal{D}^{ij}$ can be written as

$$\mathcal{D}^{ij} = \delta^{ij}D\boldsymbol{\nabla}^2 - \Gamma^{ij} + R^{ijm}\nabla_m + M^{ij}. \quad (8)$$

The first term represents the usual diffusion of the spin and charge densities, while the second one describes the D'akonov-Perel' [21] spin relaxation

$$\Gamma^{ij} = 4\tau\overline{h_{\boldsymbol{k}}^2[\delta^{ij} - n_{\boldsymbol{k}}^i n_{\boldsymbol{k}}^j]}, \quad (9)$$

where $i, j \neq 0$, the overline denotes the average over the Fermi surface, and $\boldsymbol{n}_{\boldsymbol{k}} = \boldsymbol{h}_{\boldsymbol{k}}/h_{\boldsymbol{k}}$. The third term gives rise to precession of the inhomogeneous spin polarization in the effective field of SOI [19]

$$R^{ijm} = 4\tau \sum_l \varepsilon^{ijl}\overline{h_{\boldsymbol{k}}^l v_F^m}. \quad (10)$$

The nondiagonal elements of the form $\mathcal{D}^{i0}$ appear due to spin-orbit mixing of spin and charge degrees of freedom. They are collected in M^{ij}. For Rashba SOI M^{i0} have been calculated in [7,8]. In general case

$$M^{i0} = \overline{\frac{h_{\boldsymbol{k}}^3}{\Gamma^2} \frac{\partial n_{\boldsymbol{k}}^i}{\partial \boldsymbol{k}}} \cdot \boldsymbol{\nabla}. \quad (11)$$

When a time independent homogeneous electric field is applied to the system one has $\Phi_0 = eEx$ and $D_0^0 = -2N_0eEx$. At the same time, $\Phi_i = 0$ and, hence, $D_i^0 = 0$ at $i = x, y, z$. Because of charge neutrality the induced charge density $eD_0 = 0$. It should be noted that in the system under consideration the charge neutrality cannot be fulfilled precisely. The spin polarization accumulated at the strip boundaries gives rise to charge accumulation via the M^{0i} terms in (7) and (8). The screening effect will, however, strongly reduce this additional charge, because the screening length of 2DEG is much less than the typical length scale of spin density variations. We will ignore such a small correction and set $D_0 = 0$ in (7). In this way one

arrives to the closed diffusion equation for three components of the spin density. This equation coincides with the usual equation describing diffusive propagation of the spin density [19], for exception of the additional term $-M^{i0}D_0^0 = 2N_0 eE\overline{h_{\boldsymbol{k}}^3 \nabla_{\boldsymbol{k}}^x n_{\boldsymbol{k}}^i}/\Gamma^2$ due to the external electric field. Its origin becomes more clear in an infinite system where the spin density is constant in space and only Γ^{ij} and M^{ij} are retained in (7) and (8). Hence, the corresponding solution of (8) at $\omega = 0$ is $S_i \equiv S_i^{\mathrm{b}}$, with

$$S_i^{\mathrm{b}} \equiv D_i^0/2 = \frac{N_0 eE}{\Gamma^2} \sum_j (\Gamma^{-1})^{ij} \overline{h_{\boldsymbol{k}}^3 \frac{\partial n_{\boldsymbol{k}}^j}{\partial k_x}}, \qquad (12)$$

where $(\Gamma^{-1})^{ij}$ is the matrix inverse to (9). Such a phenomenon of spin orientation by the electric field was predicted in Ref. [16] and recently observed in [22]. In the special case of Rashba SOI $\boldsymbol{h}_{\boldsymbol{k}} = \alpha(k)(\boldsymbol{k} \times \boldsymbol{z})$ it is easily to get from (12) the result of Ref. [16] $S_y^{\mathrm{b}} = -N_0 eE\alpha\tau$.

In addition to the diffusion equation one needs the boundary conditions. These conditions are that the three components of the spin flux I_x^y, I_y^y, I_z^y flowing in the y direction turn to 0 at $y = \pm d/2$. The linear response theory, similar to (2), gives

$$I_i^l(\boldsymbol{r}, t) = \int d^2 r' dt' \sum_j \Xi_{ij}^l(\boldsymbol{r}, \boldsymbol{r}', t - t') \Phi_j(\boldsymbol{r}', t'), \qquad (13)$$

where the response function Ξ is given by

$$\Xi_{ij}^l(\boldsymbol{r}, \boldsymbol{r}', \omega) = i\omega \int \frac{d\omega'}{2\pi} \frac{\partial n_F(\omega')}{\partial \omega'} \langle \mathrm{Tr}[G^a(\boldsymbol{r}', \boldsymbol{r}, \omega') \times J_i^l G^r(\boldsymbol{r}, \boldsymbol{r}', \omega' + \omega) \Sigma_j] \rangle, \qquad (14)$$

with the one-particle spin-current operator defined by $J_i^l = (\sigma^i \mathrm{v}_l + \mathrm{v}_l \sigma^i)/4$ and the particle velocity

$$\mathrm{v}_l = \frac{k_l}{m^*} + \frac{\partial}{\partial k_l}(\boldsymbol{h}_{\boldsymbol{k}} \cdot \boldsymbol{\sigma}). \qquad (15)$$

Taking into account (7) and (6), we obtain from (13) and (14)

$$I_i^y(\boldsymbol{r}) = -D\frac{\partial S_i}{\partial y} - \frac{1}{2} R^{ijy}(S_j - S_j^{\mathrm{b}}) + \delta_{iz} I_{sH}. \qquad (16)$$

The first two terms represent the diffusion spin current and the current associated with the spin precession. The third term is the uniform spin Hall current polarized along the z axis. It is given by

$$I_{sH} = -\frac{1}{2} R^{zjy} S_j^{\mathrm{b}} + eE \frac{N_0}{\Gamma^2} \overline{v_F^y \left(\frac{\partial \boldsymbol{h}_{\boldsymbol{k}}}{\partial k^x} \times \boldsymbol{h}_{\boldsymbol{k}} \right)_z}. \qquad (17)$$

From (10) and (12) it is easy to see that for Rashba SOI both terms in (17) cancel each other making $I_{sH} = 0$, in accordance with [6–12]. Therefore, in case of the strip the solution of the diffusion equation satisfying the boundary condition is $S_j = \delta_{jy} S_y^{\mathrm{b}}$. Hence, the spin density is uniform and does not accumulate near boundaries. It should be noted that such accumulation can, however, take place in the ballistic regime of electron scattering [23]. At the same time, as shown in Ref. [11], even in the diffusive regime $I_{sH} \neq 0$ for the Dresselhaus SOI. This inevitably leads to the spin accumulation. Taking Dresselhaus SOI in the form

$$h_{\boldsymbol{k}}^x = \beta k_x (k_y^2 - \kappa^2); \qquad h_{\boldsymbol{k}}^y = -\beta k_y (k_x^2 - \kappa^2), \qquad (18)$$

one can see that the bulk spin polarization (12) has a nonzero S_x^{b} component, $R^{zxy} \neq 0$, while $R^{zyy} = 0$. Hence, the solution of the diffusion Eq. (7) with the boundary condition $I_x^y(\pm d/2) = I_z^y(\pm d/2) = 0$ is S_x, $S_z \neq 0$ $S_y = 0$. Let us define $\Delta S_i(y) = S_i(y) - S_i^{\mathrm{b}}$. The dependence of $\Delta S_i(\pm d/2)$ from the strip width, as well as an example of ΔS_z coordinate dependence, are shown in Fig. 1. The damped oscillation in the d-dependence of the spin accumulation on the flanks of the strip can be seen for the S_z polarization. Similar oscillations take place also in the coordinate dependence. The length scale of these oscillations is determined by the spin precession in the effective spin-orbit field.

The arbitrary units have been used in Fig. 1. For a numerical evaluation let us take $E = 10^4$ V/m, $\sqrt{\overline{h_{k_F}^2}}\tau/\hbar = 0.1$, and $\kappa/k_F = 0.8$ for a GaAs quantum

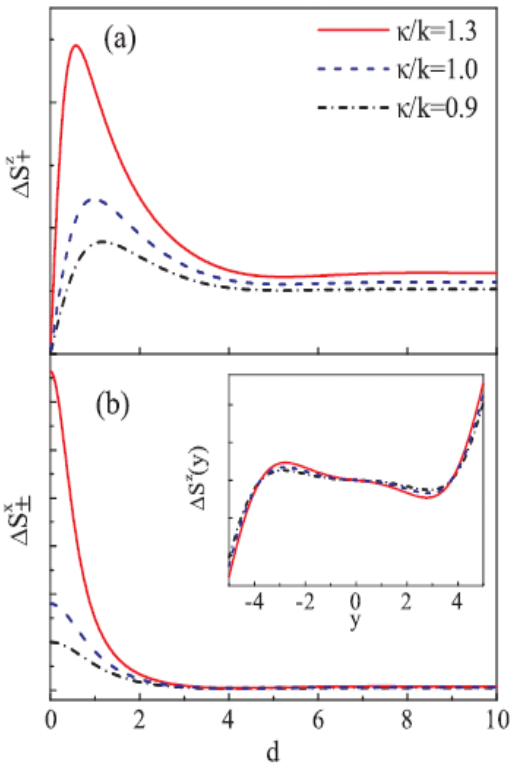

FIG. 1 (color online). Spin densities $\Delta S_i(\pm d/2) \equiv \Delta S_{\pm}^i$ for $i = x, z$ on the boundaries of the strip, as functions of its width d, for $\kappa/k = 0.9$, 1.0, and 1.3, respectively. The inset shows the dependence of $\Delta S_z(y)$ on the transverse coordinate y. Lengths are measured in units of $l_{so} = v_F^2 \hbar/2(\overline{v_{Fy} h_{ky}})$.

well of the width $w = 100$ Å doped with 1.5×10^{15} m^{-2} electrons. We thus obtain $|\Delta S_z(\pm d/2)| \simeq 5 \times 10^{11}$ m^{-2}. The corresponding volume density $\Delta S_z/w \simeq 5 \times 10^{19}$ m^{-3}, which is within the sensitivity range of the Faraday rotation method [4].

It should be noted that in the considered here "dirty" limit $\sqrt{\overline{h_{k_F}^2}}\tau/\hbar \ll 1$ the spin Hall current is suppressed by the impurity scattering. As shown in [11,12] for Dresselhaus and cubic Rashba SOI, this current decreases as $\overline{h_{k_F}^2}\tau^2/\hbar^2$ down from its highest universal value. At the same time, an analysis of the diffusion equation shows that the accumulated at the flanks of the strip spin density decreases slower, as $\sqrt{\overline{h_{k_F}^2}}\tau/\hbar$. This explains why for the considered above realistic numerical parameters, even in the dirty case, the noticeable spin polarization can be accumulated near the boundary.

Usually, the spin Hall effect is associated with the spin polarization flow, or the spin density accumulation on the sample edges, in response to the electric field. On the other hand, this effect can show up in the *electric* conductance as well. To see such an effect we take 0-projection of (13), which by definition is the electric current. The current flows along the x axis. The corresponding response function Ξ_{0j}^x is given by (14) with $J_0^x = v_x$. Using Eqs. (14), (15), and (7), and expressing Φ_i from (6) one gets the electric current density

$$I^x = \sigma E + A\frac{\partial S_z}{\partial y}, \tag{19}$$

where σ is the Drude conductivity and

$$A = e\frac{1}{2\Gamma^2}\left[\overline{2v_F^y\left(\frac{\partial \boldsymbol{h}_{\boldsymbol{k}}}{\partial k^x}\times \boldsymbol{h}_{\boldsymbol{k}}\right)_z} + \overline{v_F^x\left(\frac{\partial \boldsymbol{h}_{\boldsymbol{k}}}{\partial k^y}\times \boldsymbol{h}_{\boldsymbol{k}}\right)_z}\right]. \tag{20}$$

The total current is obtained by integrating (19) over y. Therefore, the spin Hall correction to the strip conductance

$$\Delta G = \frac{A}{E}[S_z(d/2) - S_z(-d/2)] = \frac{2A}{E}S_z(d/2). \tag{21}$$

Hence, the dependence of ΔG on the strip width coincides with that of the spin density shown in Fig. 1(a).

In conclusion, we employed the diffusion approximation to study the spin Hall effect in an infinite 2D strip. In case of the Dresselhaus spin-orbit interaction this effect leads to spin accumulation near the flanks of the strip, as well as to a correction to the longitudinal electric conductance. Both the spin accumulation and the conductance exhibit damped oscillations as a function of the strip width.

This work was supported by the Taiwan National Science Council NSC93-2112-M-009-036, NSC94-2811-M-009-010, and RFBR Grant No. 03-02-17452.

[1] G. A. Prinz, Science **282**, 1660 (1998); S. A. Wolf *et al.*, Science **294**, 1488 (2001); *Semiconductor Spintronics and Quantum Computation*, edited by D. D. Awschalom, D. Loss, and N. Samarth (Springer-Verlag, Berlin, 2002); I. Zutić, J. Fabian, and S. Das Sarma, Rev. Mod. Phys. **76**, 323 (2004).

[2] M. I. Dyakonov and V. I. Perel, Phys. Lett. **35A**, 459 (1971); J. E. Hirsch, Phys. Rev. Lett. **83**, 1834 (1999).

[3] S. Murakami, N. Nagaosa, and S.-C. Zhang, Science **301**, 1348 (2003); J. Sinova *et al.*, Phys. Rev. Lett. **92**, 126603 (2004); D. Culcer *et al.*, Phys. Rev. Lett. **93**, 046602 (2004).

[4] Y. K. Kato *et al.*, Science **306**, 1910 (2004).

[5] J. Wunderlich *et al.*, Phys. Rev. Lett. **94**, 047204 (2005).

[6] J. I. Inoue, G. E. W. Bauer, and L. W. Molenkamp, Phys. Rev. B **70**, 041303 (2004); E. I. Rashba, Phys. Rev. B **70**, 201309 (2004); O. Chalaev and D. Loss, Phys. Rev. B **71**, 245318 (2005).

[7] E. G. Mishchenko, A. V. Shytov, and B. I. Halperin, Phys. Rev. Lett. **93**, 226602 (2004).

[8] A. A. Burkov, A. S. Nunez, and A. H. MacDonald, Phys. Rev. B **70**, 155308 (2004).

[9] O. V. Dimitrova, Phys. Rev. B **71**, 245327 (2005).

[10] R. Raimondi and P. Schwab, Phys. Rev. B **71**, 033311 (2005).

[11] A. G. Mal'shukov and K. A. Chao, Phys. Rev. B **71**, 121308(R) (2005).

[12] B. A. Bernevig and S. C. Zhang, Phys. Rev. Lett. **95**, 016801 (2005); K. Nomura *et al.*, cond-mat/0506189 [Phys. Rev. B (to be published)].

[13] Yu. A. Bychkov and E. I. Rashba, J. Phys. C **17**, 6039 (1984).

[14] G. Dresselhaus, Phys. Rev. **100**, 580 (1955).

[15] The cubic Rashba interaction should not be confused with the conventional linear Rashba SOI with the wave-vector-dependent coupling constant $\alpha(k)$. In the latter case SHE $\propto \alpha(k)k/E_F \ll 1$ [9,12].

[16] V. M. Edelstein, Solid State Commun. **73**, 233 (1990); J. I. Inoue, G. E. W. Bauer, and L. W. Molenkamp, Phys. Rev. B **67**, 033104 (2003).

[17] A. A. Abrikosov, L. P. Gorkov, and I. E. Dzyaloshinskii, *Methods of Quantum Field Theory in Statistical Physics* (Dover, New York, 1975).

[18] B. L. Altshuler and A. G. Aronov, in *Electron-Electron Interactions in Disordered Systems*, edited by A. L. Efros and M. Pollak (North-Holland, Amsterdam, 1985).

[19] A. G. Mal'shukov and K. A. Chao, Phys. Rev. B **61**, R2413 (2000).

[20] A. G. Mal'shukov, K. A. Chao, and M. Willander, Phys. Rev. Lett. **76**, 3794 (1996); Phys. Scr. **T66**, 138 (1996).

[21] M. I. D'yakonov and V. I. Perel', Sov. Phys. JETP **33**, 1053 (1971) [Zh. Eksp. Teor. Fiz. **60**, 1954 (1971)].

[22] Y. K. Kato *et al.*, Appl. Phys. Lett. **87**, 022503 (2005).

[23] B. K. Nikolić *et al.*, Phys. Rev. Lett. **95**, 046601 (2005); Q. Wang, L. Sheng, and C. S. Ting, cond-mat/0505576.

Appendix F:

PHYSICAL REVIEW B **72**, 165307 (2005)

Fano resonance in transport through a mesoscopic two-lead ring

Khee-Kyun Voo and Chon Saar Chu
Department of Electrophysics, National Chiao Tung University, Hsinchu 300, Taiwan, Republic of China
(Received 15 March 2005; revised manuscript received 19 July 2005; published 4 October 2005)

The ballistic transport through a one-dimensional two-lead ring at zero magnetic field is studied. We have focused on the case in which the potential in the ring does not define closed cavities or dots. Even in the absence of well-defined quasibound states, we find Fano profiles in the transmission probability. Those Fano profiles appear at energies corresponding to the standing-wave states in the ring, but their occurrence depends sensitively on the commensurability of the system parameters. When the system parameters are commensurate, the widths of the profiles at some energies are infinitesimally small. These findings suggest that the conventional understanding of the Fano profiles as a result of the interference effect of the transition through resonant states and nonresonant continuum of states, might not account for all the Fano profiles seen in the transport measurements. Moreover, the sensitivity and tunability of the resonance with respect to the system parameters may be usable in the fabrication of electrical nanodevices.

DOI: 10.1103/PhysRevB.72.165307 PACS number(s): 73.23.Ad, 73.63.Kv

I. INTRODUCTION

The Fano resonance or profile is conventionally understood as a result of the interference between resonant and nonresonant processes. It was first observed and studied in nuclear physics[1] and atomic physics,[2] and later the effect was also observed in a wide variety of spectroscopy such as atomic photoionization,[3] optical absorption,[4] Raman scattering,[5] and also the scanning tunneling through a surface impurity atom.[6,7] As recent progress in the fabrication technology of electrical nanodevices has achieved devices of the size of the order of the various coherence lengths of the conduction electron, quantum mechanical effect and hence the Fano resonance has also been seen in mesoscopic systems. For instance, it is seen in the transport through systems which contain quantum dots[8–13] and carbon nanotubes.[14] Moreover, it is proposed that the resonance can be used in the probe of the phase coherency of the electrons in transport[15,16] and the design of mesoscopic spin filters.[17]

Most studies of the Fano resonance in the electronic transport have been along the conventional line, i.e., Fano profiles are attributed to well-defined quasibound states which are in degenerate and mixed with a continuum of states. For instance, an attractive impurity or a quantum dot (QD) is coupled to a quasi-one-dimensional (quasi-1D) transport channel,[18–20] a QD is placed on a one-dimensional (1D) or quasi-1D ring connected to two leads,[12,21–29] etc. In the case of a quasi-1D transport channel with an attractive impurity, some of the quasibound levels are degenerate, with the continuums of states due to the subbands below (e.g., see Ref. 18), and therefore an electron can either seep through the impurity level or bypass it via the band continuums. It is noted that no Fano resonance can be found in singly connected 1D systems,[18] since resonant and nonresonant processes can never coexist in transport due to the topology. In the above-mentioned cases, the problem is essentially the problem of a single impurity that is embedded into a continuum of states, which was well studied by Fano.[2] Nevertheless, similar asymmetric Fano profiles are also theoretically[30–32] and experimentally[8,9] seen in the transport in systems containing only open resonant cavities. Furthermore, in theoretical study, the width of the resonance can be sensitive to the potential in the resonant cavity and can even be tuned to approach *zero*. In those cases, the problem would not be readily understandable in the conventional scheme due to Fano.[2] By this, we mean a closed cavity or dot by a cell isolated by repulsive potential barriers or constrictions in the channels, else it is an open resonant cavity.

In order to gain understanding of the Fano profile in a transport that has unusual sharpness at no well-defined quasibound state, we explore the resonance in a 1D, but doubly connected system at zero magnetic field. The system has a topology the same as that of the frequently studied Aharonov-Bohm ring, with[12,21–28] and without[33] a QD on one of the arms, but we have focused on the case in which the potential defines only open resonant cavities in the ring. The choice of this system for our study is based on the fact that this is the simplest system that shows Fano resonance at no well-defined quasibound state, and the resonance width can also be sensitively tuned by the potential and can become infinitely sharp or collapse. It is hoped that due to the simplicity of this system more of the nature of the occurrence of the resonance beyond the conventional Fano's scheme[2] can be revealed. We have found that when the system parameters are *commensurate*, the Fano profiles at some energies can become infinitesimally sharp. We also have ventured to relate the commensurability to the constructive interference along the paths. The system parameters are, e.g., the location of the impurity potential and the arm lengths of the ring. There are also theoretical reports of the collapse of the Fano resonance[32,34,35] analogous to ours, but these reports are either on more complicated systems[32,35] or the collapsing behavior is not discussed.[34]

In Sec. II we present our formulation, and in Sec. III we present and discuss the results in several cases. We focus on systems with only repulsive and pointlike δ potentials. The idealized δ-potential model makes sense at the long-wavelength regime, and it also facilitates analytical analyses. Two aspects of the systems, open resonant cavity and commensurate system parameters, are highlighted, and the occur-

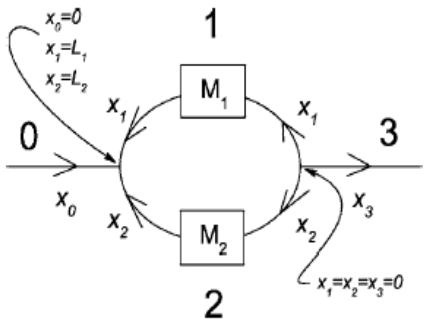

FIG. 1. The system we consider is a ring (with arms labeled by 1 and 2) connected to two leads (labeled by 0 and 3). The boxes on the ring labeled by $\mathbf{M}_{1,2}$ represent the scatterers on the arms. A coodinate system x_i is defined for the line segment labeled by i (i =0, 1, 2, and 3). While the arrows denote the positive direction of the coordinates, the right Y junction is defined at $x_1=x_2=x_3=0$, and the left Y junction is at $x_0=0$, $x_1=L_1$, and $x_2=L_2$.

rence and collapse of the Fano resonance are investigated. In the last section, Sec. IV, we give some remarks on our findings.

II. FORMULATION

We consider the ballistic transport through a two-lead ring as shown in Fig. 1. Both the ring and leads are considered as 1D, an approximation that is valid when the transverse dimension of the channel is narrow enough to allow only the lowest subband to be involved in the transport process. On each arm of the ring we include a scattering potential that is described by a transfer matrix $\mathbf{M}_i$, where $i=1,2$ labels the arm, and the wave functions on the opposite sides of a scatterer are connected by $\mathbf{M}_i$. At the three-leg junctions or Y junctions, the wave functions on the branches are connected via the Griffith's boundary condition[36] which we will describe shortly. The overall wave function can thus be found and the transmission probability be obtained.

At a given energy $E(>0)$, the wave function on each line segment in Fig. 1 can be expanded by the forward and backward traveling waves[34,37–43] as

$$\phi_i = A_i e^{ikx_i} + B_i e^{-ikx_i}, \quad i=0,1,2,\text{and } 3,$$

$$\phi_{i'} = A_i' e^{ikx_i} + B_i' e^{-ikx_i}, \quad i=1 \text{ and } 2, \tag{1}$$

where $\phi_{1',2'}$ are the wave functions before the scatterers and $\phi_{1,2}$ are after the scatterers, $k \equiv \sqrt{2mE}/\hbar$, and m is the effective mass of the traveling particle. The lengths of the arms of the ring are chosen as $L_{1,2}$ and the coordinate systems are as defined in Fig. 1. Across the scatterers, the continuity of the wave functions and their derivatives can be written as

$$\begin{bmatrix} A_1 \\ B_1 \end{bmatrix} = \mathbf{M}_1 \begin{bmatrix} A_1' \\ B_1' \end{bmatrix} \tag{2}$$

and

$$\begin{bmatrix} A_2 \\ B_2 \end{bmatrix} = \mathbf{M}_2 \begin{bmatrix} A_2' \\ B_2' \end{bmatrix}. \tag{3}$$

At the Y junctions the wave function continuity requirement[44] and Griffith's unitarity boundary condition[45] demand that the wave functions are jointed at the left Y junction by

$$A_0 + B_0 = A_1 e^{ikL_1} + B_1 e^{-ikL_1}, \tag{4}$$

$$A_0 + B_0 = A_2 e^{ikL_2} + B_2 e^{-ikL_2}, \tag{5}$$

$$(A_0 - B_0) + (A_1 e^{ikL_1} - B_1 e^{-ikL_1}) + (A_2 e^{ikL_2} - B_2 e^{-ikL_2}) = 0, \tag{6}$$

and at the right Y junction by

$$A_3 + B_3 = A_1' + B_1', \tag{7}$$

$$A_3 + B_3 = A_2' + B_2', \tag{8}$$

$$(A_3 - B_3) + (A_1' - B_1') + (A_2' - B_2') = 0. \tag{9}$$

The Griffith's boundary condition guarantees the net current flowing into a junction is zero. Since we consider particles incident from the left, we set $A_0=1$ and $B_3=0$. Equations (2)–(9) then constitute an equation set with ten linear equations and ten unknowns. It can then be solved, and the transmission probability $T=|A_3|^2$ be found. The transmission amplitude A_3 is found to be

$$A_3 = \frac{C}{D},$$

$$C \equiv e^{ikL_1}(\mathbf{M}_1^{11} - \mathbf{M}_1^{12}) + e^{-ikL_1}(\mathbf{M}_1^{21} - \mathbf{M}_1^{22}) + (L_1 \leftrightarrow L_2 \text{ and } \mathbf{M}_1 \leftrightarrow \mathbf{M}_2),$$

$$D \equiv 1 - \frac{1}{8}e^{ik(L_1+L_2)}(\mathbf{M}_1^{11}\mathbf{M}_2^{11} - 3\mathbf{M}_1^{12}\mathbf{M}_2^{12} + 2\mathbf{M}_1^{11}\mathbf{M}_2^{12}) + \frac{3}{8}e^{-ik(L_1+L_2)}(\mathbf{M}_1^{21}\mathbf{M}_2^{21} - 3\mathbf{M}_1^{22}\mathbf{M}_2^{22} + 2\mathbf{M}_1^{21}\mathbf{M}_2^{22}) + \frac{1}{4}e^{ik(L_1-L_2)}[(\mathbf{M}_1^{11} + \mathbf{M}_1^{12})(\mathbf{M}_2^{21} + \mathbf{M}_2^{22}) - 4\mathbf{M}_1^{12}\mathbf{M}_2^{22}] + (L_1 \leftrightarrow L_2 \text{ and } \mathbf{M}_1 \leftrightarrow \mathbf{M}_2), \tag{10}$$

where we have used the fact that $\det \mathbf{M}_i = 1$ (see, e.g., the discussion in Ref. 46). As the analytic expressions are cumbersome, most of the time we will proceed with our discussion by plotting out the numerical values only.

III. NUMERICAL RESULT

The behaviors of the transmission probability in some representative cases are studied in the following sections. We will focus on the dip and peak-dip profiles in the spectra, particularly, how they can occur or collapse when the system

parameters are tuned. Mathematically, we will see that the occurrence and collapse are related to the zeroes in the numerator C and denominator D in the transmission amplitude A_3 in Eq. (10). In turn, these zeroes are seen to be related to the standing-wave resonance (SWR) and two-path interference (2PI) in the arms of the ring.

A. Unequal arm lengths

In this section we investigate the case in which the arms and the leads are all at equipotential, but the arms have different lengths of L_1 and L_2. This setup is described by $\mathbf{M}_1=\mathbf{M}_2=1$ and the transmission amplitude A_3 in Eq. (10) becomes

$$A_3=\frac{i(\sin kL_1+\sin kL_2)}{1-\exp[-ik(L_1+L_2)]-\frac{1}{4}[\cos k(L_1+L_2)-\cos k(L_1-L_2)]}. \tag{11}$$

Total reflection may occur when the numerator in Eq. (11) vanishes. This requires $k(L_1-L_2)=(\text{odd integer})\times\pi$ or $k(L_1+L_2)=(\text{even integer})\times\pi$. The former equation is easily seen to correspond to a perfectly destructive 2PI between the arms. The latter equation is also easily seen to correspond to a standing wave on an isolated ring with circumference L_1+L_2. Thus it is seen that though the ring is coupled to the leads, the standing-wave states in the ring may still play a role in the transport through the ring. Note also that the SWR occurs without a red shift, in contrary to what one might expect in an open system. For a wave number k which corresponds to a perfectly destructive 2PI, the denominator in Eq. (11) is always found to be nonvanishing, and therefore there is always a total reflection under this condition. For a k in the SWR condition, the denominator in Eq. (11) vanishes if it happens that $k(L_1-L_2)=(\text{even integer})\times\pi$, which is the condition for a perfectly constructive 2PI between the two arms, and this can happen when L_2/L_1 is a rational number. When a k meets the perfectly constructive 2PI condition, the first order zeroes in the numerator and denominator in Eq. (11) cancel each other and give a nonvanishing transmission probability, which is unity. In short, when a k meets the SWR condition in the ring, a total reflection occurs when the k does not simultaneously meet a perfectly constructive 2PI condition. Otherwise, there is a perfect transmission. On the other hand, a total reflection always occurs at perfectly destructive 2PI. The above findings can be summarized into the following mathematical statements. Given a L_2/L_1, a total reflection must occur at $kL_1=(\text{odd integer})\times\pi(1-L_2/L_1)^{-1}$ (which corresponds to a perfectly destructive 2PI). A total reflection can also occur at $kL_1=2n\pi(1+L_2/L_1)^{-1}$, where n is an integer (which corresponds to a SWR in the ring), if $2n(1+L_2/L_1)^{-1}$ is not an integer. Otherwise, there is a perfect transmission. Note that $2n(1+L_2/L_1)^{-1}$ is always an integer when $L_1=L_2$ or $L_2=0$.

The above findings can be illustrated by concrete examples. Figure 2 shows the wave number dependence of the transmission probability for the case of almost equal arm lengths. It is seen that at equal arm lengths, though the transmission probability varies with the wave number, only total transmission is possible and there is no total reflection. This is because in any case there is no phase difference between the two paths and hence there is always a perfectly constructive 2PI. But at unequal arm lengths, total reflection is also seen to occur. The dips in the transmission probability[47] can be very sharp. At the limit $L_1=L_2$, the dips vanish by becoming infinitely sharp but not by recovering the transmission from zero. The spectrum does not progressively turn complicated when L_2/L_1 is detuned from 1. It becomes relatively neat when L_1 and L_2 are commensurate, i.e., when L_2/L_1 is a simple rational number and some of the resonance dips collapse. For instance, the case of $L_2/L_1\sim 2/3$ is depicted in Fig. 3. In Fig. 3 we see equally spaced sharper dips at $kL_1=2n\pi(1+L_2/L_1)^{-1}$ [provided that $2n(1+L_2/L_1)^{-1}$ is not an integer] due to the SWR in the ring. In addition, we also see equally spaced but smoother dips at $kL_1=(\text{odd integer})\times\pi(1-L_2/L_1)^{-1}$ due to the destructive 2PI. The 2PI effect has also resulted in a pronounced envelope in the transmission probability. The dips due to the SWR at $kL_1(2\pi)^{-1}\sim 3$ and 6 collapse when L_2/L_1 is exactly equal to $2/3$, i.e., when $kL_1/\pi=2n(1+L_2/L_1)^{-1}$ is exactly an integer. Interestingly, though the SWR results in transmission dips, around the dips the transmission is actually enhanced by the local minima of $|D|$ [see Fig. 2(d)]. The behaviors of the transmission probability is thus seen to be related to the interplay between the SWR and 2PI.

We have interpreted the behaviors of the numerator C and denominator D in Eq. (10) by the notions of SWR and 2PI. A closer look into the mathematical structures of them is also interesting. The very different natures of C and D can account for the abrupt occurrence and collapse of the transmission dips. Owing to the symmetry in the transfer matrices $\mathbf{M}_i^{11}=(\mathbf{M}_i^{22})^*$ and $\mathbf{M}_i^{12}=(\mathbf{M}_i^{21})^*$, $i=1,2$ (see, e.g., Ref. 46), C has always a constant phase regardless of the wave number and potential on the ring. Therefore, this phase can be peeled off and C will behave like a real-valued number; whereas D has a phase that depends on the wave number and potential, and it is genuinely a complex-valued number. Therefore, when a system parameter is slightly changed, the zeroes in C will only be slightly shifted and will remain, whereas zeroes in D can be abruptly lifted since they require both the real and imaginary parts to vanish simultaneously, which is a much more stringent condition. A nonzero transmission at delicately matched zeroes of C and D, e.g., the nonzero

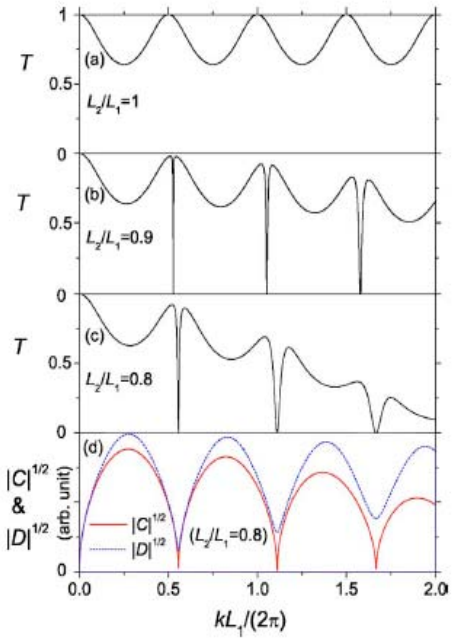

FIG. 2. (Color online) This figure shows that dips appear in the transmission probability T when L_1 and L_2 are slightly unequal. We have plotted T versus the dimensionless wave number $kL_1/(2\pi)$, for the case of no potential on the ring, and arm-length ratios L_2/L_1 =1, 0.9, and 0.8 [from (a) to (c)]. To illustrate the mathematical reason behind the formation of the transmission zeroes, the square roots of the magnitudes of the numerator C and denominator D [see Eq. (10)] of the transmission amplitude are plotted [in (d)] for the case of L_2/L_1=0.8. The zeroes in C are seen to remain but the zeroes in D (exist when $L_1=L_2$) are lifted, and hence give rise to T=0.

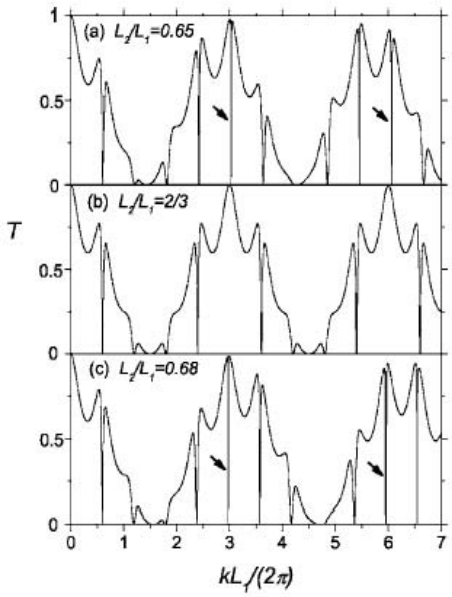

FIG. 3. For the case of no potential on the ring, the dips in the transmission probability T at some wave numbers are seen to become infinitely sharp or collapse when the arm lengths are commensurate. This figure shows T versus the dimensionless wave number $kL_1/(2\pi)$, for the case of no potential on the ring, and arm-length ratios L_2/L_1=0.65, 2/3, and 0.68 [from (a) to (c)]. The transmission dips at $kL_1/(2\pi)\sim$ 3 and 6 are seen to close at the limit L_2/L_1=2/3. Note also the transmission zeroes at $kL_1/(2\pi)$ $\sim$1.5 and 4.5, and the overall envelope due to the two-path interference.

transmission at $kL_1=n\pi$ in the case of $L_1=L_2$, is kind of "accidental." It is at a point of delicately matched SWR and perfectly constructive 2PI. It is very fragile and a slight detuning of an arm length can create a transmission zero (see Fig. 2). In later sections we will see that such behaviors of C and D are rather general and can abruptly create a Fano profile with a peak-dip pair when, e.g., the location of an impurity on the ring is shifted.

The above observation of the detuned zeroes in the numerator C and denominator D immediately implies that the numerical results can be casted into the Fano profile expression, and the dip's width can be explicitly related to the detuning from perfectly constructive 2PI. To be self-contained, we first give a very brief review of the Fano resonance. Consider a physical process which simultaneously involves a nonresonant part and a resonant part at energy ε =0. Let the nonresonant part be energy independent and described by a complex-valued amplitude t_0, and the resonant part be described by a complex-valued amplitude $t_r=za/(\varepsilon+ia)$, where z is a complex-valued number, and a is a real-valued number characterizing the width of the resonant process. The total transition amplitude $t_{tot}=t_0+t_r=t_0(\varepsilon+qa)/(\varepsilon+ia)$, where $q\equiv z/t_0+i$ is the Fano parameter, results in a total transition probability

$$T_{tot}=|t_0|^2\frac{|\varepsilon+qa|^2}{\varepsilon^2+a^2}. \tag{12}$$

Roughly speaking, in the case of $a\neq 0$ and $q\neq 0$, T_{tot} gives a dip (peak) when the numerator (denominator) in Eq. (12) is close to or equal to zero. When $a\neq 0$ and $q=0$, T_{tot} has only a dip at $\varepsilon=0$. The case of $a\neq 0$ and Im $q=0$ is discussed comprehensively in Fano's original paper.[2] In the case of $a\to 0$, the numerator and denominator in t_{tot} become exact zeroes at $\varepsilon=0$, but they are first order zeroes and cancel each other to give a finite transition probability. This is actually the case of commensurate arm lengths we have discussed. Since we know that a SWR dip can occur at $k=k_m$, where k_m is defined by $k_m(L_1+L_2)\equiv 2m\pi$, and m is an integer, we expand the transmission amplitude A_3 around a dip by letting $\delta\equiv(k-k_m)(L_1+L_2)$. Since we also know that a dip appears when $k_m(L_1-L_2)\neq 2n\pi$, where n is an integer, we define a detuning Δ from a perfectly constructive 2PI by $k_m(L_1-L_2)\equiv 2n\pi+\Delta$, where Δ is within $[-\pi,+\pi]$ (note that given an m, n is determined). Then we expand A_3 at the vicinity of a dip when both the dimensionless parameters δ and Δ are small. We have expanded Eq. (11) for the case of max($|\delta|$) $\sim|\Delta|$ and $|\Delta|\ll\pi$. We expand the numerator to the third order and the denominator to the second order, and we obtain an approximate transmission amplitude

$$A_3 \simeq (-1)^{m+n}\left[1-\frac{1}{8}\Delta^2-\frac{1}{4}\frac{L_1-L_2}{L_1+L_2}\Delta\delta-\frac{1}{6}\frac{L_1^3+L_2^3}{(L_1+L_2)^3}\delta^2\right]\frac{\delta}{\delta+i\left\{\frac{1}{8}\Delta^2+\frac{1}{4}\frac{L_1-L_2}{L_1+L_2}\Delta\delta-\frac{1}{8}\left[5-\left(\frac{L_1-L_2}{L_1+L_2}\right)^2\right]\delta^2\right\}}. \quad (13)$$

The fraction part can be roughly viewed as a $q=0$ Fano profile with a δ-dependent width, and the other part can be viewed as a slow-varying envelope function. It is seen that within this range of δ the line shape is not in the usual Fano profile. But if we further restrict the range of δ to an order of magnitude smaller than Δ, i.e., $\max(|\delta|)\sim\Delta^2$, Eq. (13) can be simplified to

$$A_3 \simeq (-1)^{m+n}\left(1-\frac{\Delta^2}{8}\right)\frac{\delta}{\delta+i\frac{\Delta^2}{8}}, \quad (14)$$

i.e., near the minimum of a dip due to a SWR, the transmission probability profile is in the form of the $q=0$ Fano profile. Note that the parameter δ is a dimensionless wave number but not energy. When the SWR approaches a perfectly constructive 2PI (i.e., Δ approaches zero), the width of the dip ($\sim\Delta^2$) approaches zero and the dip vanishes. There are a few noteworthy points here. If one adopts the conventional understanding of the Fano profile with the notions of quasibound states and their lifetimes, the "lifetimes" of the "quasibound states" in our case might seem can be dramatically tuned by a slight tuning of an arm length. Moreover, the two arms of the ring are all the same except for their lengths, the SWR at $k(L_1+L_2)=2m\pi$ also occurs in the entire ring, and there is no obvious distinction between the "resonant" and "nonresonant" transition paths in our case.

On the other hand, we also have investigated the transmission amplitude A_3 for the case of $L_1=L_2=L$, in the complex wave number $\tilde{k}$ plane. This is a common way to investigate the nature of the quasibound states on the transition paths. In this special case of $L_1=L_2=L$, we can readily find poles at $\tilde{k}L=n\pi-i\ln 3$, where n is an integer. Though the $\mathrm{Re}\,\tilde{k}$ does correspond to a standing wave in an isolated ring with circumference $2L$, the $\mathrm{Im}\,\tilde{k}$ is large and comparable to the spacing in the $\mathrm{Re}\,\tilde{k}$. This indicates that these "quasibound" states are vaguely defined and this is in congruence with the fact that the ring is strongly coupled to the leads. It is therefore inappropriate to view these states as the quasibound states in Fano's original formulation.[2] But in contrary, transmission dips are seen and can be very sharp as soon as $L_1\neq L_2$. As we will see in the later sections, these standing-wave states are also related to the formation of the peak-dip pairs in the transmission probability when an impurity potential is added. It is thus seen that the conventional Fano resonance scheme with the notions of nonresonant and resonant transition paths, and lifetimes of the quasibound states, might be hard to provide a consistent understanding basis of the above results of equal arm lengths and slightly unequal arm lengths. This reveals the following logic. Though it is true that when there are resonant and nonresonant paths in a transition process there will be a Fano profile; the converse, when there is a Fano profile there are resonant and nonresonant transition paths in the transition process, may *not* be always true. In other words, though the mathematical form of the resulting transition probabilities can be unanimously in the Fano profile form as in Eq. (12), the underlying physical contents could be quite different.

B. With impurities

This section considers the case with a presence of point impurities on the ring. An impurity is described by a Dirac-δ function potential, and this model should apply to the case in which the extensions of the potentials are small compared with the wavelengths of the incident particles and the arm lengths of the ring. We first consider the case in which an impurity is embedded into arm 1, by adding the potential $V_1\delta(x_1-X_1)$, where V_1 is the strength of the impurity potential and X_1 is the location of the impurity in coordinate x_1 on arm 1. The corresponding transfer matrix is

$$\mathbf{M}_1=\begin{bmatrix}1-\frac{imV_1}{\hbar^2k} & -e^{-i2kX_1}\frac{imV_1}{\hbar^2k}\\ e^{i2kX_1}\frac{imV_1}{\hbar^2k} & 1+\frac{imV_1}{\hbar^2k}\end{bmatrix}. \quad (15)$$

Henceforth we will use the dimensionless parameter $v_1\equiv mL_1V_1/(2\pi\hbar^2)$ to characterize the impurity strength. It is noted that the transfer matrix has the symmetry $\mathbf{M}_1^{11}=(\mathbf{M}_1^{22})^*$ and $\mathbf{M}_1^{12}=(\mathbf{M}_1^{21})^*$. Arm 2 has no potential added and hence $\mathbf{M}_2=1$. A few more words on how to relate the dimensionless impurity strength v_1 to the experiments are worthwhile. A potential with a small spatial extension a and a magnitude of $\bar{V}_1$ can be approximated by a δ potential with $V_1=a\bar{V}_1$, and hence $v_1=mL_1\bar{V}_1a/(2\pi\hbar^2)$. For instance, if we have $m=m_{\mathrm{GaAs}}\simeq 0.067\,m_{\mathrm{bare}}$, $L_1=3\ \mu$m, and $a=0.03\ \mu$m, $v_1=1$ corresponds to $\bar{V}_1\simeq 0.08$ meV.

Figure 4 shows how the asymmetric Fano profile arises when the strength of a repulsive impurity on arm 1 grows. In Fig. 4 we have chosen $L_1=L_2$ and $X_1/L_1=0.3$. The peak-dip profile is in contrast with the mere dip profile in the no-impurity case in Sec. III A, but both of them are seen to develop from zero widths. Mathematically the dips are also due to the lift of zeroes in the denominator D [see Fig. 4(d)].

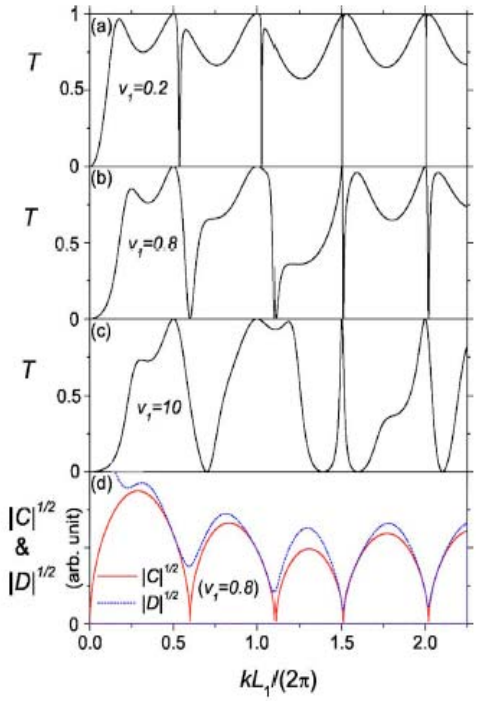

FIG. 4. (Color online) Asymmetric Fano profiles are seen in the transmission probability T when there is an impurity potential on the ring. We have plotted T versus the dimensionless wave number $kL_1/(2\pi)$ for the cases of $L_1=L_2$, an arbitrarily chosen impurity location $X_1/L_1=0.3$, and increasing potential strengths $v_1=0.2$, 0.8, and 10 (cutoff limit) [from (a) to (c)]. The Fano profiles are seen to evolve from the $v_1=0$ limit by increasing width. The square roots of the magnitudes of the numerator C and denominator D [see Eq. (10)] of the transmission amplitude are also plotted [in (d)] for the case of $v_1=0.8$ to illustrate how the Fano profiles are formed.

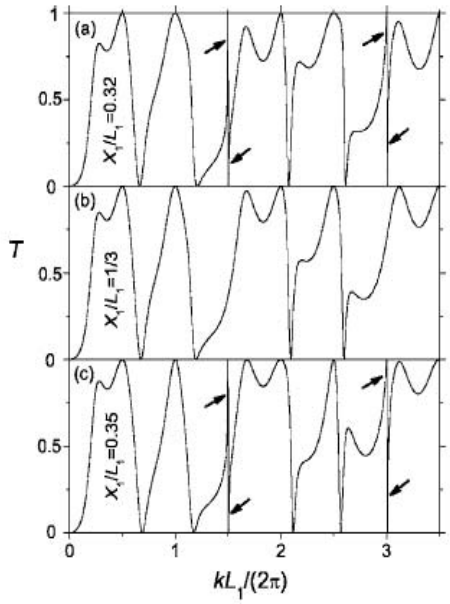

FIG. 5. Even at appreciable impurity strength, the Fano profiles in the transmission probability T at some wave numbers can collapse when the impurity is located commensurately. To illustrate this, we have plotted T versus the dimensionless wave number $kL_1/(2\pi)$ for the case of $L_1=L_2$, impurity strength $v_1=2$, and impurity locations $X_1/L_1=0.32$, 1/3, and 0.35 [from (a) to (c)]. The Fano profiles at $kL_1/(2\pi)\sim 1.5$ and 3 are seen to collapse when the impurity is located at $X_1/L_1=1/3$.

It is noted that the dips are not necessarily at the eigenenergies of an isolated ring with a point impurity, since all the locations of the impurity and Y junctions have substantial effects on the standing waves in the ring. At the strong impurity limit [Fig. 4(c)], the zero transmission dips are wide and can also be analytically found to locate at $kX_1=\text{integer}\times\pi$ or $k(L_1-X_1)=\text{integer}\times\pi$. This agrees with the result of the transport through a 1D wire with a stub.[34] An arm is essentially cut off when the impurity on it is very strong, and the arrangement of our system for Fig. 4(c) is equivalent to a 1D wire with two stubs of lengths X_1 and L_1-X_1. There will be zero transmission when the length of any one of the stubs just matches an integral number of half-wavelengths.

Similar to the collapse of the dip profile in Sec. III A, the peak-dip profile here can also collapse. In Fig. 5 we have illustrated the phenomenon by showing the transmission probability for the case in which the impurity is on a special location on an arm. We have chosen $L_1=L_2$ and $X_1/L_1\sim 1/3$, and the resonant profiles at $kL_1/(2\pi)=1.5$ and 3 are seen to collapse when $X_1/L_1=1/3$. Though the formidable expressions of C and D forbid a detailed analytical analysis, it can be readily verified that at a k that simultaneously satisfies $kL_1=n_1\pi$, $kL_2=n_2\pi$, $kX_1=n_1'\pi$, where n_1, n_2, and n_1' are integers, and n_1+n_2 is even [i.e., $k(L_1+L_2)=\text{integer}\times 2\pi$], both C and D vanish but they give a nonzero transmission amplitude $A_3=C/D=(-1)^{n_1}[1+imV_1/(\hbar^2k)]^{-1}$. The above situation can arise when X_1/L_1 and L_2/L_1 are simple rational numbers. At such a mathematically "accidental" nonzero transmission, it is expected that a slight detuning of X_1 can generate a transmission zero such as in those cases discussed in Sec. III A. Note that the above-mentioned conditions for k imply that $k(L_1-L_2)=\text{integer}\times 2\pi$. Thus these conditions are seen to be similar to those in Sec. III A, and as we will see, the conditions for the collapse of the profiles in the two impurity case is also similar.

We can also obtain an approximate analytical expression for the transmission amplitude at the vicinity of a peak-dip profile when the impurity is at a location such that the profile is very sharp and about to collapse. The relationship between the resonance width and the detuning of the impurity location will then be more explicit. In our previous discussion, we have seen that if the ratios L_2/L_1 and X_1/L_1 are rational, the peak-dip profile at the wave number k_0 has a zero width, where k_0 is defined by $k_0L_1=n_1\pi$, $k_0L_2=n_2\pi$, n_1+n_2 is even, and $k_0X_1=n_1'\pi$. We therefore can make an expansion around k_0 for the case of a small detuning of the impurity location and the resonance has a very small width. As before, we let $k_0L_1=n_1\pi$, $k_0L_2=n_2\pi$, and n_1+n_2 is even, but now we let $k_0X_1=n_1'\pi+\Delta$. Defining a dimensionless wave number $\delta\equiv(k-k_0)(L_1+L_2)$, considering the regime of $\max(|\delta|)\sim\Delta^2$

and $|\Delta| \ll \pi$, and also assumming that $\tilde{v}_1 \equiv v_1/[(n_1+n_2)\pi]$ is at most of the order of 1, we can expand the numerator C and denominator D to obtain an approximate transmission amplitude A_3. To the lowest nonvanishing order,

$$A_3 \simeq \frac{(-1)^{n_1}}{1+i\tilde{v}_1} \frac{\delta - 2\tilde{v}_1\Delta^2}{\left[\delta - \dfrac{2\tilde{v}_1\Delta^2}{1+\tilde{v}_1^2}\right] + i\dfrac{2\tilde{v}_1^2\Delta^2}{1+\tilde{v}_1^2}}. \tag{16}$$

The zero of the numerator is seen to occur at $\delta = 2\tilde{v}_1\Delta^2$, while the zero of the real part of the denominator is seen to occur at $\delta = 2\tilde{v}_1\Delta^2/(1+\tilde{v}_1^2)$. The locations of the two zeroes do not coincide as long as $\tilde{v}_1$ and Δ are nonzero, and such situation of detuned zero locations corresponds to the case of a nonzero Fano parameter q. Since $(1+\tilde{v}_1^2) > 1$, when $\tilde{v}_1 > 0$ (the impurity is repulsive), the peak appears to precede the dip; if $\tilde{v}_1 < 0$ (the impurity is attractive), the order of appearance of the peak and dip is swapped. This property is probably usable in the design of mesoscopic spin filters. For instance, if the impurity potential is spin dependent, e.g., it is provided by a magnetic impurity or magnetic scanning tunneling microscopic tip, the transmission dip of the spin up (down) electrons may coincide with the transmission peak of the spin down (up) electrons. Therefore, at this incident energy, the device is a spin filter. The overall width of the resonance depends neither on the sign of the impurity potential ($\tilde{v}_1$) nor the detuning (Δ).

What we have learnt up to now is that the existence of SWR in the ring provides only the possibility of dip or peak-dip resonance in the transmission. Eventually, whether the resonance will occur or not is contingent on the commensurability of the system parameters. In the case of commensurate system parameters, some would-be dips which meet the condition of perfectly constructive 2PI will have infinitely small widths, and the resonances are removed. In contrast, the conventional Fano resonance[2] and Breit-Wigner (BW)[48] resonance are robust against slight tuning of the system parameters.

The case of two impurities on the ring resembles very much the cases of no impurity and one impurity. The Fano profile also collapses when it meets the perfectly constructive 2PI condition. We will consider the case of each arm with one impurity embedded. The impurity scatterings are described by $\mathbf{M}_1$ and $\mathbf{M}_2$, where $\mathbf{M}_1$ is the same as that in Eq. (15), and $\mathbf{M}_2$ is obtained from $\mathbf{M}_1$ by the substitution $X_1 \to X_2$ and $V_1 \to V_2$. $V_i (i=1,2)$ is the strength of an impurity, and X_i is the location of an impurity in the coordinate x_i on arm i. In such an arrangement, the two leads are always separated by the impurities. When both impurities are away from the Y junctions, the potential defines an open resonant cavity in the ring but not a closed dot. We will use the dimensionless parameter $v_i \equiv mL_1V_i(2\pi\hbar^2)^{-1}$ to characterize the strengths of the impurity potentials (note that we have used L_1 in the definitions of both v_1 and v_2).

Figure 6 shows the transmission probability for the cases of symmetric and asymmetric potentials on the arms. For a symmetric arrangement of the arms, i.e., $v_1 = v_2$, $X_1 = X_2$, and $L_1 = L_2$, only broad structures are seen. But when the potentials on the arms are asymmetric, e.g., either $X_1 \neq X_2$ or $v_1 \neq v_2$, Fano profiles are seen. The almost-perfect transmission peaks in the Fano profiles at low energies are rather surprising since the two leads are separated by the δ potentials on both arms. In a 1D system, there is no perfect transmission through a single δ-potential barrier at finite energy, whereas perfect transmission through a double δ-potential barrier at finite energy is possible, since the barriers create quasibound states in between them and BW resonant tunneling can take place. In our cases for Fig. 6, no region between the leads is enclosed by the repulsive potentials and therefore one usually does not expect any perfect transmission at finite energy. It is thus seen that the doubly connected 1D system behaves differently from the singly connected 1D system. The fact that the Fano profile appears only at asymmetric potentials on the arms indicates that the profiles are intimately related to the constructive 2PI between the arms. This is similar to the case in which $L_1 \simeq L_2$ but no potential is added onto the arms studied in Fig. 2.

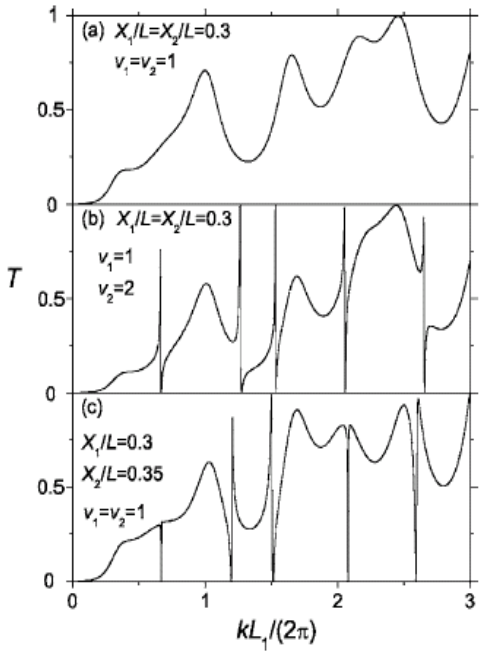

FIG. 6. Fano profiles are seen in the transmission probability T when the symmetricity of the two arms are disturbed. To illustrate this, we have plotted T versus the dimensionless wave number $kL_1/(2\pi)$ for the case of $L_1 = L_2 \equiv L$, and two impurities with strengths $v_{1,2}$ at $X_{1,2}$. The case of symmetric arms are illustrated by (a) $X_1/L = X_2/L = 0.3$ and $v_1 = v_2 = 1$; whereas the case of asymmetric impurity strengths are illustrated by (b) $X_1/L = X_2/L = 0.3$, $v_1 = 1$, and $v_2 = 2$; and the case of asymmetric impurity locations are illustrated by (c) $v_1 = v_2 = 1$, $X_1/L = 0.3$, and $X_2/L = 0.35$.

The collapse of the Fano profile also occurs in other cases, particularly in cases where the system parameters are commensurate. Figure 7 illustrates the collapse at a particular wave number using a system with $L_2/L_1 = 2/3$, $X_1/L_1 = 1/3$, and $X_2/L_2 \sim 1/2$. To work out rigorously all the wave numbers at which the collapse can occur would be difficult due to the complexity of C and D [see Eq. (10)], but an ansatz

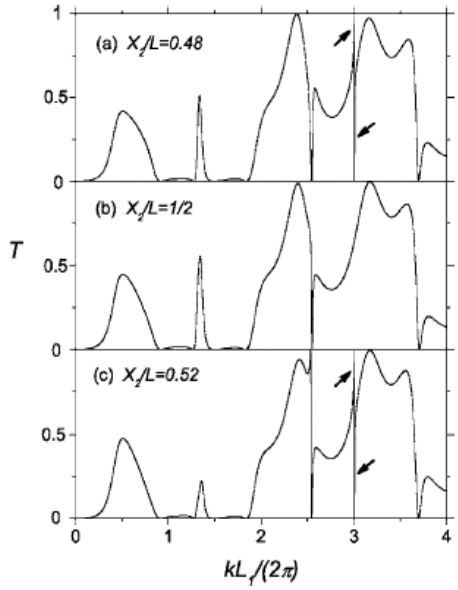

FIG. 7. Collapse of the Fano profile can also occur at more complicated system arrangements, as long as the system parameters are commensurate. For instance, we have plotted the transmission probability T versus the dimensionless wave number $kL_1/(2\pi)$ for the case in which $L_2/L_1=2/3$ and an impurity is placed on each arm. The strengths of the impurities on arms 1 and 2 are arbitrarily chosen as $v_1=1$ and $v_2=1.3$ respectively. The location of the impurity on arm 1 is chosen as $X_1/L_1=1/3$, while the location of the impurity on arm 2 is chosen as $X_2/L_2=0.48$, 1/2, and 0.52 [from (a) to (c)]. We note that the Fano profile at $kL_1/(2\pi)\sim 3$ collapses at approaching the commensurate location $X_2/L_2=1/2$.

similar to that in Sec. III B is seen to work well. It can be verified by direct substitution that at a k which simultaneously meets the conditions $kL_i=n_i\pi$, $kX_i=n_i'\pi$, where n_i and n_i' are integers $(i=1,2)$, and n_1+n_2 is even [i.e., $k(L_1+L_2)=(\text{even integer})\times\pi$], both C and D vanish, but the transmission amplitude $A_3=C/D=(-1)^{n_1}[1+im(V_1+V_2)/(\hbar^2k)]^{-1}$ is nonzero. Due to this mathematical structure, a zero transmission is anticipated at this k when any one of the system parameters, the impurity locations or arm lengths, is detuned. An illustration of the above mathematics is given in Fig. 7, and the resonance is seen to be a peak-dip pair. Since the above conditions for k also imply $k(L_1-L_2)=\text{integer}\times 2\pi$, which is a perfectly constructive 2PI, this again suggests that the phenomenon is related to the SWR and 2PI on the arms.

IV. CONCLUDING REMARKS

We have studied in this paper the ballistic transport through a 1D ring in the regime of a comparable particle's wavelength and a ring's dimension. In all cases, repulsive δ potentials are used, and no two δ potentials are placed on the same arm so that they do not create quasibound states. Nevertheless, a Fano profile can still be found and is shown to be related to the standing-wave states in the ring. The Fano profiles encountered in this paper grow or collapse by changing their widths, but not by changing their dips' depths or peaks' heights. We also have checked the case of attractive impurity potentials, and we have found that the results are qualitatively the same.[49]

In our study, several aspects of the Fano resonance are examined. Firstly, well-defined quasibound states which are weakly coupled to a continuum of states may not be necessary for the observation of the resonance. In other words, though the simultaneous presence of resonant and nonresonant processes in a physical process results in a Fano profile,[2] it might not be true to say that the observation of a Fano profile always implies the simultaneous presence of resonant and nonresonant processes in the underlying mechanism. Moreover, in our study the resonances are identified as the standing waves on the entire ring but not on only one of the arms (paths). Hence there is no clear distinction between the "resonant" and "nonresonant" paths. Secondly, commensurability is an important factor in the occurrence of the Fano profile. When the system parameters are commensurate, the Fano profiles at some energies can disappear by collapsing their widths to zero. Hence the presence of standing-wave resonance in the ring does not guarantee the occurrence of the Fano profile. Since the commensurability is found to be related to the constructive 2PI between the two arms, the width of the profile is seen to be controlled by the 2PI. While collapse of the Fano profile is also seen in the theoretical investigations of more complicated systems,[32,35] in the study of our exceedingly simple system, the collapse can be further seen as a result of the constructive 2PI. The abrupt occurence or collapse of the profile also indicates that the problem might not be equivalent to the conventional one discussed by Fano,[2] since a slight change in the system should not create or remove any quasibound states, or change their lifetimes dramatically. In our case, the prominent behaviors of the transmission probability are seen to be related to the SWR and 2PI. How the understanding of this simple system can be related or extended to the case of more complicated systems will be an interesting subject.

The sensitivity of the Fano profile to the device geometry and spatial details of the potential may imply that a naive tight-binding formulation of the quantum coherent device is not always viable. For instance, if a potential barrier is simply modeled by a hopping integral, or a resonance state is simply modeled by a zero-dimensional state, the spatial information of the device will be lost, and the consequences of the commensurability of the system parameters will be gone. We point out that such sensitivity of the resonance might be useful in the design of mesoscopic electrical switches, with the impurity potential provided by, e.g., a movable scanning tunneling microscopic tip.

We have left out some issues. For instance, the finite width of the transport channel has not been considered. We believe the Fano profile will be still present (e.g., see a related study in Ref. 50), and the question is just how it will be reshaped. Another issue is how the Fano profile will be affected by the inelastic dephasing process along the transport channel. These issues will be deferred to a later project.

ACKNOWLEDGMENTS

This work is supported by the NSC of Taiwan under Grant No. 93-2811-M-009-029. We thank C.-S. Tang and L.-Y. Wang for useful discussions, and the National Center for Theoretical Sciences (Physics Division) of Taiwan for letting us to use their facilities.

[1] R. K. Adair, C. K. Bockelman, and R. E. Peterson, Phys. Rev. **76**, 308 (1949).

[2] U. Fano, Phys. Rev. **124**, 1866 (1961).

[3] U. Fano and A. R. P. Rau, *Atomic Collision and Spectra* (Academic Press, Orlando, 1986).

[4] J. Faist, F. Capasso, C. Sirtori, K. W. West, and L. N. Pfeiffer, Nature (London) **390**, 589 (1997).

[5] F. Cerdeira, T. A. Fjeldly, and M. Cardona, Phys. Rev. B **8**, 4734 (1973).

[6] V. Madhavan, W. Chen, T. Jamneala, M. F. Crommie, and N. S. Wingreen, Science **280**, 567 (1998).

[7] J. Li, W.-D. Schneider, R. Berndt, and B. Delley, Phys. Rev. Lett. **80**, 2893 (1998).

[8] J. Gores, D. Goldhaber-Gordon, S. Heemeyer, M. A. Kastner, H. Shtrikman, D. Mahalu, and Y. Meirav, Phys. Rev. B **62**, 2188 (2000).

[9] I. G. Zacharia, D. Goldhaber-Gordon, G. Granger, M. A. Kastner, Y. B. Khavin, H. Shtrikman, D. Mahalu, and U. Meirav, Phys. Rev. B **64**, 155311 (2001).

[10] K. Kobayashi, H. Aikawa, S. Katsumoto, and Y. Iye, Phys. Rev. Lett. **88**, 256806 (2002).

[11] C. Fuhner, U. F. Keyser, R. J. Haug, D. Reuter, and A. D. Wieck, cond-mat/0307590 (unpublished).

[12] K. Kobayashi, H. Aikawa, A. Sano, S. Katsumoto, and Y. Iye, Phys. Rev. B **70**, 035319 (2004).

[13] M. Sato, H. Aikawa, K. Kobayashi, S. Katsumoto, and Y. Iye, cond-mat/0410062 (unpublished).

[14] J. Kim, J.-R. Kim, Jeong-O. Lee, J. W. Park, H. M. So, N. Kim, K. Kang, K.-H. Yoo, and J.-J. Kim, Phys. Rev. Lett. **90**, 166403 (2003).

[15] A. A. Clerk, X. Waintal, and P. W. Brouwer, Phys. Rev. Lett. **86**, 4636 (2001).

[16] Y.-J. Xiong and S.-J. Xiong, Int. J. Mod. Phys. B **16**, 1479 (2002).

[17] J. F. Song, Y. Ochiai, and J. P. Bird, Appl. Phys. Lett. **82**, 4561 (2003).

[18] E. Tekman and P. F. Bagwell, Phys. Rev. B **48**, 2553 (1993).

[19] J. U. Nockel and A. D. Stone, Phys. Rev. B **50**, 17415 (1994).

[20] A. C. Johnson, C. M. Marcus, M. P. Hanson, and A. C. Gossard, Phys. Rev. Lett. **93**, 106803 (2004).

[21] A. Yacoby, M. Heiblum, D. Mahalu, and H. Shtrikman, Phys. Rev. Lett. **74**, 4047 (1995).

[22] A. L. Yeyati and M. Buttiker, Phys. Rev. B **52**, R14360 (1995).

[23] G. Hackenbroich and H. A. Weidenmuller, Phys. Rev. Lett. **76**, 110 (1996).

[24] J. Wu, B.-L. Gu, H. Chen, W. Duan, and Y. Kawazoe, Phys. Rev. Lett. **80**, 1952 (1998).

[25] O. Entin-Wohlman, A. Aharony, Y. Imry, and Y. Levinson, cond-mat/0109328 (unpublished).

[26] K. Kobayashi, H. Aikawa, S. Katsumoto, and Y. Iye, Phys. Rev. B **68**, 235304 (2003).

[27] C. Benjamin and A. M. Jayannavar, Phys. Rev. B **68**, 085325 (2003).

[28] H. Aikawa, K. Kobayashi, A. Sano, S. Katsumoto, and Y. Iye, Phys. Rev. Lett. **92**, 176802 (2004).

[29] P. Singha Deo, Solid State Commun. **107**, 69 (1998).

[30] M. Mendoza and P. A. Schulz, Phys. Rev. B **68**, 205302 (2003).

[31] Y. Takagaki and K. H. Ploog, Phys. Rev. B **70**, 073304 (2004).

[32] V. A. Margulis and M. A. Pyataev, J. Phys.: Condens. Matter **16**, 4315 (2004).

[33] Y. Gefen, Y. Imry, and M. Ya. Azbel, Phys. Rev. Lett. **52**, 129 (1984).

[34] J.-B. Xia, Phys. Rev. B **45**, 3593 (1992).

[35] C. S. Kim, A. M. Satanin, Y. S. Joe, and R. M. Cosby, Phys. Rev. B **60**, 10962 (1999).

[36] J. Stanley Griffith, Trans. Faraday Soc. **49**, 345 (1953); **49**, 650 (1953).

[37] M. Buttiker, Y. Imry, and M. Ya. Azbel, Phys. Rev. A **30**, 1982 (1984).

[38] J. M. Mao, Y. Huang, and J. M. Zhou, J. Appl. Phys. **73**, 1853 (1993).

[39] M. V. Moskalets, Low Temp. Phys. **23**, 824 (1997).

[40] C.-M. Ryu and S. Y. Cho, Phys. Rev. B **58**, 3572 (1998).

[41] B. Molnar, F. M. Peeters, and P. Vasilopoulos, Phys. Rev. B **69**, 155335 (2004).

[42] B. Molnar, P. Vasilopoulos, and F. M. Peeters, cond-mat/0407536 (unpublished).

[43] D. Frustaglia and K. Richter, Phys. Rev. B **69**, 235310 (2004).

[44] The wave function continuity requirement demands $\phi_0=\phi_1=\phi_2$ at the left Y junction and $\phi_{1'}=\phi_{2'}=\phi_3$ at the right Y junction in Fig. 1.

[45] The Griffith's boundary condition states that at an n-leg junction, the sum of the spatial derivatives of the wave functions on the legs is zero, i.e., $\Sigma_i(\partial\phi_i/\partial x_i)=0$, where the directions of the coordinates are defined either simultaneously toward the junction or outward.

[46] G. Grosso and G. P. Parravicini, *Solid State Physics* (Academic Press, New York, 2000), p. 8.

[47] Such dips at unequal arm lengths were reported in Ref. 34, but no further discussion was made.

[48] G. Breit and E. Wigner, Phys. Rev. **49**, 519 (1936).

[49] K.-K. Voo and C. S. Chu (unpublished).

[50] A. A. Kiselev and K. W. Kim, J. Appl. Phys. **94**, 4001 (2003).

Appendix G:

PHYSICAL REVIEW B **73**, 035307 (2006)

Connecting wave functions at a three-leg junction of one-dimensional channels

Khee-Kyun Voo,[1,*] Shu-Chuan Chen,[1] Chi-Shung Tang,[2] and Chon-Saar Chu[1]
[1]*Department of Electrophysics, National Chiao Tung University, Hsinchu 30010, Taiwan, Republic of China*
[2]*Physics Division, National Center for Theoretical Sciences, Hsinchu 30013, Taiwan, Republic of China*
(Received 21 September 2005; revised manuscript received 31 October 2005; published 10 January 2006)

We propose a scheme to connect the wave functions on different one-dimensional branches of a three-leg junction (*Y* junction). Our scheme differs from that due to Griffith [Trans. Faraday Soc. **49**, 345 (1953)] in the respect that ours can model the difference in the widths of the quasi-one-dimensional channels in different systems. We test our scheme by comparing results from a doubly connected one-dimensional system and a related quasi-one-dimensional system, and we find a good agreement. Therefore our scheme may be useful in the construction of one-dimensional effective models out of (multiply connected) quasi-one-dimensional systems.

DOI: 10.1103/PhysRevB.73.035307 PACS number(s): 73.23.Ad, 73.63.Nm, 73.21.Hb, 02.10.Ox

I. INTRODUCTION

For a system which comprises quasi-one-dimensional (Q1D) channels, when only the low-energy regime at near the first subband bottom is considered, it can usually be modeled by a one-dimensional (1D) system. When the system is multiply connected and consists of multileg junctions, the wave functions on the branches are usually connected at the junctions by the Griffith scheme,[1–4] the Shapiro scheme,[5–7] or similar schemes. Since such formulations greatly reduce the calculational effort of complicated multiply connected mesoscopic systems, they have been used widely in the literature. For example, see Refs. 8–19 and the references therein. However, arguments which lead to these connecting schemes are kinematical,[1–7] and it is not clear what kind of junction in practice they describe. Moreover, a comparison between the results of these schemes and that of the exact calculation of Q1D systems has never been done. It is the purpose of this paper to make a comparison between the Griffith result, the Q1D result, and the result due to a scheme we propose in this paper. We find that for clean junctions of Q1D channels, the Griffith result is not even qualitatively in accord with the exact result. The scheme we derive gives a result that compares much better with the exact result.

At a *N*-leg junction of 1D channels, the wave function continuity condition is a requirement that must be respected. Besides, the Griffith scheme[1–4] demands that the sum of the derivatives of the wave functions on the different branches at the junction is zero, i.e.,

$$\sum_{i=1}^{N} \frac{\partial \psi_i}{\partial x_i} = 0, \tag{1}$$

where the directions of the coordinates are defined either diverging from or converging to the junction. This is the simplest way to impose the unitarity condition of no net current flows into the junction, i.e., $\Sigma_i \mathrm{Re}\, \psi_i^*(-i\partial\psi_i/\partial x_i)=0$. When there is a magnetic field, the requirement is rephrased as the sum of the covariant derivatives is zero, i.e., $\Sigma_i(\partial/\partial x_i - ieA_i^{\parallel})\psi_i=0$, where $A_i^{\parallel}$ is the component of the vector potential parallel to branch i at the junction. On the other hand, the Shapiro scheme[5–7] directly demands that the scattering matrix connecting the in-going and out-going waves at the junction be unitary, and a general matrix with free parameters is written down. When the spin degree of freedom is considered, these schemes are straightforwardly applied to each spin channel.[15–19] These schemes and the like have been taken for granted and used widely in the literature.

II. FORMULATIONS AND MODELS

We approach the problem from another point of view. For a Q1D system with equal-width channels (the "width" is an ill-defined quantity in snaking channels but nevertheless we may talk about it when the curvatures are small enough), we may approximate a three-leg junction (*Y* junction) and its branches [e.g., see Fig. 1(a)] by a tight-binding (TB) model as shown in Fig. 1(b).[20]

The tight-binding model is described by a second quantized Hamiltonian

$$H = \sum_{\mathbf{i},\mathbf{j}} c_{\mathbf{i}}^{\dagger} h_{\mathbf{ij}} c_{\mathbf{j}}, \tag{2}$$

where $c_{\mathbf{i}}$ is the annihilation operator of a spinless particle on site $\mathbf{i}$, and $h_{\mathbf{ij}}$ is a matrix element which is complex in gen-

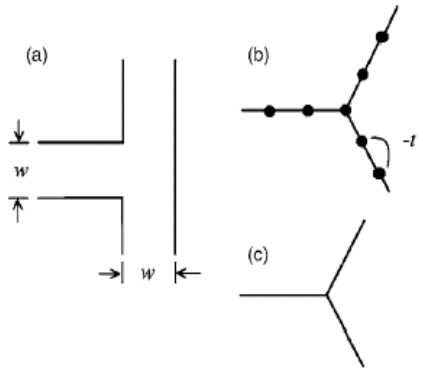

FIG. 1. (a) The original *Y* junction of Q1D channels considered in this paper, (b) the reformulated *Y* junction of tight-binding channels, and (c) the effective *Y* junction of 1D channels affiliated with the Griffith or our connection scheme.

eral. The element h_{ij} is called a hopping when $\mathbf{i} \neq \mathbf{j}$, and an onsite potential when $\mathbf{i}=\mathbf{j}$. Defining a basis set $\{|\mathbf{i}\rangle\}$ by $|\mathbf{i}\rangle \equiv c_{\mathbf{i}}^{\dagger}|0\rangle$, where $|0\rangle$ is the no-particle state, one can write the time-independent Schrödinger equation $H|\psi\rangle = E|\psi\rangle$, where E is the energy of the particle, into the form

$$\sum_{\mathbf{j}} (h_{\mathbf{ij}} - E\delta_{\mathbf{ij}})\bar{\psi}_{\mathbf{j}} = 0, \tag{3}$$

where $\bar{\psi}_{\mathbf{j}} \equiv \langle \mathbf{j}|\psi\rangle$ is the TB wave function at site $\mathbf{j}$. We define that the hopping exists only between nearest-neighbor sites, and is denoted by $-t$. The onsite potential at site $\mathbf{i}$ is denoted by $V_{\mathbf{i}}+2t$.

The magnitude of the hopping $-t$ is obtained by the following argument. Let a Q1D channel be approximated by a finite-difference square grid, with three grid-points across the channel, one at the center and each edge. Then the distance between the grid-points will be $w/2$, where w is the width of the channel, and the hopping in the finite-difference time-independent Schrödinger equation[21] will be $-t=-2\hbar^2/(mw^2)$. We will assume the same hopping in our TB formulation.

Away from the junction, the TB time-independent Schrödinger equation reads[21]

$$-t(\bar{\psi}_{\mathbf{i+1}} - \bar{\psi}_{\mathbf{i}}) + t(\bar{\psi}_{\mathbf{i}} - \bar{\psi}_{\mathbf{i-1}}) + (V_{\mathbf{i}} - E)\bar{\psi}_{\mathbf{i}} = 0, \tag{4}$$

where E is the energy. In the long-wavelength limit it reduces, as it should, to the 1D second order differential time-independent Schrödinger equation, $-[\hbar^2/(2m)]\partial_x^2\psi(x) + [V(x)-E]\psi(x)=0$.

At a Y junction, the TB time-independent Schrödinger equation reads

$$(\bar{\psi}_1 - \bar{\psi}_0) + (\bar{\psi}_2 - \bar{\psi}_0) + (\bar{\psi}_3 - \bar{\psi}_0) + \frac{E - V_0 + t}{t}\bar{\psi}_0 = 0, \tag{5}$$

where the subscript "0" denotes the site at the junction, and "1," "2," and "3" denote the sites on the branches nearest to the site at the junction [i.e., in Eq. (3), take $\mathbf{i}=0$, and $\mathbf{j}=0$, 1, 2, and 3]. It is seen that the Griffith scheme formulated in Eq. (1) is recovered only when $E-V_0+t=0$ at the junction. It is reasonable to set $E=0$ here since we are considering energies at near the band bottom and $E \ll t$. But one still requires $V_0 = t$ to send the last term in Eq. (5) to zero. In other words, the Griffith connection scheme[1–4] actually describes a Y junction of Q1D channels with a *repulsive* potential with a strength of the order of t, whereas in this paper we propose a connection scheme in the long-wavelength limit for a *clean* Y junction [i.e., $V_0=0$ in Eq. (5)] of Q1D channels. At a Y junction of 1D channels [see Fig. 1(c)], we propose

$$\sum_{i=1}^{3} \frac{\partial \psi_i}{\partial x_i} + \frac{2\nu}{w}\psi_1 = 0, \tag{6}$$

where the directions of the coordinates are defined to be diverging from the junction. If Eq. (6) is reached by dividing Eq. (5) by $w/2$ and letting $w \to 0$ (remember that E/t and V_0/t have been set to zero), the factor ν will be equal to 1. Adopting $\nu=1$ indeed results in a good enough qualitative comparison with the Q1D result. But we will see that choosing $\nu \simeq 1.9$ may bring the 1D and Q1D results to a semiquantitative agreement, which means that the term has been underestimated. The TB argument serves to bring out the $1/w$ dependence of the term, and the fixing of ν will be discussed using concrete examples. The effect of the channel width is hence included, in contrast to the Griffith scheme (the case of $\nu=0$). The $1/w$ dependence results in an effect that is more prominent at smaller channel widths, and this understanding may also help to relate studies on the quantum graph theory[4,7] to the practical experiments. The case of a general N-leg junction can also be worked out likewise.

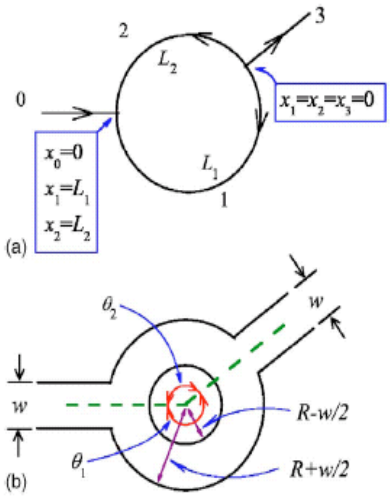

FIG. 2. (Color online) The doubly connected 1D system and the related Q1D system we consider. (a) The 1D system is a ring (with arms labeled by 1 and 2) connected to two leads (labeled by 0 and 3). The coodinate system x_i is defined for the line segment labeled by i (i=0, 1, 2, and 3). The arrows denote the positive directions of the coordinates, the right Y junction is defined at $x_1=x_2=x_3=0$, and the left Y junction at $x_0=0$, $x_1=L_1$, and $x_2=L_2$. (b) The Q1D system is an annulus with two radially connected leads. Both the annulus and the leads have the same width.

In this paper we compare the Griffith and our schemes with the exact Q1D calculation in a chosen type of system. We calculate the transmission probability for a 1D ring connected to two leads [see Fig. 2(a)], which is the simplest multiply connected 1D system, using the Griffith and our connection schemes at the Y junctions. In addition, we also calculate the transmission probability for a similar system, an annulus connected to two Q1D leads [see Fig. 2(b)], using the exact mode-matching method. The two three-leg junctions in Fig. 2(b) resemble the one in Fig. 1(a). Note that the transmission probability is directly related to the experimentally measurable conductance.[21] We will sketch how we have done the calculations, and we refer the readers to the literature for more details.

In a 1D model as shown in Fig. 2(a), the wave function on each line segment at a given positive energy E is a superposition of forward and backward traveling waves, i.e.,

$$\psi_i(x_i) = A_i e^{ikx_i} + B_i e^{-ikx_i}, \quad i=0,\ 1,\ 2,\ \text{and}\ 3, \tag{7}$$

where $k \equiv \sqrt{2mE}/\hbar$ and m is the effective mass of the particle. The wavelength λ is given by $\lambda \equiv 2\pi/k$. The $x_{0,1,2,3}$ are

the coordinates on the line segments correspondingly, and the coordinates have positive directions as that defined in Fig. 2. We define $x_1=x_2=x_3=0$ at the right junction, and $x_0=0$, $x_1=L_1$, $x_2=L_2$ at the left junction, where $L_{1,2}$ are the lengths of the arms between the junctions [see Fig. 2(a)]. The A_i (B_i) is the coefficient of a forward (backward) traveling wave. Since we consider particles incident from the left, we set $A_0=1$ and $B_3=0$. Then the continuity requirement

$$\psi_0\big|_{x_0=0}=\psi_1\big|_{x_1=L_1}=\psi_2\big|_{x_2=L_2} \tag{8}$$

and

$$\psi_1\big|_{x_1=0}=\psi_2\big|_{x_2=0}=\psi_3\big|_{x_3=0}, \tag{9}$$

and the Griffith unitarity imposition [following Eq. (1)]

$$\left.\frac{\partial\psi_0}{\partial x_0}\right|_{x_0=0}+\left.\frac{\partial\psi_1}{\partial x_1}\right|_{x_1=L_1}+\left.\frac{\partial\psi_2}{\partial x_2}\right|_{x_2=L_2}=0 \tag{10}$$

and

$$\left.\frac{\partial\psi_1}{\partial x_1}\right|_{x_1=0}+\left.\frac{\partial\psi_2}{\partial x_2}\right|_{x_2=0}+\left.\frac{\partial\psi_3}{\partial x_3}\right|_{x_3=0}=0 \tag{11}$$

constitute an equation set which contains six equations with the six unknowns $\{B_0;A_1,B_1;A_2,B_2;A_3\}$ which have been defined in Eq. (7). Hence the transmission amplitude A_3 can be solved, and the transmission probability $T=|A_3|^2$ be found. We may also replace the Griffith unitarity condition by our unitarity condition [following Eq. (6)]

$$\left.\frac{\partial\psi_0}{\partial x_0}\right|_{x_0=0}+\left.\frac{\partial\psi_1}{\partial x_1}\right|_{x_1=L_1}+\left.\frac{\partial\psi_2}{\partial x_2}\right|_{x_2=L_2}+\left.\frac{2\nu}{w}\psi_0\right|_{x_0=0}=0 \tag{12}$$

and

$$\left.\frac{\partial\psi_1}{\partial x_1}\right|_{x_1=0}+\left.\frac{\partial\psi_2}{\partial x_2}\right|_{x_2=0}+\left.\frac{\partial\psi_3}{\partial x_3}\right|_{x_3=0}+\left.\frac{2\nu}{w}\psi_3\right|_{x_3=0}=0, \tag{13}$$

and the transmission probability also can be solved. We will discuss the fixing of ν later in this paper.

Besides the mentioned 1D model, we also solve a related Q1D model in a way as that of Xia and Li in Ref. 22. Consider an annulus with an inner and an outer radii of $R-w/2$ and $R+w/2$, respectively, and two leads of width w radially connected to it as shown in Fig. 2(b). The wave function is governed by the two-dimensional (2D) differential time-independent Schrödinger equation. In a lead it can be expanded in terms of transverse modes (subbands) and longitudinal forward and backward modes, i.e., $\psi_{\text{lead}}(x,y)=\Sigma_{l=1}^{N}(a_l e^{ik_l x}+b_l e^{-ik_l x})\sin(l\pi y/w)$, where x and y are respectively the longitudinal and transverse coordinates for the lead. The k_l and l are related by $k_l^2+(l\pi/w)^2=2mE/\hbar^2$, where E is the energy (positive) of the particle, and k_l can be real or imaginary. In the annulus the wave function can be expanded by radial and angular modes, i.e., $\psi_{\text{annulus}}(r,\theta)=\Sigma_{l=-M}^{M}\phi_l(kr)e^{il\theta}$, where a radial mode is given by $\phi_l(kr)\equiv c_l J_l(kr)+d_l Y_l(kr)$, and $k=\sqrt{2mE}/\hbar$. The r and θ are the radial and angular coordinates, respectively; and the J_l and Y_l are the Bessel functions of the first and second kinds, respectively. We demand $\phi_l|_{r=R-w/2}=0$ for any θ, $\psi_{\text{annulus}}|_{r=R+w/2}=0$ when θ is away from the leads, but $\psi_{\text{annulus}}|_{r=R+w/2}=\psi_{\text{lead}}$ when θ is in the range of a lead. Also, the radial derivative $\partial\psi_{\text{annulus}}/\partial r$ is equated with the longitudinal derivative $\partial\psi_{\text{lead}}/\partial x$ when they meet at the outer arc of the annulus. The difference between the straight transverse cuts of the leads and the outer arcs of the annulus is neglected. The wave functions in the leads and the annulus are hence matched. Expanding the wave functions in different regions with sufficient numbers of modes,[23] one gets a set of equations relating the coefficients of the modes in different regions. With a given energy E and specified in-going subbands, one can obtain the transmission probabilities in the out-going subbands.

In the Q1D case, we will consider that the particle is incident from one lead, and its energy is below the second subband and hence the particle propagates only within the first subband. The resulting transmission probability is to be compared with that in the 1D case. We will use the more convenient longitudinal wave number $k_\parallel\equiv\sqrt{2m(E-E_0^{\text{ann.}})}/\hbar$ instead of the energy E, where $E_0^{\text{ann.}}$ is the energy of the nodeless ground state of the isolated annulus in an individual case.[24] Defining a longitudinal wavelength $\lambda_\parallel$ by $\lambda_\parallel\equiv 2\pi/k_\parallel$ implies that the long-wavelength limit we consider is at $\lambda_\parallel \gg w$. Here we define the arm lengths by $L_{1,2}\equiv R\theta_{1,2}$, where $\theta_{1,2}$ are the angles shown in Fig. 2(b).

III. COMPARISON BETWEEN RESULTS

Figure 3 shows the transmission probabilities obtained by different schemes, for the case of symmetrical arms in the ring ($L_1=L_2\equiv L$). We have considered broad [Fig. 3(a)] and narrow [Fig. 3(b)] channels, and in both cases we have presented the result of the Q1D calculation, the result of the Griffith scheme, and the results of our scheme (with $\nu=1$ and 1.9). The Griffith result is seen to differ very much from the Q1D result in all cases. The $\nu=1$ scheme qualitatively captures the trend of change in the Q1D result when the channel width is changed, while the $\nu=1.9$ scheme captures the Q1D result most satisfactorily.

Besides the Griffith result, it is seen that all results in Fig. 3 show Breit-Wigner (BW) resonance peaks.[25] These BW peaks become sharper and shift toward the left when the channels narrow down, i.e., $w/R\to 0$ [compare Figs. 3(a) and 3(b)]. Those peaks are due to the quasibound levels in the arms, and they are seen to be always blueshifted[26] from the exact levels. In the 1D case, the exact levels are at $2L/\lambda\equiv kL/\pi=$integer. The quasibound levels and the blueshift are results of the presence of an *attractive* potential at a Y junction.[27] While the attractive potential in our scheme is manifest [see Eq. (6)], the potential at a Y junction of Q1D channels is not so obvious, but can have an intuitive understanding as follows. Since a particle feels less confined at near a junction, the "band-bottom" at the vicinity of a junction is effectively lower, and therefore the region acts as an attraction center. This potential becomes stronger when the channels become narrower, and that leads to the sharper and

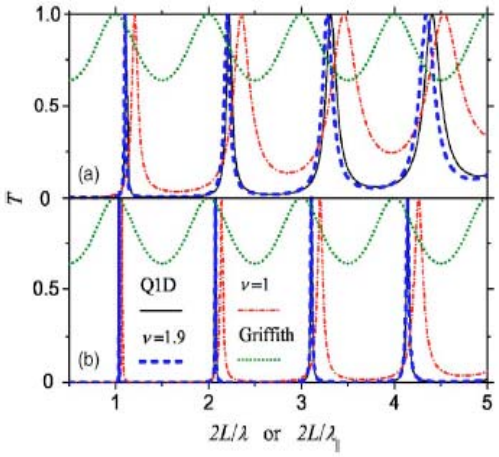

FIG. 3. (Color online) The transmission probability T is plotted versus the dimensionless longitudinal wave numbers ($2L/\lambda_{\|}$ in the case of Q1D channels, and $2L/\lambda$ in the case of 1D channels), for the case of $L_1=L_2\equiv L$. The Q1D results (solid lines), 1D results due to our scheme [dashed ($\nu=1.9$) and dash-dotted ($\nu=1$) lines], and 1D results due to the Griffith scheme (dotted lines) are shown. T is plotted for the cases of broad and narrow Q1D channels, (a) $R/w=3.5$ and (b) $R/w=9.5$. Note that the Griffith result is independent of the channel widths. In the narrow channel case (b), the difference between the Q1D and $\nu=1.9$ results is indiscernible in the scale of this graph.

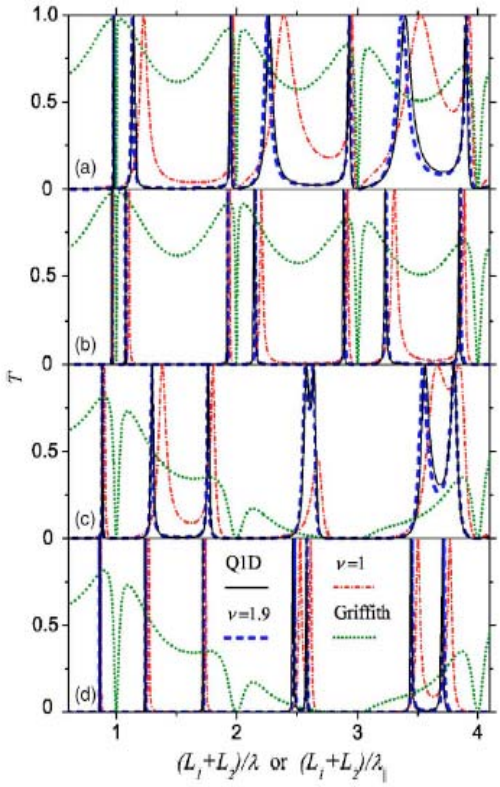

FIG. 4. (Color online) The transmission probability T is plotted versus the dimensionless longitudinal wave numbers [$(L_1+L_2)/\lambda_{\|}$ in the case of Q1D channels, and $(L_1+L_2)/\lambda$ in the case of 1D channels], for the case of asymmetrical arm lengths. The Q1D results (solid lines), 1D results due to our scheme [dashed ($\nu=1.9$) and dash-dotted ($\nu=1$) lines], and 1D results due to the Griffith scheme (dotted lines) are shown. T is plotted for the cases of broad and narrow Q1D channels, with small and appreciable differences in the arm lengths. T is plotted for (a) $R/w=3.5$, $L_2/L_1=0.9$, (b) $R/w=9.5$, $L_2/L_1=0.9$, (c) $R/w=3.5$, $L_2/L_1=0.7$, and (d) $R/w=9.5$, $L_2/L_1=0.7$. Note that the Griffith result is independent of the channel widths. In the narrow channel cases [(b) and (d)], the differences between the Q1D and $\nu=1.9$ results are indiscernible in the scale of this graph.

less blueshifted BW peaks [compare Figs. 3(a) and 3(b)]. The growth of the potential at narrowing channels can be understood as a result of the departure from the case of very broad channels (i.e., $w\sim R$), in which the system has no difference in the "band-bottom" everywhere.

While the result from the Griffith scheme is independent of the channel width and disagrees with the Q1D result, our scheme captures the trend of change in the transmission probability when the channel width is varied. Therefore, our scheme has correctly included the attractive nature of the clean Y junction of Q1D channels, though the strength has been underestimated (i.e., $\nu=1.9$ is prefered to $\nu=1$). The misjudgment of an appropriate value for the parameter ν is due to the fact that the details of the shape of the Y junctions of Q1D channels and the actual dimensionality of the channels are relevant. For instance, our simple TB argument which leads to Eqs. (5) and (6) does not show the difference between junctions with different relative directions of branching channels, and also does not distinguish a three-dimensional (3D) cylinder from a 2D strip as a Q1D channel. But in reality, the appropriate parameter ν's in those different cases may likely be different. In the 2D cases we have just seen in Fig. 3, the same kind of Y junction has been involved, and the effective potential in our scheme is characterized by an almost constant ν in both the broad [Fig. 3(a)] and narrow [Fig. 3(b)] channel cases.

Therefore, though the parameter ν cannot be derived analytically, it can be readily fixed for a particular kind of junction by comparing the 1D result with the Q1D result. What we have done in Fig. 3 has been a comparison which involves a tedious calculation. Actually, other simpler comparisons also work. For instance, one may consider the bound state at the junction due to the attraction.[29] On one hand, for a junction of three 1D channels, with the channels extended to infinity like what we depict in Fig. 1(c), the negatively valued bound state energy E can be readily found by using $\psi_i=e^{-\kappa x_i}$, where $i=1,2,3$, $\kappa\equiv\sqrt{-2mE/\hbar}$, and Eq. (6). The energy E is found to be lower than zero by an amount of $2\nu^2\hbar^2/(9mw^2)$. On the other hand, the bound state at a T-shaped junction of three Q1D channels, with the channels extended to infinity like what we depict in Fig. 1(a), was studied by Schult *et al.*[29] The energy of the state was numerically found to be lower than the first subband bottom by an amount of $0.19\pi^2\hbar^2/(2mw^2)$.[29] Equating the two energies in the 1D and Q1D cases, one gets $\nu\simeq 2.05$, which is about the number we use in Fig. 3, and as we will see, that in Fig. 4.

Figure 4 shows the transmission probabilities for the case of asymmetrical arm lengths. It is seen that in all cases,

broad channels [Figs. 4(a) and 4(c)] and narrow channels [Figs. 4(b) and 4(d)], small difference in arm lengths [Figs. 4(a) and 4(b)] and appreciable difference in arm lengths [Figs. 4(c) and 4(d)], there are good comparisons between the results due to our $\nu=1.9$ scheme and the Q1D calculation. All the essential features, such as the relative positions of the BW and Fano profiles[28] in the Q1D results, are nicely reproduced. Note that the number 1.9 agrees with the one used in Fig. 3.

For the 1D models, including Griffith's and ours, the perfectly zero transmission dips of the Fano profiles are located exactly at the eigenenergies of an isolated ring[30] with a circumference of L_1+L_2. In the 1D case, these eigenenergies are exactly at $(L_1+L_2)/\lambda \equiv k(L_1+L_2)/(2\pi)=$ integer. In the Q1D cases shown in Figs. 3 and 4, the eigenenergies are numerically found to be at the $(L_1+L_2)/\lambda_{\parallel}$'s deviated by not more than 0.5% from the integers on the horizontal axes. For the Q1D model, we find that those zero transmission dips may coincide with the eigenenergies of an isolated annulus only in the long-wavelength limit. As in the case of symmetrical arms, the Griffith result disagrees with the Q1D result, and our simple TB argument which leads to Eqs. (5) and (6) has underestimated the strength of the effective potential at the junction, i.e., $\nu=1.9$ is preferred to $\nu=1$.

IV. CONCLUDING REMARKS

It is seen that in all the above cases the results from the Griffith scheme are not in congruence with the Q1D results. The Griffith result is regardless of the channel width, whereas the Q1D result shows a strong dependence on that. Our model gives a result in much better agreement with the Q1D result. The trend of change in the transmission probability and the relative positions of the resonance profiles are impressively reproduced. In view of these calculations, it is clear that the Griffith scheme which is frequently adopted in the literature, does not describe a clean junction of Q1D channels and is definitely not for the 1D limit of the Q1D models. In the small width limit, a Y junction of Q1D channels is a strong scatterer, and that makes the Q1D system studied in this paper not at all an "open" system. Speaking reversely, adding a repulsive potential to a Y junction of Q1D channels may weaken the scattering effect and enhance the transmission through the junction at low energies, and away from the levels. When a strong magnetic field is present, our model may not apply since the field creates an additional asymmetric transverse confinement.

In conclusion, we have proposed a connection scheme with a parameter ν at a Y junction of 1D channels. The parameter ν can be most easily fixed by comparing the energy of the bound state at a Y junction of Q1D channels to the energy of the bound state at a Y junction of 1D channels due to Eq. (6). The scheme reflects the presence of an effectively attractive potential at a clean Y junction of Q1D channels. The disregard of this potential in the Griffith scheme makes its result compare poorly with the exact Q1D result.

ACKNOWLEDGMENTS

This work was supported by the National Science Council of Taiwan under Grant No. 94-2112-M-009-017. We thank the National Center for Theoretical Sciences of Taiwan for allowing us to use their facilities.

*Author to whom correspondence should be addressed. Electronic address: kkvoo@cc.nctu.edu.tw

[1] H. Kuhn, Helv. Chim. Acta **32**, 2247 (1949).
[2] J. Stanley Griffith, Trans. Faraday Soc. **49**, 345 (1953); **49**, 650 (1953).
[3] K. Ruedenberg and C. W. Scherr, J. Chem. Phys. **21**, 1565 (1953).
[4] T. Kottos and U. Smilansky, Ann. Phys. (N.Y.) **274**, 76 (1999).
[5] B. Shapiro, Phys. Rev. Lett. **50**, 747 (1983).
[6] M. Buttiker, Y. Imry, and M. Ya. Azbel, Phys. Rev. A **30**, 1982 (1984).
[7] P. Exner and P. Seba, Rep. Math. Phys. **28**, 7 (1989).
[8] Y. Gefen, Y. Imry, and M. Ya. Azbel, Phys. Rev. Lett. **52**, 129 (1984).
[9] J.-B. Xia, Phys. Rev. B **45**, 3593 (1992).
[10] J. M. Mao, Y. Huang, and J. M. Zhou, J. Appl. Phys. **73**, 1853 (1993).
[11] P. S. Deo and A. M. Jayannavar, Phys. Rev. B **50**, 11629 (1994).
[12] M. V. Moskalets, Low Temp. Phys. **23**, 824 (1997).
[13] C.-M. Ryu and S. Y. Cho, Phys. Rev. B **58**, 3572 (1998).
[14] C. Benjamin and A. M. Jayannavar, Phys. Rev. B **68**, 085325 (2003).
[15] S. K. Joshi, D. Sahoo, and A. M. Jayannavar, Phys. Rev. B **64**, 075320 (2001).
[16] B. Molnar, F. M. Peeters, and P. Vasilopoulos, Phys. Rev. B **69**, 155335 (2004).
[17] D. Bercioux, M. Governale, V. Cataudella, and V. M. Ramaglia, Phys. Rev. Lett. **93**, 056802 (2004).
[18] P. Foldi, B. Molnar, M. G. Benedict, and F. M. Peeters, Phys. Rev. B **71**, 033309 (2005).
[19] U. Aeberhard, K. Wakabayashi, and M. Sigrist, Phys. Rev. B **72**, 075328 (2005).
[20] Note that the information of the relative directions of the branches is not contained at this level. This information will be included later via a phenomenological parameter ν in Eq. (6).
[21] S. Datta, *Electronic Transport in Mesoscopic Systems*, 1st ed. (Cambridge University Press, Cambridge, 1995).
[22] J.-B. Xia and S.-S. Li, Phys. Rev. B **66**, 035311 (2002).
[23] The Q1D results in Figs. 3 and 4 are obtained using 101 transverse modes in the leads (i.e., $N=101$) and 101 angular modes in the annulus (i.e., $M=50$). The differences between these results and that using $N=201$ and $M=100$ are well within the thicknesses of the data lines in the figures.
[24] $E_0^{\text{ann.}}$ is slightly lower than the energy of the band bottom of the first subband in the leads, $\pi^2\hbar^2/(2mw^2)$.
[25] G. Breit and E. Wigner, Phys. Rev. **49**, 519 (1936).
[26] We mean a red (blue) shift of a quasibound level by a shift of the level to an energy lower (higher) than the level at the infinite

trapping potential limit, where the wave function is expelled completely from the barriers or antibarriers.

[27] Recall the fact that a quasibound level due to repulsive barriers (attractive wells) is redshifted (blueshifted).

[28] U. Fano, Phys. Rev. **124**, 1866 (1961).

[29] R. L. Schult, D. G. Ravenhall, and H. W. Wyld, Phys. Rev. B **39**, R5476 (1989).

[30] K.-K. Voo and C.-S. Chu, Phys. Rev. B **72**, 165307 (2005).

Appendix H:

Spin cloud induced around an elastic scatterer by the intrinsic spin-Hall effect

A. G. Mal'shukov[1], C. S. Chu[2]
[1]*Institute of Spectroscopy, Russian Academy of Science, 142190, Troitsk, Moscow oblast, Russia*
[2]*Department of Electrophysics, National Chiao Tung University, Hsinchu 30010, Taiwan*

Similar to the Landauer electric dipole created around an impurity by the electric current, a spin polarized cloud of electrons can be induced by the intrinsic spin-Hall effect near a spin independent elastic scatterer. It is shown that in the ballistic range around the impurity, such a cloud appears in the case of Rashba spin-orbit interaction, even though the bulk spin-Hall current is absent.

PACS numbers: 72.25.Dc, 71.70.Ej, 73.40.Lq

The spin-Hall effect attracts much interest because it provides a method for manipulating electron spins by electric gates, incorporating thus spin transport into conventional semiconductor electronics. As it has been initially predicted, the electric field $\mathbf{E}$ induces the spin flux of electrons or holes flowing in the direction perpendicular to $\mathbf{E}$. This spin flux can be due either to the intrinsic spin-orbit interaction (SOI) inherent to a crystalline solid [1], or to spin dependent scattering from impurities [2]. Intrinsic spin-Hall effect corresponding to the former situation has been observed in p-doped 2D semiconductor quantum wells [4], while the extrinsic effect related to the latter scenario has been detected in n-doped 3D semiconductor films [3].

Most of the theoretical studies on the spin-Hall effect (SHE) has been focused on calculation of the spin current (for a review see [5]). On the other hand, since the spin current carries the spin polarization, one would expect a buildup of the spin density near the sample boundaries. Such a spin accumulation near interfaces of various nature was calculated in a number of works [6, 7, 8]. This accumulated polarization is a first evidence of SHE that has been observed experimentally in Ref. [3, 4]. In fact, measuring spin polarization is thus far the only practical way to detect SHE.

Yet the spin accumulation near interfaces is not the only signature of SHE. To draw an analogy with the charge transport, one can expect that similar to Landauer charge dipoles created by the DC electric current around impurities [9], nonequilibrium spin dipoles must be formed subsequent to the spin-Hall current. One may expect that the spin cloud will appear around a spin-orbit scatterer in case of extrinsic SHE, as well as around a spin-independent scatterer, in case of the intrinsic effect. We will consider the latter possibility for a 2D electron gas with Rashba interaction. The polarization in the direction perpendicular to 2DEG will be calculated in the ballistic range around an impurity represented by an isotropic spin independent scattering potential. Besides conventional semiconductor quantum wells this analysis can be applied to metal adsorbate systems with strong Rashba type spin splitting of surface states [12]. In this case the spin cloud can be measured by STM with a magnetic tip.

The Landauer electric dipole has been calculated [10, 11] basing on the asymptotic expansion of the electron waves elastically scattered from an isolated impurity. Subsequent averaging of the corresponding spatial probability weighted by the Boltzmann distribution function of incident wavevectors produces the dipole distribution. The spin cloud could be obtained in a similar way. Instead, we choose a Green function method combined with the linear response theory. Within this method the spin density is given by the standard Kubo formula where the scattering potential of a target impurity, at a fixed position $\mathbf{r}_i$, is included into the Green functions, up to the second perturbation order. Other impurities are assumed to be randomly distributed over a 2D plane, so that the calculated spin density is averaged over their positions.

We assume that a uniform external electric field is applied to 2DEG. The field is represented by the vector potential $\mathbf{A}$, $\mathbf{E} = i\omega\mathbf{A}/c$, with $\omega \to 0$ in the DC regime. The corresponding interaction Hamiltonian is $e\mathbf{A}\cdot\mathbf{v}/c$, where the velocity v^j, $j = x, y$, includes the spin-orbit correction $\partial(\mathbf{h_k}\cdot\boldsymbol{\sigma})/\partial k^j$. The spin-orbit field $\mathbf{h_k}$ is a function of the two-dimensional wave-vector $\mathbf{k}$. In its turn, the spin-orbit interaction is written in the form

$$H_{so} = \mathbf{h_k}\cdot\boldsymbol{\sigma}\,, \tag{1}$$

where $\boldsymbol{\sigma}\equiv(\sigma^x,\sigma^y,\sigma^z)$ is the Pauli matrix vector. We assume that the target impurity, located at $\mathbf{r}_i$, has a scattering potential $U(\mathbf{r}-\mathbf{r}_i)$. In 2D geometry the corresponding Born amplitude is given by

$$f(\mathbf{k},\mathbf{k}') = -\frac{m^*}{\sqrt{2\pi k_F}}\int dr^2 U(\mathbf{r})e^{i(\mathbf{k}-\mathbf{k}')\mathbf{r}}\,, \tag{2}$$

where $\hbar = 1$ and φ is the angle between $\mathbf{k}$ and $\mathbf{k}'$. Both the scattered and the incident wavevectors are taken at the Fermi circle with the radius k_F. Other impurities, which not necessarily are of the same nature as the target impurity, are randomly distributed within a sample. They create the random potential $V_{sc}(\mathbf{r})$ which is assumed to be delta correlated, so that the pair correlator $\langle V_{sc}(\mathbf{r})V_{sc}(\mathbf{r}')\rangle = \Gamma\delta(\mathbf{r}-\mathbf{r}')/\pi N_F$, where N_F is the electron density of states at the Fermi energy, and $\Gamma = 1/2\tau$ is expressed via the mean elastic scattering time τ. Assuming that the semiclassical approximation $E_F\tau \gg 1$

is valid, one can apply the standard perturbation theory [13, 14] when calculating the configurational averages of Green functions and their products. In the leading order of $(E_F\tau)^{-1}$ and up to the second order in $U(\mathrm{r}-\mathrm{r}_i)$, the average retarded Green function in the momentum representation is given by

$$G^r_{\mathbf{kk}'}(\omega) = \delta_{\mathbf{kk}'}G^{r(0)}_{\mathbf{k}}(\omega) + G^{r(1)}_{\mathbf{kk}'}(\omega) + G^{r(2)}_{\mathbf{kk}'}(\omega)\,, \quad (3)$$

with the unperturbed function given by the 2×2 matrix

$$G^{r(0)}_{\mathbf{k}}(\omega) = (\omega - E_{\mathbf{k}} - \boldsymbol{h}_{\mathbf{k}}\cdot\boldsymbol{\sigma} + i\Gamma)^{-1}\,, \quad (4)$$

where $E_{\mathbf{k}}$=$k^2/(2m^*)$. Other functions in (3) are

$$\begin{aligned} G^{r(1)}_{\mathbf{kk}'}(\omega) &= G^{r(0)}_{\mathbf{k}}(\omega)U_{\mathbf{kk}'}G^{r(0)}_{\mathbf{k}'}(\omega) \quad (5)\\ G^{r(2)}_{\mathbf{kk}'}(\omega) &= G^{r(0)}_{\mathbf{k}}(\omega)\sum_{\mathbf{k}''}U_{\mathbf{kk}''}G^{r(0)}_{\mathbf{k}''}(\omega)U_{\mathbf{k}''\mathbf{k}'}G^{r(0)}_{\mathbf{k}'}(\omega)\,. \end{aligned}$$

The matrix elements $U_{\mathbf{k}'\mathbf{k}} = -\sqrt{2\pi k_F}f(\mathrm{k},\mathrm{k}')\exp[i(\mathrm{k}-\mathrm{k}')\mathrm{r}_i]/m^*$. Expressions similar to Eqs.(3-5) can be obtained for the advanced functions $G^a_{\mathbf{k}'\mathbf{k}}(\omega) = G^r_{\mathbf{k}'\mathbf{k}}(\omega)^\dagger$. The sum over k'' in the second Eq. (5) can be directly calculated. First, we decompose $G^{r(0)}_{\mathbf{k}''}$ into a spin independent scalar part and a spin dependent part which is proportional to $\mathrm{h}_{\mathbf{k}''}\cdot\boldsymbol{\sigma}$. Due to the time inversion symmetry $\mathrm{h}_{\mathbf{k}''} = -\mathrm{h}_{-\mathbf{k}''}$ the sum over k'' on the spin dependent part is zero for an isotropic scattering amplitude. For anisotropic amplitude, however, this sum is not identically 0. Nevertheless, the sum on the spin dependent part can be ignored either way in the following calculations, because it is proportional to the small parameter $h_{k_F}/E_F \ll 1$. Further, it is easily seen that only $\mathrm{Im}[G^{r(0)}_{\mathbf{k}''}]$ is important in this k'' sum because the real part gives rise to a term that simply adds to $U_{\mathbf{kk}'}$ in the first line of Eq. (5), thus effectively renormalizing the Born scattering amplitude. The imaginary part can not be absorbed in such a way because it has opposite signs for the advanced and retarded Green functions. Taking into account that $\omega \simeq E_F$ and assuming that $h_{k_F} \ll E_F$ we thus get

$$\begin{aligned} &\sum_{\mathbf{k}''}U_{\mathbf{kk}''}G^{r(0)}_{\mathbf{k}''}(\omega)U_{\mathbf{k}''\mathbf{k}'} = -i\pi N_F S(\mathrm{k},\mathrm{k}')e^{i(\mathbf{k}'-\mathbf{k})\mathbf{r}_i}\\ &S(\mathrm{k},\mathrm{k}') = \frac{k_F}{m^{*2}}\int d\varphi'' f(\mathrm{k}'',\mathrm{k})f(\mathrm{k}',\mathrm{k}'')\,, \quad (6) \end{aligned}$$

where ϕ'' is the angle of the vector k'', with $|\mathrm{k}''| = k_F$. At $\mathrm{k} = \mathrm{k}'$ the integral in (6) is equal to the scattering cross-section.

Within the semiclassical theory we follow the well known method [13, 14] to calculate the configurational average of the Green function pair product that enters into the Kubo's linear response equation. Therefore, we take into account, as our leading approximation, only the so called ladder series describing particle and spin diffusion processes. Some of the representative diagrams

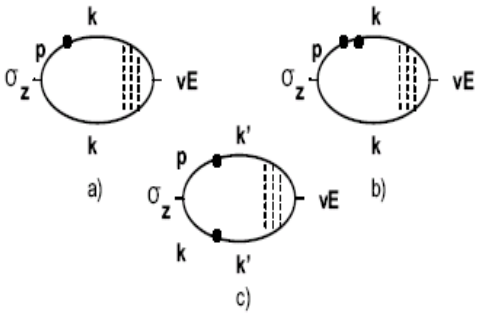

FIG. 1: Diagram for the spin density. Scattering of electrons by a target impurity is shown by the solid circles. Dashed lines denote the ladder series of particle scattering by the random potential. $\mathbf{p},\mathrm{k},\mathrm{k}'$ are electron momenta.

are shown at Fig. 1. The diffusion ladder renormalizes only the vertex associated with the electric field, while such a ladder does not appear at the vertex attributed to the induced spin density. It is because in the ballistic range around the impurity, the momentum transfer $|\mathrm{p}-\mathrm{k}| \gg 1/(v_F\tau)$, and thus the diffusion is not important. Finally, the density of spins oriented in z direction can be written as

$$\begin{aligned} \sigma_z(\mathrm{r}) &= \sum_{\mathbf{k},\mathbf{k}',\mathbf{p}} e^{i(\mathbf{p}-\mathbf{k})\mathbf{r}}\int\frac{d\omega}{2\pi}\frac{dn_F(\omega)}{d\omega}\times\\ &\quad Tr[G^a_{\mathbf{k}'\mathbf{k}}(\omega)\sigma_z G^r_{\mathbf{pk}'}(\omega)\mathcal{T}(\omega,\mathrm{k}')]\,, \quad (7) \end{aligned}$$

where the trace runs through the spin variables and $n_F(\omega)$ is the Fermi distribution function. The functions $G^{r/a}_{\mathbf{k}'\mathbf{k}}$ are given by Eq. (3). In (7), only terms up to the second order in $U_{\mathbf{k}'\mathbf{k}}$ should be taken into account. Hence the highest order corrections are those shown at Fig.1, b) and c). At low temperatures only ω in close vicinity around E_F contributes to the integral in (7). Therefore, below we set $\omega = E_F$. In the following it is convenient to write the vertex $\mathcal{T}(E_F,\mathrm{k}')$ in the vector representation, using the complete set of four 2×2 matrices $\tau_0 = 1$, and $\tau_i = \sigma_i$ at $i = x,y,z$. We thus have

$$\mathcal{T}_b(E_F,\mathrm{k}) = \frac{1}{2}Tr[\tau_b\mathcal{T}(E_F,\mathrm{k})],\quad b = 0,x,y,z \quad (8)$$

and the ladder summation gives

$$\begin{aligned} \mathcal{T}_b(E_F,\mathrm{k}) &= e\mathrm{v}_b\mathbf{E} + \frac{e\Gamma}{2\pi N_F}\sum_c D^{bc}\times \quad (9)\\ &\quad \sum_{\mathbf{k}'}Tr[\tau_c G^{r(0)}_{\mathbf{k}'}(E_F)\mathrm{v}\mathbf{E}G^{a(0)}_{\mathbf{k}'}(E_F)]\,. \end{aligned}$$

D^{bc} is the diffusion propagator satisfying the diffusion equation, as it was described in [15]. In our case D^{bc} is determined by the spin relaxation time of a uniform spin distribution.

The sum over k' in Eq. (9) can be directly calculated. Let us consider the part of it associated with the spin independent velocity, which is the first term in

$$\mathrm{v}^j = \frac{k^j}{m^*} + \frac{\partial \mathbf{h}_\mathbf{k} \cdot \boldsymbol{\sigma}}{\partial k^j} . \tag{10}$$

At $h_\mathbf{k} \ll E_F$ we find

$$\frac{\Gamma}{2\pi N_F} \sum_\mathbf{k} \frac{k^j}{m^*} Tr[\sigma_c G^{r(0)}_\mathbf{k}(E_F) G^{a(0)}_\mathbf{k}(E_F)] = -\overline{\frac{\partial h^c_\mathbf{k}}{\partial k^j}} , \tag{11}$$

where the bar denotes angular averaging over the Fermi circle. Using this equation one can rewrite (9) in such a way that the velocity operator v_b is substituted for $\mathrm{v}_b - \overline{\mathrm{v}_b}$, and the scalar spin independent part of $\mathbf{v}$ does not enter into the second term of (9). Now it is easily to see that $\mathrm{v}_b - \overline{\mathrm{v}_b} = \mathrm{k}/m^*$ for any spin-orbit interaction where $\mathbf{h}_\mathbf{k}$ depends linearly on $\mathbf{k}$. Consequently, from (9) we get the simple expression

$$\mathcal{T} = \frac{e}{m^*} \mathbf{k}\mathbf{E} . \tag{12}$$

It should be noted that the same vertex in Eq. (9) enters into the spin-Hall current, and the cancelation of the spin dependent part from the velocity operator is the main reason for vanishing of spin-Hall conductance in case of Rashba SOI [16]. Such a cancelation, however, does not take place in case of nonlinear SOI [15].

Let us consider the spin density (7) in the presence of the Rashba spin-orbit field $h_x = \alpha k_y, h_y = -\alpha k_x$. In the zeroth order in $U_{\mathbf{k}\mathbf{k}'}$ the Green functions in (7) are given by the first term in (3). In this approximation and with $\mathcal{T}$ given by (12) one can easily see that $\sigma_z(\mathbf{r}) = 0$. On the other hand, the inplane spin polarization directed perpendicular to $\mathbf{E}$ is finite. This polarization is due to the electric orientation effect [17]. In the first order with respect to $U_{\mathbf{k}\mathbf{k}'}$ the z spin polarization is represented by Fig.1a. Expressing $U_{\mathbf{k}\mathbf{k}'}$ via the scattering amplitude, from (3-5) and (7) we obtain

$$\sigma^{(a)}_z(\mathbf{r}) = -e\sqrt{\frac{k_F}{2\pi}} \sum_{\mathbf{k},\mathbf{p}} \frac{\mathbf{k}\mathbf{E}}{m^{*2}} Tr[G^r_\mathbf{k}(E_F) G^a_\mathbf{k}(E_F) \times \left(\sigma_z G^r_\mathbf{p}(E_F) f(\mathbf{p},\mathbf{k}) e^{i(\mathbf{p}-\mathbf{k})\mathbf{R}} + h.c.\right)] , \tag{13}$$

where $\mathbf{R} = \mathbf{r} - \mathbf{r}_i$. At $k_F R \gg 1$ the angular integration in (13) can be performed by expansions around the saddle-points $(\mathbf{p}\mathbf{R}/pR) = \pm 1$ and $(\mathbf{k}\mathbf{R}/kR) = \pm 1$, which result in the asymptotic expansion of $\sigma_z(\mathbf{r})$ at a large distance from the impurity. In these saddle points the scattering amplitude entering into (13) will coincide either with the forward scattering amplitude $f(0) = f(k_F\hat{\mathbf{R}}, k_F\hat{\mathbf{R}})$, or with the backscattering amplitude $f(\pi) = f(k_F\hat{\mathbf{R}}, -k_F\hat{\mathbf{R}})$, where $\hat{\mathbf{R}} = \mathbf{R}/R$ is the unit vector directed to the observation point. Finally, we obtain from (13)

$$\sigma^{(a)}_z(\mathbf{r}) = \frac{m^*}{R}\sqrt{\frac{2}{\pi^3 k_F}} v^j_d \left(\frac{\partial \mathbf{n}_R}{\partial R^j} \times \mathbf{n}_R\right) \times \mathrm{Re}[f(\pi) e^{2ik_F R}] \sin^2\left(\frac{R}{L_{so}}\right) , \tag{14}$$

where $\mathrm{v}_d = e\tau\mathbf{E}/m^*$ is the drift velocity and $L_{so} = \hbar/m^*\alpha$ is the characteristic spin-orbit length. The unit vector $\mathbf{n}_R = \mathbf{h}_{k_F\hat{\mathbf{R}}}/|h_{k_F\hat{\mathbf{R}}}|$. For Rashba interaction it is $n^x_R = \hat{R}^y$, $n^y_R = -\hat{R}^x$.

Similarly, the second order contribution to the spin density, as it is represented in Fig. 1b) and c) can be calculated via Eq.(6). Assuming that the electric field is applied in the x-direction and in the case of Rashba interaction, we get the final result, which is as a sum of all diagrams in Fig. 1a)-c),

$$\sigma_z(\mathbf{r}) = -\frac{m^* v_d \sigma_t}{2\pi^2 R L_{so}} \sin\left(\frac{2R}{L_{so}}\right) \sin\theta + \frac{m^* v_d}{2\pi^2 R^2} \sin^2\left(\frac{R}{L_{so}}\right) \sin^3\theta \times \left(\sigma_{tot} + \sqrt{\frac{8\pi}{k_F}} \mathrm{Re}[f(\pi) e^{2ik_F R}]\right) , \tag{15}$$

where σ_{tot} and σ_t are the total and transport scattering cross sections, respectively, and θ is the angle between the vector $\mathbf{R}$ and the x-axis. In order to check our method we applied it to the calculation of the charge dipole, whence σ_z is substituted by 1 in Eq. (7). Ignoring SOI we obtained the same result as in Ref.[11].

The explicit shape of the spin cloud is clearly seen from Eq. (15). It consists of a dipole, oriented perpendicular to the electric field, and a tripole. Similar to the Landauer charge dipole distribution [11], the spin density contains both slowly varying and fast Friedel oscillation components. Important distinctions, however, are found in the asymptotic behaviors. First, unlike the charge density, whose slow asymptotic term is represented by monotonous R^{-1} dependence, the spin density oscillates with a period determined by the spin-orbit precession length πL_{so}. Second, at smaller distances $R \lesssim L_{so}$, the polarization decreases as R^{-2}. It should be noted that this asymptotic form can not be obtained by the method based on the conventional leading order asymptotic expansion of the wave function, as it has been done in [11] for the Landauer dipole. It is because in 2D geometry the corresponding scattered amplitude decreases as $1/\sqrt{R}$. Accordingly, the probability density, which can be either the charge or the spin density, will be proportional to $1/R$, not $1/R^2$.

When talking about asymptotic expression (15), one should not forget that it is restricted by the ballistic range $R \lesssim l$, where l is the mean free path. At larger distances the ballistic part of the spin density decays as $exp(-R/l)$. On the other hand, outside the ballistic range the spin

diffusion becomes important. Spin diffuses during the D'yakonov-Perel' [18] spin relaxation time, up to the distance $\sim L_{so}$. Hence, the spin diffusion must be taken into account at $R \gg l$, providing that the spin-orbit coupling is not too strong, so that $L_{so} \gg l$. In order to calculate the spin density in the diffusive range, the ladder diagrams renormalizing the left hand vertex in Fig. 1 should be taken into account. The evident result to be expected in this case is that the diffusion spin cloud with the size $\gg l$ will appear in addition to Eq.(15). Due to the spin relaxation, however, the spin density will decay exponentially at $R \gg L_{so}$. This behavior is in sharp contrast to the power law decreasing of the charge density [10]. In the latter case, the long-range R^{-1} charge-density tails of many impurities result in the macroscopic electric field which can be related to the electric potential difference at the sample boundaries. This was the main idea by Landauer - to associate impurities with resistors which give rise to an overall potential drop for a given current. In a similar way, one would try to formulate the spin-Hall effect in terms of the spin-Hall resistance and spin dependent chemical potential $\chi(\mathrm{r})$, defined as $N_F \chi(\mathrm{r}) = \sum_i \sigma_z(\mathrm{r} - \mathrm{r}_i)$. But, due to the exponential decay in space of the spin cloud, the well converging sum over impurities will produce, on average, a vanishing "spin-Hall" chemical potential everywhere, except for the $R \sim L_{so}$ range near the sample boundary. No such spin accumulation, on the other hand, has been found near flanks of a 2D diffusive strip of 2DEG with Rashba SOI [7]. Probably, this means that the spin density outside the ballistic range around an elastic scatterer will be zero in case of Rashba SOI. An answer to this question is, however, outside the scope of the present study.

In conclusion, for a 2DEG with Rashba spin-orbit interaction we calculated the nonequilibrium spin polarization induced by the intrinsic spin-Hall effect in the ballistic range around a spin independent scatterer. The angular spatial distribution of the spin density is represented by a tripole and a dipole oriented perpendicular to the electric field. As a function of the distance from the scatterer, the polarization shows the power law decay with oscillations, some terms oscillating relatively slowly, with the period πL_{so}, while other terms varying fast, with a period of Friedel oscillations. Noteworthy, that although the z-polarized spin-Hall current is zero in case of Rashba SOI, we found out that the z-component of the spin density is not zero in the ballistic range. This agrees with finite spin accumulation near flanks of a ballistic strip [8].

This work was supported by the Taiwan National Science Council NSC94-2811-M-009-010 and RFBR Grant No 060216699. A.G.M. acknowledges the hospitality of Taiwan National Center for Theoretical Sciences.

[1] S. Murakami, N. Nagaosa, and S.-C. Zhang, Science **301**, 1348 (2003); J. Sinova *et. al.*, Phys. Rev. Lett. **92**, 126603 (2004); D. Culcer *et. al.*, Phys. Rev. Lett. 93, 046602 (2004).

[2] M. I. Dyakonov, V. I. Perel, Phys. Lett. A **35**, 459 (1971); J. E. Hirsch, Phys. Rev. Lett **83**, 1834 (1999).

[3] Y. K. Kato, *et. al.*, Science **306**, 1910 (2004)

[4] J. Wunderlich *et. al.*, Phys. Rev. Lett. **94**, 047204 (2005)

[5] H. -A. Engel, E. I. Rashba, and B. I. Halperin, cond-mat/0603306.

[6] V. M. Galitski *et. al.*, cond-mat/0601677; G. Usaj and C. Balsiero, cond-mat/0405065; I. Adagideli and G.E.W. Bauer, Phys. Rev. Lett. **95**, 256602 (2005);

[7] A. G. Mal'shukov *et. al.*, Phys. Rev. Lett. **95**, 146601 (2005); R. Raimondi *et. al.*, cond-mat/0601525;

[8] B. K. Nikolić *et. al.*, Phys. Rev. Lett. **95**, 046601 (2005); Q. Wang *et. al.*, cond-mat/0505576.

[9] R. Landauer, IBM Journ. Res. Development, 1, 223 (1957); R. Landauer, Philos. Mag. 21,863 (1970).

[10] R. S. Sorbello and C.S. Chu, IBM J. Res. Develop. **32**, 58 (1988); C.S. Chu and R. S. Sorbello, Phys. Rev. B **38**, 7260 (1988)

[11] W. Zwerger, L. Bönig, and K. Schonhammer, Phys. Rev. B **43**, 6434 (1991)

[12] C. R. Ast *et. al.* cond-mat/0509509 unpublished

[13] A.A. Abrikosov, L.P. Gor'kov, and I.E. Dzyaloshinskii, Methods of Quantum Field Theory in Statistical Physics, (Dover, New York, 1975)

[14] B. L. Altshuler and A. G. Aronov, in *Electron-Electron Interactions in Disordered Systems*, edited by A. L. Efros and M. Pollak (North-Holland, Amsterdam, 1985).

[15] A. G. Mal'shukov and K. A. Chao, Phys. Rev. B **71**, 121308(R) (2005)

[16] J. I. Inoue, G. E. W. Bauer, and L.W. Molenkamp, Phys. Rev. B **70**, 041303 (2004); E. G. Mishchenko, A. V. Shytov, and B. I. Halperin, Phys. Rev. Lett. **93**, 226602 (2004); E. I. Rashba, Phys. Rev. B **70**, 201309(R) (2004); R. Raimondi and P. Schwab, Phys. Rev. B **71**, 033311 (2005).

[17] V.M. Edelstein, Solid State Commun., **73**, 233 (1990); J. I. Inoue, G. E. W. Bauer, and L.W. Molenkamp, Phys. Rev. B **67**, 033104 (2003)

[18] M. I. D'yakonov and V. I. Perel', Sov. Phys. JETP **33**, 1053 (1971) [Zh. Eksp. Teor. Fiz. **60**, 1954 (1971)].